

MICROSTRUCTURE DEVELOPMENT IN NICKEL ZINC FERRITES

A THESIS SUBMITTED TO
THE GRADUATE SCHOOL OF NATURAL AND APPLIED SCIENCES
OF
MIDDLE EAST TECHNICAL UNIVERSITY

BY

MAHMUT BARIŞ OKATAN

IN PARTIAL FULFILLMENT OF THE REQUIREMENTS
FOR
THE DEGREE OF MASTER OF SCIENCE

IN

METALLURGICAL & MATERIALS ENGINEERING

DECEMBER 2005

Approval of the Graduate School of Natural and Applied Sciences.

Prof. Dr. Canan Özgen
Director

I certify that this thesis satisfies all the requirements as a thesis for the degree of Master of Science.

Prof. Dr. Tayfur Öztürk
Head of Department

This is to certify that we have read this thesis and that in our opinion it is fully adequate, in scope and quality, as a thesis for the degree of Master of Science.

Prof. Dr. Muharrem Timuçin
Supervisor

Examining Committee Members

Prof. Dr. Macit Özenbaş	(METU, METE) _____
Prof. Dr. Muharrem Timuçin	(METU, METE) _____
Prof. Dr. Abdullah Öztürk	(METU, METE) _____
Assist. Prof. Dr. Arcan Dericioğlu	(METU, METE) _____
Prof. Dr. Hüsnü Özkan	(METU, PHYS) _____

I hereby declare that all information in this document has been obtained and presented in accordance with academic rules and ethical conduct. I also declare that, as required, I have fully cited and referenced all material and results that are not original to this work.

Name Lastname : Mahmut Barış Okatan

Signature :

ABSTRACT

MICROSTRUCTURE DEVELOPMENT IN NICKEL ZINC FERRITES

Okatan, Mahmut Barış

M. S., Department of Metallurgical & Materials Engineering

Supervisor: Prof. Dr. Muharrem Timuçin

December 2005, 134 pages

Nickel zinc ferrites (NZF) have been considered as one of the basic components in high frequency electromagnetic applications especially in the field of telecommunications. In the present study, the aim was to produce high quality nickel zinc ferrite ceramics at low soaking temperatures. For this purpose, conventional ceramic manufacturing method based on mixed oxide precursors was followed using calcium fluoride, CaF_2 , as sintering additive.

During the sintering studies, it was noticed that both the microstructure and the electromagnetic properties of the NZF ceramics were modified to a great extent by CaF_2 . Therefore, material characterization studies involving microstructural, dielectric and magnetic properties were conducted with respect to CaF_2 content of ceramics and soak duration.

The results showed that due to the presence of CaF_2 in ceramics, significant improvements were achieved not only in kinetics of sintering but also in the parameters; DC electrical resistivity, dielectric constant and dielectric loss factor. For example, 1.0 wt% CaF_2 added NZF ceramic produced in this study had a DC electrical resistivity of 10^{11} Ω -cm which was “100,000” times bigger than the one attained in pure NZF ceramic. On the other hand, the dielectric constant exhibited

a flat behavior up to 40 MHz with a value around 16. In addition, no resonance peak was observed in dielectric loss factor spectra, and the typical values of dielectric loss factor lied below 0.01. Besides the achievements mentioned, the magnetic properties such as relative magnetic loss factor and hysteresis parameters were also improved.

Keywords: Nickel zinc ferrite, sintering, DC electrical resistivity, dielectric properties, magnetic properties.

ÖZ

NİKEL ÇİNKO FERRİTLERDE İÇ YAPI GELİŞİMİ

Okatan, Mahmut Barış

Y. Lisans, Metalurji ve Malzeme Mühendisliği

Tez Yöneticisi: Prof. Dr. Muharrem Timuçin

Aralık 2005, 134 sayfa

Nikel çinko ferritler (NÇF) yüksek frekans elektromanyetik uygulamalarında, özellikle telekomünikasyon alanında, kullanılan en temel malzemelerden biri olarak kabul edilmektedir. Bu çalışmada, amaç yüksek kalitede nikel çinko ferrit seramiklerinin düşük sıcaklıklarda üretilmesidir. Bu amaçla, oksit karışımı methoduna dayanan geleneksel seramik üretim yöntemi izlenmiş sinterleme bileşeni olarak kalsiyum florür, CaF_2 , kullanılmıştır.

Sinterleme çalışmaları sırasında, NÇF seramiklerinin hem içyapı hem de elektromanyetik özelliklerinin CaF_2 ile oldukça değiştiği belirlenmiştir. Bu yüzden, içyapı, dielektrik ve manyetik özellikleri içeren malzeme karakterizasyon çalışmaları CaF_2 içeriğine ve pişirme süresine bağlı olarak sürdürülmüştür.

Sonuçlar göstermiştir ki, kalsiyum florür eklenmesi dolayısı ile hem sinterlenme kinetiğinde hem de doğru akım elektrik direnci, dielektrik sabiti ve dielektrik kayıp faktörü parametrelerinde önemli gelişmeler sağlanmıştır. Örneğin, bu çalışmada üretilen ağırlıkça % 1.0 CaF_2 içeren NÇF seramiklerinde doğru akım direncinin 10^{11} Ω -cm değerine ulaştığı ve saf NÇF seramiğine oranla 100,000 kat daha büyük olduğu tespit edilmiştir. Öte yandan dielektrik sabiti 16 civarında 40 MHz'e kadar düz bir davranış sergilemiştir. Ayrıca, dielektrik kayıp

faktörünün frekansa bağılı deęişiminde rezonans oluşturmadığı ve dielektrik kayıp faktörünün tipik deęerlerinin 0.01'in altında yer aldığı gözlenmiştir. Bahsedilen başarıların yanında manyetik özelliklerden göreceli manyetik kayıp faktörü ve histeresiz parametrelerinde artış olmuştur.

Anahtar Kelimeler: Nikel çinko ferrit, sinterleme, doğru akım elektrik direnci, dielektrik özellikler, manyetik özellikler.

To SoahC
and
Arëwòr the Arcane Archer

ACKNOWLEDGEMENTS

The author wishes to express his deepest gratitude to his supervisor Prof. Dr. Muharrem Timuçin for his guidance, advice, criticism, encouragement and insight throughout the research.

The author expresses sincere appreciation to Barış Nakibođlu for supplying most of the crucial articles from far away lands across the Atlantic Ocean.

The author also wants to express sincere thanks to Cengiz Tan for his kind interest during SEM studies and Necmi Avcı for performing XRD measurements.

The author also would like to thank Yoldaş Ataseven for his guidance in hysteresis studies and Dr. Nurşen Koç and Ayhan Yılmaz for their moral support and encouragement throughout the thesis.

Thanks are to all of my friends at the Department of Metallurgical and Materials Engineering, METU, especially Prof. Dr. Şakir Bor, Dr. Elif Tarhan, Tufan Güngören, Ziya Esen, Güher Kotan, Melih Topçuođlu and Çekdar Ahmetvakıfođlu for creating a warm and dependable working place.

Finally, a very special thanks to my parents for their support, encouragement and trust in me throughout my life.

TABLE OF CONTENTS

PLAGIARISM.....	iii
ABSTRACT	iv
ÖZ.....	vi
ACKNOWLEDGEMENTS	ix
TABLE OF CONTENTS	x
LIST OF TABLES	xiii
LIST OF FIGURES.....	xiv
CHAPTERS	
1. INTRODUCTION.....	1
2. LITERATURE SURVEY	4
2.1 Ferrites.....	4
2.1.1 Classification of Ferrites	7
2.1.2 Crystal Structure of Spinel Ferrites.....	8
2.1.3 Cation Distribution in Spinel Ferrites	10
2.2 Magnetism in Ferrites.....	11
2.2.1 Curie Temperature.....	13
2.2.2 Anisotropy	14
2.3 Electrical Resistivity	15
2.4 Microstructure	18
2.4.1 Powder Characteristics.....	18
2.4.1.1 Effect of Particle Size.....	18
2.4.1.2 Effect of Defect Structure of Particles	19
2.4.1.2.1 Particles with Excess Fe ₂ O ₃	21
2.4.1.2.2 Fe ₂ O ₃ Deficient Particles.....	25
2.4.2 Sintering Method.....	26
2.4.3 Chemical Modifications	27
2.4.4 Additives	32

3. EXPERIMENTAL PROCEDURES	33
3.1 General	33
3.2 Experimental Technique	33
3.2.1 Synthesis of the Nickel Zinc Ferrite Powder	33
3.2.2 Preparation of Ceramic Samples	39
3.2.3 Characterization.....	42
3.2.3.1 Density Measurements	42
3.2.3.2 Microstructural Characterization.....	43
3.2.3.2.1 Grain Size and Grain Size Distribution.....	43
3.2.3.3 X-Ray Diffraction.....	48
3.2.3.4 SEM Investigations	49
3.2.3.5 Electrical Characterization	49
3.2.3.5.1 Electrical Resistivity Measurements	49
3.2.3.5.2 Dielectric Constant and Dielectric Loss Factor Measurements	50
3.2.3.6 Magnetic Characterization	51
3.2.3.6.1 Initial Magnetic Permeability and Magnetic Loss Factor	51
3.2.3.6.2 Magnetic Hysteresis	52
4. EXPERIMENTAL DATA AND RESULTS	56
4.1 General	56
4.2 X-Ray Diffraction Studies on Sintered Ferrites	56
4.3 Data and Results on Sintered Density	59
4.4 Microstructural Features by SEM Analyses.....	63
4.6 Grain Size and Grain Size Distribution.....	77
4.6.1 Factors Effecting Average Grain Size.....	79
4.7 Densification Mechanism.....	81
4.8. Electrical Properties	86
4.8.1 Electrical Resistivity	86
4.8.2 Dielectric Properties	90
4.8.2.1. Dielectric Constant.....	90
4.8.2.1.1 Dielectric Constant of the CaF ₂ -free NZF Ceramics	91
4.8.2.1.2 Dielectric Constant of NZF Ceramics Containing CaF ₂	92

4.8.2.2. Dielectric Loss Factor	95
4.9 Magnetic Properties.....	99
4.9.1 Initial Magnetic Permeability.....	99
4.9.2 Dispersion in Magnetic Permeability with Frequency.....	100
4.9.3 Relative Loss Factor.....	103
4.9.4 Magnetic Hysteresis	106
4.9.4.1 Hysteresis in CaF ₂ -free NZF Ceramics.....	106
4.9.4.2 Hysteresis in the NZF Ceramics Containing CaF ₂	107
5. DISCUSSION AND CONCLUSION.....	113
REFERENCES.....	119
APPENDIX	128
A. GRAIN SIZE DISTRIBUTION GRAPHS OF NZF CERAMICS	128

LIST OF TABLES

Table 2.1 Various types of soft ferrite cores with their area of utilization [19].	6
Table 2.2 Summary of ferrite crystal structure types, typified by changes in the $\text{Fe}_2\text{O}_3 - \text{MeO}$ (or Me_2O_3) modifier oxide ratios [19].	8
Table 2.3 Effect of some processing and chemical modifications on electrical and magnetic properties of NZF ceramics.	29
Table 3.1 Characteristics of powders used in the production of ferrite powders.	35
Table 3.2 The parameters of the X-ray diffraction analysis.	48
Table 4.1 The bulk density data for the NZF ceramics produced in the present study.	60
Table 4.2 The extent of densification in the NZF ceramics of the present work, expressed as percentage of the theoretical density of the ferrite.	61
Table 4.3 Time dependence of densification (fitted equations).	63
Table 4.4 The variation of average grain size with soaking time and with the amount of CaF_2	79
Table 4.5 Values of the parameters relevant to the assessment of densification mechanism in the NZF ceramics sintered with the aid of CaF_2	84
Table 4.6 Values of the grain size exponent “n” with respect to wt% CaF_2 addition.	86
Table 4.7 DC electrical resistivity of NZF ceramics prepared in this thesis.	88
Table 4.8 Initial magnetic permeability in the NZF ceramics.	100
Table 4.9 Hysteresis parameters of the NZF ceramics studied in this thesis.	110

LIST OF FIGURES

Figure 2.1 Structure of spinel; open circles are oxygen ions, full circles are Me^{2+} cations and shaded circles are Fe^{3+} cations. Only one layer (100) is shown for the sake of clarity [21].	9
Figure 2.2 Sphere model of the spinel structure revealing tetrahedral and octahedral sites between oxygen anions [22].	9
Figure 2.3 Effect of $ZnFe_2O_4$ addition on the magnetization of the ferrites of Ni, Co, and Mn. Increased saturation magnetization effects should be noted [19].	13
Figure 2.4 Depression of the magnetic Curie temperature, T_c , with Zn additions to Mn, Co, Ni, and Li/Fe ferrites [19].	14
Figure 2.5 A cluster of tetrakaidecahedral grains with insulating boundary surfaces between them.	17
Figure 2.6 The variation of oxygen vacancy flux emitted from a pore in a solid solution of $(1-x) MO + x L_2O$.	21
Figure 2.7 Mechanism of pore migration proposed in cation deficient ferrites during firing [28].	24
Figure 2.8 Microstructure of a cation deficient ferrite sintered in oxygen. Grains are absolutely free from pores [28].	24
Figure 2.9 Optical micrograph taken from an anion deficient ferrite enlightening trapped tiny pores in grains [12].	26
Figure 2.10 The microstructure of a ferrite for microwave frequency applications produced via hot pressing [12].	27
Figure 3.1 The flowchart showing the steps involved in the production of the nickel zinc ferrite powder.	34
Figure 3.2 XRD of the NZF powder after the first calcination.	37
Figure 3.3 XRD of the NZF powder after the second calcination.	37
Figure 3.4 XRD of the powder produced after the third calcination showing single phase NZF.	38

Figure 3.5 A SEM photo of the NZF powder produced by thermal synthesis technique used in this study.....	39
Figure 3.6 The time - temperature program used during sintering experiments of this study.....	41
Figure 3.7 NZF samples prepared for experimental studies in this thesis.....	41
Figure 3.8 An optical micrograph of a nickel zinc ferrite ceramic used for grain size determination.....	44
Figure 3.9 The circle with radius r created due to sectioning of a sphere with radius R . The plane of polish includes circle with radius r	44
Figure 3.10 A typical histogram obtained from plane of polish of the ferrite ceramic produced in this study.....	46
Figure 3.11 The coefficients of the distribution function for spheres, P_n , with observed Q_n values.....	47
Figure 3.12 Schematic representation of the set up used for DC electrical resistivity measurements.	50
Figure 3.13 Schematic representation of the set-up used for dielectric property investigations.....	51
Figure 3.14 Demonstration of the setup used for inductance and loss factor measurements of toroids.....	52
Figure 3.15 Schematic representation of the setup constructed for magnetic hysteresis measurements.	53
Figure 4.1 XRD patterns of nickel-zinc ferrite ceramics containing various amounts of CaF_2 . The samples were soaked at $1200\text{ }^\circ\text{C}$ for 2 hours.	57
Figure 4.2 XRD patterns for the NZF ceramics sintered for durations up to 18 hours. The ceramics contained 1.0wt% CaF_2	58
Figure 4.3 Variation in the degree of densification of the ferrite ceramics containing different amounts of CaF_2 with soak duration.....	62
Figure 4.4 SEM image obtained from fracture surface of CaF_2 -free NZF ceramic. The sample was soaked at $1200\text{ }^\circ\text{C}$ for 2 hours.	64

Figure 4.5 SEM fractograph of the NZF ceramic containing 0.5wt% CaF ₂ . The ceramic was soaked for 2 hours at 1200 °C.	65
Figure 4.6 SEM micrograph of the NZF ceramic containing 0.5 wt% CaF ₂ . The sample was soaked for 2 hours at 1200 °C and etched.	65
Figure 4.7 SEM fractograph of the NZF ceramic containing 0.75 wt% CaF ₂ . Sample was soaked at 1200 °C for 2 hours.	66
Figure 4.8 SEM micrograph of the NZF ceramic containing 0.75 wt% CaF ₂ . The ceramic was soaked for 2 hours at 1200 °C.	67
Figure 4.9 SEM fractograph of the NZF ceramic containing 1.0wt% CaF ₂ . The ceramic was soaked for 2 hours at 1200 °C.	68
Figure 4.10 SEM micrograph of the NZF ceramic containing 1.0 wt% CaF ₂ . The sample was soaked for 2 hours at 1200 °C and etched.	68
Figure 4.11 SEM fractograph of the NZF ceramic containing 0.5wt% CaF ₂ . Sample was soaked at 1200 °C for 18 hours.	69
Figure 4.12 The EDS pattern of a grain boundary in the NZF ceramic containing 0.5 wt% CaF ₂	70
Figure 4.13 The EDS pattern of grain interior in the NZF tablet doped with 0.5 wt% CaF ₂	70
Figure 4.14 SEM fractograph of the NZF ceramic containing 1.0wt% CaF ₂ . Sample was soaked at 1200 °C for 2 hours.	71
Figure 4.15 The EDS pattern obtained from the grain boundary of NZF ceramic containing 1.0wt% CaF ₂	72
Figure 4.16 The EDS pattern of grain interior of 1.0wt% CaF ₂ added NZF disk.	72
Figure 4.17 The optical micrograph of the NZF ceramic containing no CaF ₂ . The sample was soaked for 18 hours at 1200 °C.....	74
Figure 4.18 Optical micrograph of the ferrite containing 0.5wt% CaF ₂ . The sample was sintered for 18 hours at 1200 °C.	75
Figure 4.19 The microstructure of 0.75wt% CaF ₂ incorporated NZF sample after sintering at 1200 °C for 18 hours.	76

Figure 4.20 Optical micrograph of the NZF ceramic containing 1.0 wt% CaF ₂ . The ceramic was soaked for 18 hours at 1200 °C.	76
Figure 4.21 Experimentally determined grain size distribution in the NZF ceramic containing 0.5 wt% CaF ₂ . The sample was soaked at 1200 °C for 18 hours.	78
Figure 4.22 The effect of soaking time on average grain size of the NZF ceramics containing various amounts of CaF ₂	80
Figure 4.23 Variation in average grain size of the NZF ceramics with CaF ₂ addition for different soaking durations.	81
Figure 4.24 Effect of CaF ₂ content on densification behavior of NZF ceramics.	85
Figure 4.25 The variation in DC electrical resistivity of the NZF ceramics with respect to average grain size for various amount of CaF ₂ additions.	89
Figure 4.26 The effect of CaF ₂ on the electrical resistivity of NZF ceramics studied in this thesis.	90
Figure 4.27 Variation of the dielectric constant of the NZF ceramics with frequency and sintering duration.	91
Figure 4.28 The effect of CaF ₂ additions on the dielectric constant of NZF ceramics containing CaF ₂ . Soak duration 2 hours.	92
Figure 4.29 The effect of CaF ₂ additions on the dielectric constant of NZF ceramics containing CaF ₂ . Soak duration 6 hours.	93
Figure 4.30 The effect of CaF ₂ additions on the dielectric constant of NZF ceramics containing CaF ₂ . Soak duration 12 hours.	94
Figure 4.31 The effect of CaF ₂ additions on the dielectric constant of NZF ceramics containing CaF ₂ . Soak duration 18 hours.	94
Figure 4.32 The effect of the sintering duration on the dielectric loss factor of the NZF ceramics without CaF ₂ addition.	96
Figure 4.33 The dielectric loss factor spectra for the NZF ceramics containing 0.5 wt% CaF ₂	97
Figure 4.34 The dielectric loss factor spectra for the NZF ceramic containing 0.75 wt% CaF ₂	98
Figure 4.35 The dielectric loss spectra for the NZF ceramic containing 1.0 wt% CaF ₂	98

Figure 4.36 The dispersion of initial permeability with frequency in NZF ceramics without CaF ₂	101
Figure 4.37 The dispersion of initial permeability with frequency in NZF ceramics containing 0.5 wt% CaF ₂	102
Figure 4.38 The dispersion of initial permeability with frequency in NZF ceramics containing 0.75 wt% CaF ₂	102
Figure 4.39 The dispersion of initial permeability with frequency in NZF ceramics containing 1.0 wt% CaF ₂	103
Figure 4.40 RLF spectra of NZF ceramics without CaF ₂ addition.....	104
Figure 4.41 The frequency response of RLF in NZF ceramics containing 0.5 wt% CaF ₂	105
Figure 4.42 The frequency response of RLF in NZF ceramics containing 0.75 wt% CaF ₂	105
Figure 4.43 The frequency response of RLF in NZF ceramics containing 1.0 wt% CaF ₂	106
Figure 4.44 The hysteresis curves of pure NZF ceramics fired at 1200 °C with different soak durations.	107
Figure 4.45 The hysteresis behavior of NZF ceramics containing 0.5 wt% CaF ₂	108
Figure 4.46 The hysteresis behavior of NZF ceramics containing 0.75 wt% CaF ₂	108
Figure 4.47 The hysteresis behavior of NZF ceramics containing 1.0 wt% CaF ₂	109
Figure 4.48 Variation in coercivity of NZF ceramics with CaF ₂ content and sintering duration.....	111
Figure 4.49 Variations in remanent magnetization (a) and saturation magnetization (b) of NZF ceramics doped with CaF ₂	112
Figure 5.1 Comparison of the NZF ceramics produced via mixed oxide route in this study to the one manufactured by the citrate precursor method.....	116
Figure 5.2 The dependency of coercive field strength on average grain size of NZF ceramics.	117

Figure A.1 The grain size distribution of NZF sample containing 0.5 wt% CaF ₂ . The ceramic was soaked for 2 hours at 1200 °C.	128
Figure A.2 The grain size distribution of NZF sample containing 0.5 wt% CaF ₂ . The ceramic was soaked for 6 hours at 1200 °C.	129
Figure A.3 The grain size distribution of NZF sample containing 0.5 wt% CaF ₂ . The ceramic was soaked for 12 hours at 1200 °C.	129
Figure A.4 The grain size distribution of NZF sample containing 0.5 wt% CaF ₂ . The ceramic was soaked for 18 hours at 1200 °C.	130
Figure A.5 The grain size distribution of NZF sample containing 0.75 wt% CaF ₂ . The ceramic was soaked for 2 hours at 1200 °C.	130
Figure A.6 The grain size distribution of NZF sample containing 0.75 wt% CaF ₂ . The ceramic was soaked for 6 hours at 1200 °C.	131
Figure A.7 The grain size distribution of NZF sample containing 0.75 wt% CaF ₂ . The ceramic was soaked for 12 hours at 1200 °C.	131
Figure A.8 The grain size distribution of NZF sample containing 0.75 wt% CaF ₂ . The ceramic was soaked for 18 hours at 1200 °C.	132
Figure A.9 The grain size distribution of NZF sample containing 1.0 wt% CaF ₂ . The ceramic was soaked for 2 hours at 1200 °C.	132
Figure A.10 The grain size distribution of NZF sample containing 1.0 wt% CaF ₂ . The ceramic was soaked for 6 hours at 1200 °C.	133
Figure A.11 The grain size distribution of NZF sample containing 1.0 wt% CaF ₂ . The ceramic was soaked for 12 hours at 1200 °C.	133
Figure A.12 The grain size distribution of NZF sample containing 1.0 wt% CaF ₂ . The ceramic was soaked for 18 hours at 1200 °C.	134

CHAPTER 1

INTRODUCTION

The drastic progress in the development and growth of electronic ceramics since the era of post Second World War II has played a major role in the transformation of the society from Steel Age to the Information Age. Nearly instantaneous satellite communications from coast to coast and around the world would not be possible without simultaneous advances in semiconductors, dielectrics, ferroelectrics, ferrites and optoelectronics. The continued developments in these fields have been matched, and perhaps eventually superseded, with advances in superconducting ceramics, photonics, optical waveguides and potentially in optical computing and information processing [1].

In connection with advances in communication technologies, magnetic ceramics have been investigated due to their vastly intriguing properties such as magnetization behavior, high magnetic permeability and high electrical resistivity [2]. These intrinsic material properties have made them indispensably the most versatile engineering ceramics for high frequency applications including power transformers, antennas, faraday rotators, etc [3].

The magnetic ceramics, known also as ferrites due to the dominance of the ferrite (Fe_2O_3) compound as the major crystalline phase in these ceramics, can be categorized into three groups. Hexagonal ferrites constitute the first group. They have been distinguished due to their high uniaxial magnetocrystalline anisotropy which renders them perfect for permanent (hard) magnet applications [4]. The second group is the garnet type ferrites. Garnets are unique magnetic ceramics that provide the transparency required for magneto-optical applications [5].

The last group is known as the spinel ferrites. Spinel ferrites exhibit soft magnetic behavior; i.e., they can be magnetized or demagnetized rather easily by externally applied magnetic fields. They are alternative to metallic magnets such as Fe and layered Fe-Si alloys, but exhibit enhanced performance due to their outstanding magnetic properties [6, 7]. The two popular ceramic magnets; nickel zinc ferrites (NZF) and manganese zinc ferrites (MZF) are the major members of the spinel ferrite family. They have been intriguing ceramic materials due to their high electrical resistivity, high magnetic permeability and possible modification of intrinsic properties over a wide spectrum [1].

The manganese zinc ferrite family of magnetic ceramics has been developed basically due to their extraordinarily high initial magnetic permeability [8-10]. In communication systems operating under high frequencies, however, the use of these ceramics causes problems because of premature dielectric breakdown or mal-functioning due to their high electrical conductivity. Overheating caused by Eddy currents may lead to premature breakdown and mal-functioning.

Nickel zinc ferrites proved to be the preferred ceramic material for high frequency applications in which Eddy current suppression is of primary consideration [11]. Although NZF ceramics have high electrical resistivity to prevent Eddy current generation, they have moderate magnetic permeability compared to manganese zinc ferrites. Like in the MZF group, the electrical and magnetic properties of this particular group of ferrites depend strongly on the microstructural features such as grain size, grain size distribution, the nature of grain boundaries and the extent and nature of porosity. These factors are controlled critically by the chemical composition and by the practice followed in high temperature processing, i.e., the sintering process involved in the production of NZF ceramics [12-18].

The sintering of NZF ceramics is quite easier than the one in MZF production due to the simplicity of the atmosphere control. While the MZF family requires a close control of redox conditions prevailing in the sintering chamber during the firing and the cooling process, in the case of NZF ceramics these operations are conducted in air. Against this advantage, the temperatures involved in firing the NZF ceramics are rather high. This causes difficulties in maintaining uniformity in grain size and control of pore structure.

The aim of the present thesis study was to search for additives which would allow manufacturing NZF ceramics at sintering temperatures lower than those normally encountered in NZF production. The main focus of the thesis work was the production of dense and microstructurally tailored NZF samples of composition $\text{Ni}_{0.5}\text{Zn}_{0.5}\text{Fe}_2\text{O}_4$ which could be fired at relatively low sintering temperatures. The initial experiments on candidate additives revealed that small amounts of calcium fluoride, CaF_2 , could be quite instrumental in achieving enhanced densification during the sintering process. Thus, emphasis was placed on the optimization of the amount of CaF_2 used in the NZF production and on the study of its effects on the magnetic properties. The kinetics of densification, variations in the microstructures and alterations in magnetic and electrical properties of the NZF ceramics sintered in the presence of CaF_2 additions or otherwise were the central themes of concern in this thesis study.

CHAPTER 2

LITERATURE SURVEY

2.1 Ferrites

The history of ferrites began many centuries ago with the discovery of lodestone consisting of the black ore magnetite (ferrous ferrite, $\text{FeO}\cdot\text{Fe}_2\text{O}_3$), which would attract iron. Believed to be discovered in ancient civilizations, magnetite was first used by Chinese navigators in compasses around 1000 BC or perhaps even earlier [7].

A first milestone in the history of magnetism was the work done by William Gilbert in 1600 describing the magnetic properties of lodestone up to that point in time. It was not until 200 years later that major developments occurred. The new science of electromagnetism was developed through the work of H.C. Oersted, A.M. Ampere, W.E. Weber, M. Faraday, P. Curie, J.C. Maxwell, and many others [19].

In 1909, the first attempt to improve the magnetic properties of magnetite was made by Hilpert [6]. The crystal structure of magnetite, the spinel structure, was explained in 1915 by Bragg and Nishikawa [19]. The basis of electromagnetic theory in general and the crystal structures of related materials were gotten to known by researches.

In order to prepare ferrites with better qualifications, precipitation and heat treatment techniques were first performed by Forestier in 1928 [6]. The major contributions to reveal the physics operating in ferrites were achieved both by the researches conducted in Japan by V. Kato et. al. from 1932 to 1935 and the

studies carried out by Snoek et. al. at Philips Laboratories in the Netherlands between 1936 and 1945 [6,19]. Finally in 1945, the basic physics and technology of practical ferrite materials were described by Snoek who initiated and pursued the development of ferrites into useful materials [5]. In 1948, ferrimagnetism theory; describing the basic phenomenon of spin-spin interaction taking place in the magnetic sublattices in ferrites, was set by Néel [19].

The major booming of the ferrite industry was led by the large-scale introduction of television in the 1950s. In television sets, ferrite cores were used as high-voltage transformers and electron beam deflection yokes due to their strong magnetic properties, high electrical resistivity and low magnetic losses. In 1959, J. Smit and H.P.J. Wijn published a comprehensive book on ferrites. Since then, developments have been made on the magnetic characteristics of ferrite materials that have improved device performances. These involve both compositional and processing modifications in addition to improvements succeeded in device design. A very wide range of Curie points, remanent magnetization, saturation magnetization and coercive fields have been obtained due to wide range of substitutional solid solution that makes it possible to tailor the magnetic properties of polycrystalline magnetic ceramics. Thus, ceramic magnets could be molecularly designed and processed for specific electronic applications [19, 20].

Currently, applications of ferrites have been established in many branches of communication and electronic engineering. Typical applications include: audio and video recording tapes, motors, generators, videocassette recorders, computer disks, and high frequency inductor and transformer cores [5]. The examples for uses of ferrite cores are summarized in Table 2.1.

Table 2.1 Various types of soft ferrite cores with their area of utilization [19].

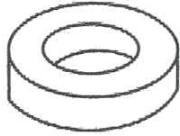
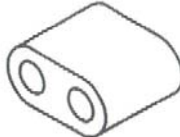
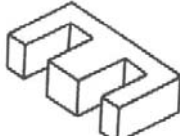
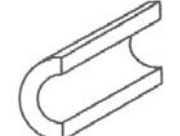
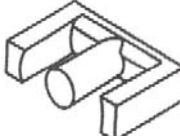
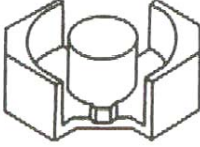
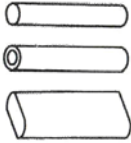
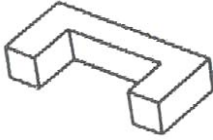
Ferrite Geometry	Type	Description	Uses
	Toroid	Very good magnetic shielding, low material cost but very high assembly cost	Broadband and pulse transformers, common mode chokes
	Balun Core	Excellent magnetic shielding, high cost	Broadband and pulse transformers, common mode chokes
	E Core	External magnetic field generated close to the exposing winding, de facto standard, low cost	Power transformers and inductors
	EMI Core	Good magnetic shielding, high cost	Cable EMI suppression
	EP Core	Very good magnetic shielding, de facto standard, high cost	Power transformers
	ETD Core	External magnetic field generated close to the exposing winding, IEC core standard, very low cost	Power transformers and inductors
	Planar Core	Good magnetic shielding, average cost	Low profile SMD of power transformers

Table 2.1 (Continued)

	Pot Core	Very good magnetic shielding, IEC core standard, high cost	High Q inductors and tuned transformers
	RM Core	Good magnetic shielding, IEC core standard, high cost	High Q inductors and tuned transformers
	Rods Tubes Stripes	Very poor magnetic shielding, very low cost	Antennas and high frequency welding
	U Core	External magnetic field generated close to the exposing winding, low cost	Power transformers and inductors

2.1.1 Classification of Ferrites

The subclasses of ferrite family are magnetoplumbites (hard magnets), spinel ferrites (soft magnets or soft ferrites), and garnets. These are distinguished with respect to the molar ratio of Fe_2O_3 to the other oxide components present in the ceramic as shown in Table 2.2. The magnetoplumbite family exhibits permanent magnetism. Garnets have optical transparency that let them be used in magneto-optical applications. Spinel ferrites have intriguing intrinsic properties such as high electrical resistivity and low magnetic losses. Among these classes, spinel ferrites represent the widest subclass. Nickel zinc ferrite, which has been the subject of the present thesis work, is an important member in the spinel ferrites subclass.

Table 2.2 Summary of ferrite crystal structure types, typified by changes in the $\text{Fe}_2\text{O}_3 - \text{MeO}$ (or Me_2O_3) modifier oxide ratios [19].

Magnetoplumbite	$6 \text{Fe}_2\text{O}_3 - 1 \text{MeO}$	where MeO is a divalent metal oxide from group IIA – BaO, CaO, SrO
Spinel	$1 \text{Fe}_2\text{O}_3 - 1 \text{MeO}$	where MeO is a transition metal oxide
Garnet	$5 \text{Fe}_2\text{O}_3 - 3 \text{Me}_2\text{O}_3$	where Me_2O_3 is a rare earth metal oxide

2.1.2 Crystal Structure of Spinel Ferrites

The crystal structure of soft ferrites is cubic as indicated by the atomic arrangements given in Figures 2.1 and 2.2. The structure is the same as that of the naturally occurring mineral spinel, MgAl_2O_4 . In some texts, the general formula for spinel is written as AB_2O_4 where A stands for a divalent cation such as Ca^{+2} , Mg^{+2} , Co^{+2} , etc., and B stands for the trivalent cations like Al^{+3} , Fe^{+3} , or Cr^{+3} . The formula of the ferrite may be written as $\text{MeO} \cdot \text{Fe}_2\text{O}_3$ or sometimes as MeFe_2O_4 . In this formula, Me represents the divalent metal cation, Me^{+2} . The ferrite compound is named after its Me^{+2} cation; i.e., $\text{CuO} \cdot \text{Fe}_2\text{O}_3$ is called copper ferrite.

The unit cell of spinel ferrite is made up of 8 formula units of $\text{MeO} \cdot \text{Fe}_2\text{O}_3$ making a total of 56 atoms per unit cell. The 32 oxygen ions (O^{2-}) are arranged in cubic close packing, which accommodate tetrahedral (A) and octahedral (B) sites (sublattices) for metal cations. 8 of the 64 available tetrahedral sites and half of the 32 available octahedral sites are occupied by cations [19].

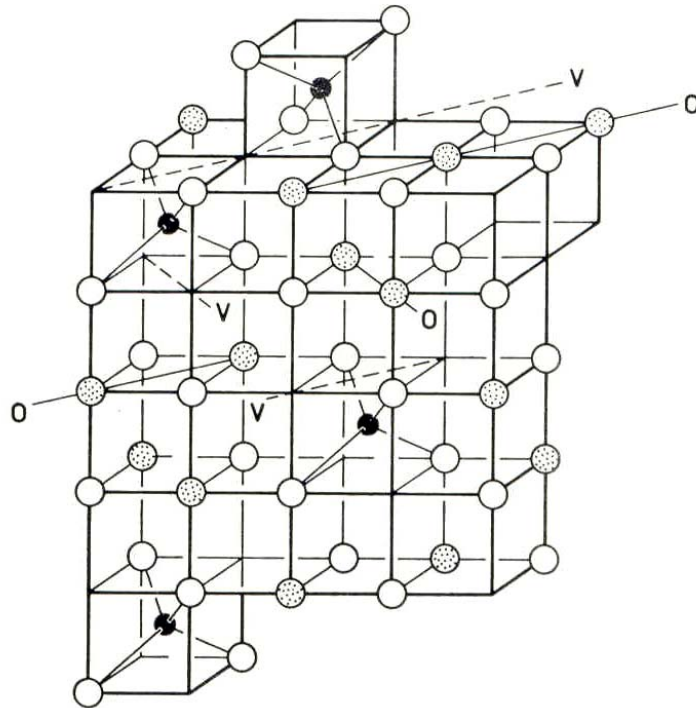


Figure 2.1 Structure of spinel; open circles are oxygen ions, full circles are Me^{+2} cations and shaded circles are Fe^{+3} cations. Only one layer (100) is shown for the sake of clarity [21].

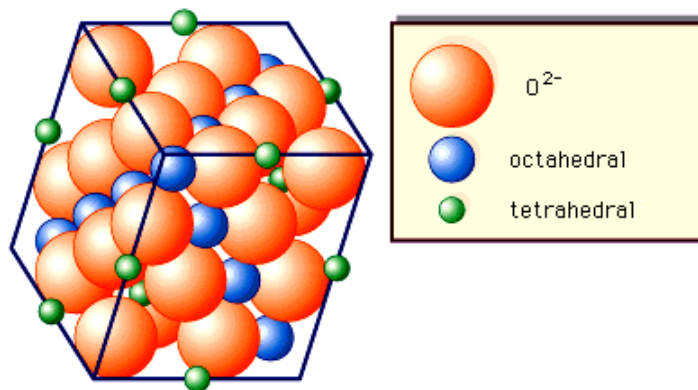


Figure 2.2 Sphere model of the spinel structure revealing tetrahedral and octahedral sites between oxygen anions [22].

2.1.3 Cation Distribution in Spinel Ferrites

The cations in the spinel ferrite may distribute themselves between the tetrahedral sites and octahedral sites in accordance with their site preference energies. When cations of (+2) charge are all located on the tetrahedral sites and cations of (+3) charge are all located on octahedral positions the compound is called as “normal spinel.” This is the situation encountered in zinc or cadmium ferrites. In contrast to this, some ferrites have half of their (+3) cations occupy tetrahedral sites while the other half remain on octahedrals, while all (+2) cations migrate to octahedral positions. In this case the compound becomes an “inverse spinel.” The octahedral site preference energies of the cations like Ni^{+2} , Fe^{+2} , Mn^{+2} , and Cu^{+2} are much higher than their tetrahedral site preference energies, therefore the ferrites of these cations assume inverse structure. It is worth to mention that no site preference has been detected for ferric ion, Fe^{+3} [1,5,19].

The distribution of cations on different sites of the spinel is designated by using bracket notation. Round brackets are used for divalent or trivalent cations on the tetrahedral sites; square brackets are used for cations occupying the octahedral sites. Thus, the zinc ferrite, which is has a normal spinel structure is represented as $(\text{Zn}^{+2})[\text{Fe}^{+3}]_2\text{O}_4$. On the other hand, the iron ferrite, magnetite, which is an inverse spinel is represented as $(\text{Fe}^{+3})[\text{Fe}^{+2}\text{Fe}^{+3}]\text{O}_4$. In some ferrites, part of the divalent cations can be distributed over the tetrahedral sites and the remaining part may occupy octahedral positions. In such cases the ferrite attains the so-called “mixed spinel” structure. For example, in nickel ferrite 90 percent of the nickel cations occupy the octahedral positions. In this case the ferrite is denoted as $(0.9\text{Fe}^{+3}0.1\text{Ni}^{+2})[0.9\text{Ni}^{+2}1.1\text{Fe}^{+3}]\text{O}_4$. In general, the mixed ferrite can be represented as $(x\text{Fe}^{+3}(1-x)\text{Me}^{+2})[(x\text{Me}^{+2}(2-x)\text{Fe}^{+3})\text{O}_4$ where x represents the degree of inversion and can take values between 0 and 1. Heat treatment processes involving slow cooling or quenching may be instrumental in obtaining different values for the degree of inversion [5].

The compositional diversity in soft ferrites has become possible due to the ability of forming complete solid solution series among different soft ferrites. A variety of specific magnetic properties required for certain applications could be attained in this manner [5]. The nickel zinc ferrite, a solid solution of nickel ferrite and zinc ferrite; $(x\text{Zn}^{+2}(1-x)\text{Fe}^{+3})[(1-x)\text{Ni}^{+2}(1+x)\text{Fe}^{+3}]\text{O}_4$ where x is the mole of ZnO, has been engineered by using this concept.

2.2 Magnetism in Ferrites

The nature of ferrimagnetism and hence the resultant magnetic properties has emanated from the spin-spin interaction of cations available in the sublattices of the ferrite. A wide range of compositions and magnetic properties could be secured by substituting various kinds of cations on different sublattices. The magnetic moments of cations on each sublattice tends to arrange themselves antiferromagnetically that is antiparallel to each other. The direction of arrangement with respect to each other, being parallel or antiparallel, is determined by the so-called exchange (coupling or interaction) energy, E_{ex} , given by the following expression [1, 23]:

$$E_{\text{ex}} = -2.J.\vec{S}_1.\vec{S}_2.\cos\phi, \quad (2.1)$$

here, \vec{S}_1 and \vec{S}_2 are the magnitudes of the spin vectors of electron no 1 and no 2, respectively and ϕ is the angle between their spin vectors. The term J is the exchange integral; it is defined as [1]:

$$J = \int \Psi_a(1)\Psi_b(2)\Psi_a(2)\Psi_b(1) \left(\frac{1}{a} - \frac{1}{a_2} - \frac{1}{a_1} + \frac{1}{r_{12}} \right) dt, \quad (2.2)$$

where a is the lattice separation, a_2 is the distance between electron no 2 and atom no 1, a_1 is the distance between electron no 1 and atom no 2, and r_{12} is the distance between electrons.

The total energy of a system consisting of two magnetic moments is decreased if the moments are coupled with each other. Parallel or antiparallel alignment of magnetic moments is a consequence of the sign of the coupling energy. The magnetic moments are arranged antiferromagnetically (antiparallel) to each other if the exchange energy is positive or vice versa. In the case of ferrites antiparallel alignment of magnetic moments on different sublattices has been observed. However a net magnetization (total magnetic moment) results due to the fact that the magnitude of the total magnetic moments in each sublattice differs from each other. The net magnetic moment can be calculated by the summation of magnetic moments of tetrahedral and octahedral sites [1].

For nickel zinc ferrites of composition $x\text{ZnO}+(1-x)\text{NiO}+\text{Fe}_2\text{O}_3$, that is $(x\text{Zn}^{+2}(1-x)\text{Fe}^{+3})[(1-x)\text{Ni}^{+2}(1+x)\text{Fe}^{+3}]\text{O}_4$, the total magnetic moment on tetrahedral sites results only from the contribution of Fe^{+3} cations as Zn^{+2} cations possess no unpaired electron(s). The magnetic moment per ferric cation (Fe^{+3}) is 5 Bohr magnetons (μ_B) due to five unpaired electrons in d-orbitals. Therefore tetrahedral sites provide $5 \cdot (1-x) \cdot \mu_B$ to the lattice. In the same manner, the total magnetic moment on octahedral sites is $[2 \cdot (1-x) + 5 \cdot (1+x)] \cdot \mu_B$ where the first term is due to Ni^{+2} cations and the latter stands for Fe^{+3} cations. The net magnetization of the lattice is the difference of two sublattices as they are in an antiparallel arrangement, $[2 \cdot (1-x) + 5 \cdot (1+x) - 5 \cdot (1-x)] \cdot \mu_B = (2 + 8x) \cdot \mu_B$ [24]. The change of net magnetization with amount of ZnFe_2O_4 for various mixed ferrites is given in Figure 2.3.

After a certain amount of ZnFe_2O_4 addition, the net magnetization is decreased due to the increasing amount of paramagnetic Zn cations in tetrahedral sites. This effect is called as magnetic dilution of tetrahedral sites. The strength of interaction between tetrahedral and octahedral sites is weakened due to dilution of tetrahedral sites. As a result of this, the B-B interaction dominates in the system and the magnetic moments present in octahedral sites, align themselves

antiparallel to each other. Thus the saturation magnetization of ferrite drops as a result of the realignment of moments on octahedral sites [19,24].

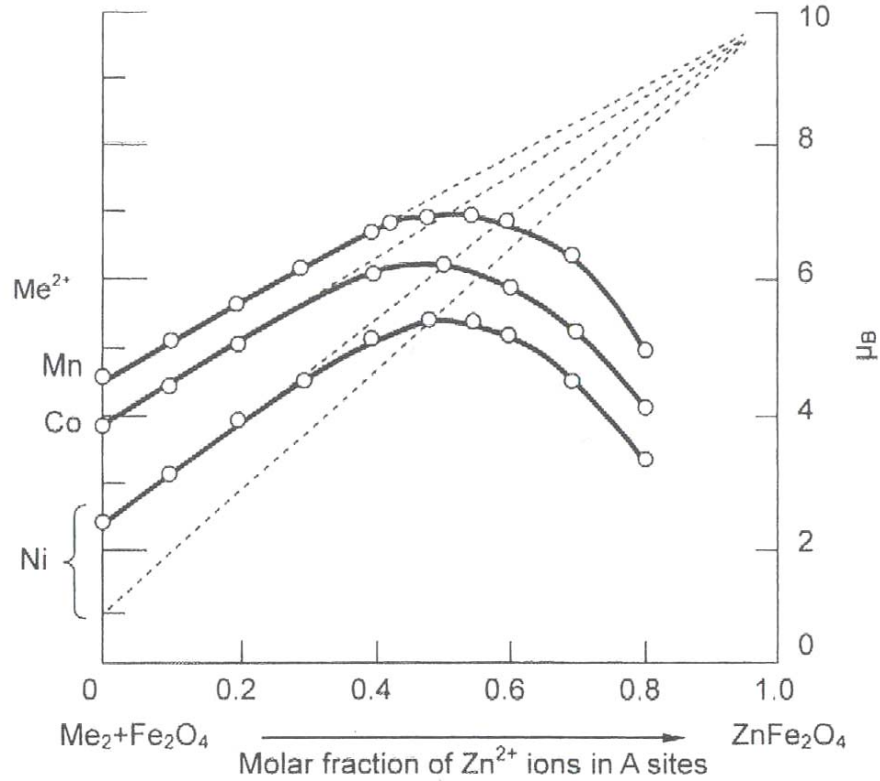


Figure 2.3 Effect of ZnFe_2O_4 addition on the magnetization of the ferrites of Ni, Co, and Mn. Increased saturation magnetization effects should be noted [19].

2.2.1 Curie Temperature

The Curie temperature, T_C , of the ferrite ceramic at which the thermal agitation causes the magnetic moments to become randomly aligned, is decreased with addition of zinc ferrite as shown in Figure 2.4. This effect indicates an attenuation in the strength of interaction between A and B sites. Curie temperature is important because it determines the temperature limit for the application of the ferrite [19].

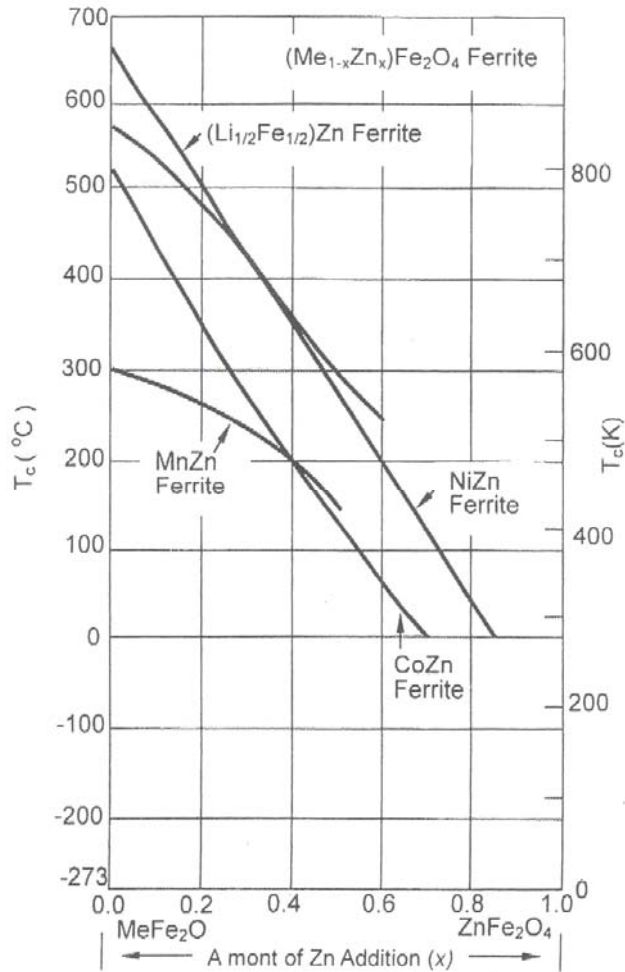


Figure 2.4 Depression of the magnetic Curie temperature, T_c , with Zn additions to Mn, Co, Ni, and Li/Fe ferrites [19].

2.2.2 Anisotropy

The magnetic properties and the process of magnetization of ferrites are constrained with intrinsic crystallographic features imposed by the crystal structure. Due to these restrictions ferrites are categorized as anisotropic magnets. There are three anisotropy factors controlling the magnetic behavior of a ferrite. First one is the magnetocrystalline anisotropy energy, which favors the spin alignment in an easy crystallographic direction. It is a measure of the ease with which magnetic moments can be oriented in the direction of the applied magnetic

field. In cubic lattices like spinels, the magnetocrystalline anisotropy energy, E_a , can be given in a Taylor series expansion as:

$$E_a = K_1 (\alpha_1^2 \cdot \alpha_2^2 + \alpha_2^2 \cdot \alpha_3^2 + \alpha_1^2 \cdot \alpha_3^2) + K_2 (\alpha_1^2 \cdot \alpha_2^2 \cdot \alpha_3^2) + \dots, \quad (2.3)$$

where: K_1 and K_2 : magnetocrystalline anisotropy constants,
 α_i : direction cosines of the magnetization vector relative to the crystallographic axes [5].

The crystallographic direction of magnetization, minimum of E_a , is determined by the signs and values of K_1 and K_2 parameters. The magnitudes of these constants can be adjusted by chemical modifications. They also change by service temperature of ferrite [2, 5]. As long as it is allowed, the K_2 term in Equation (2.3) can be neglected rendering the magnetization direction dependent only on K_1 . Therefore a low value of K_1 indicates that the energy barrier, anisotropy energy, that must be exceeded by an externally applied magnetic field in order to deflect the orientation of magnetic moments is decreased. Hence especially initial magnetization process is rendered quiet easy and initial magnetic permeability is enhanced.

Second type of restriction is the magnetostrictive energy which is related to the presence of strain or stress on the sample. The last type of restriction is the magnetostatic energy caused by the geometry of the ferrite [5].

2.3 Electrical Resistivity

Nickel zinc ferrites have been indispensably used in high frequency applications due to their high electrical resistivity and low magnetic losses. The Eddy currents produced by the alternating magnetic fields, which many devices generate, are limited in ferrites by their high intrinsic resistivities. To keep Eddy

currents to a minimum becomes of paramount importance as the operating frequency increases. Approximately, the loss generated by eddy currents is inversely proportional with the electrical resistivity of the ferrite [6].

The resistivity of nickel zinc ferrites can be tailored precisely with chemical modifications and microstructural features. The change of DC electrical resistivity lies in a wide range from 10^3 to 10^{11} Ω -cm. The effect of microstructure on DC resistivity of ferrites can be explained on the basis of the composite behavior of ferrites. The resistance to electron flow through the bulk of the NZF changes from grain interior to grain boundary regions. A semiconducting behavior is observed in grains whereas the grain boundaries act as an insulator. Thus the resistivity of NZF mainly arises from the contribution of grain boundaries. Therefore a decrease in volume fraction of grain boundaries results in a reduction of the electrical resistivity of NZF [2].

The volume fraction of grain boundaries in a fully dense ceramic can be given proportional to the grain boundary surface area per unit volume (S_v). For a ceramic consisting of tetrakaidecahedral grains like in Figure 2.5, the S_v parameter is given as:

$$S_v = \frac{7.1023}{\bar{D}} \cdot (\exp -(2.5 \cdot \ln^2 \sigma)), \quad (2.4)$$

where: \bar{D} : the average grain size,
 $\ln \sigma$: the standard deviation of the log normal distribution.

Equation (2.4) was derived by Mendelson [25], on the assumption of a log-normal grain size distribution. Since S_v varies inversely proportional with the average grain size, the resistivity of the ferrite is decreased as the grain size is increased.

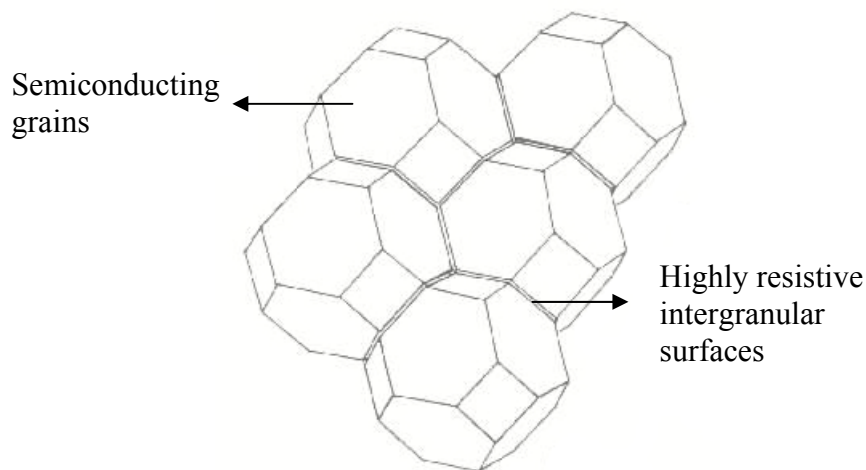


Figure 2.5 A cluster of tetrakaidecahedral grains with insulating boundary surfaces between them.

The electrical conduction in ferrites occurs by the movement of an electron with its associated elastic distortion field which is known as polaron hopping. The hopping of electron takes place between multivalent cations of the same atom located at crystallographically equivalent lattice sites [26]. Therefore attention must be paid on cations in the lattice which exhibits multivalent character. In NZF, the multivalent behavior has been observed for cations of iron according to the reaction:



Therefore, in order to obtain high resistivity values in NZF, the concentration of ferrous (Fe^{+2}) cations must be controlled closely and be kept low. The formation of ferrous cations can be avoided by keeping the sintering temperature low and maintaining high partial pressures of oxygen during firing [2, 27].

2.4 Microstructure

The control of microstructure evolution is of primary interest in manufacturing ferrites with high permeabilities and low magnetic losses. Most of the progress achieved in the development of superior MnZn ferrites can also be applied to NZF manufacture. The parameters that must be controlled intentionally can be classified as the density, the distribution of pores, the average grain size and the grain size distribution. Dense samples are required to minimize the demagnetizing effects of pores in the sample. The pores that remain after sintering should be located at grain boundaries in order to avoid pinning of domain walls, which moves during magnetization process. Fine or coarse grains may be preferred depending on the type of application. Uniform grain size is desired to keep the magnetization in all grains similar to each other [12-18].

The microstructural features of any ceramic article are set by the characteristics of the processing steps. The two fundamental steps to be checked carefully can be mentioned as the powder synthesis and the method of sintering.

2.4.1 Powder Characteristics

Chemical and physical characteristics of the powder such as purity, particle size, and defect structure of the particle in terms of deviation from stoichiometric composition play a crucial role during sintering and thus impose a dominant effect on evolution of microstructure.

2.4.1.1 Effect of Particle Size

The effect of particle size in sintering is related to the concept of total surface energy of the greenware. The driving force, in sintering being the total surface energy, is increased by decreasing the particle size. As the particle size of the powder is decreased a higher surface area to volume ratio is obtained. Therefore

the total surface energy per unit mass is increased. Due to the promoted driving force, the peak temperature required for sintering process can be lowered.

A decrease in sintering temperature prevents the volatilization of Zn and the decomposition of the ferrite at high temperatures [13]. Structural integrity and structural perfection can be preserved more easily when the ferrite is fired at low temperature. In addition, the possibility of the occurrence of discontinuous grain growth may also diminish at lower sintering temperature.

Powder synthesis methods such as co-precipitation, freeze-drying and spray-drying, were proposed for production of very fine ferrite particles down to 10 nm size [12].

2.4.1.2 Effect of Defect Structure of Particles

The microstructural features in ionic solids are set by the diffusion of ions during sintering through various mechanisms such as bulk diffusion, grain boundary diffusion, and so forth. In these cases the movement of ions is allowed through available “vacant lattice sites”. The term “sinterability” can be used to indicate the ease of diffusion taking place in an aggregate of particles during firing. The rate of sintering, thereby the sinterability of a particular assemble, is determined by the diffusivity of the slowest diffusing specie which is generally oxygen in oxide ceramics.

The sinterability of ionic solids was investigated in detail by P. J. N. Reijnen [28]. Controlled amounts of lattice defects, “such as anion or cation vacancies”, were generated in an MO (divalent cation oxide) by addition of a L₂O (monovalent cation oxide). The change of sintered density; the sinterability, was checked against the amount of L₂O; a measure of the concentration of defect type induced. Based on the concept developed by P. N. J. Reijnen [28], the normalized anion, O⁻², vacancy flux emitted from surface of a pore with respect to concentration and type of defect was derived as:

$$\frac{\Phi_o}{\Phi_{o,STOICH}} = \frac{\left(1 + \frac{D_c}{D_o}\right) \cdot \left[K_s + \left(\frac{x}{x+1} + C_c - \frac{(1-x)K_i}{(1+x)(K_i+C_c)} \right) \cdot \left(\frac{(1-x)K_i}{(1+x)(K_i+C_c)} \right) \right]}{\left[(1+x) \cdot \left(\frac{x}{x+1} + C_c - \frac{(1-x)K_i}{(1+x)(K_i+C_c)} \right) + \frac{D_c}{D_o} \cdot \left(C_c + \frac{(1-x)K_i}{(1+x)(K_i+C_c)} \right) \right]} \cdot K_s^{1/2}, \quad (2.6)$$

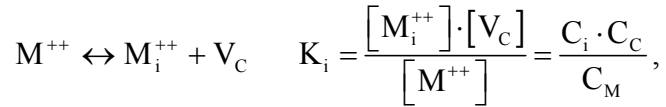
where: Φ_o : oxygen vacancy flux,
 $\Phi_{o,STOICH}$: oxygen vacancy flux for stoichiometric composition,
 D_c : diffusion constant of M cation,
 D_o : diffusion constant of anion (oxygen),
 x : amount of L_2O added in moles,
 K_s : equilibrium constant of the annihilation reaction



C_c : M cation vacancy concentration,

C_o : anion (oxygen) vacancy concentration,

K_i : equilibrium constant of the Frenkel reaction



C_i : concentration of interstitial M cations,

C_M : concentration of M cations on regular lattice sites.

The variation of the concentration of the cation vacancies, C_c , with respect to system parameters K_i , K_s and amount of L_2O added, x , was derived as:

$$C_c^3 + \left(K_i + \frac{x}{x+1} \right) \cdot C_c^2 + \left(\frac{2x-1}{x+1} \cdot K_i - K_s \right) \cdot C_c - K_i K_s = 0, \quad (2.7)$$

One positive (-two negative-) root of Equation (2.7) was substituted into Equation (2.6).

The variation of normalized oxygen vacancy flux with respect to x and K_i is given in Figure 2.6. The K_s and $\frac{D_c}{D_o}$ parameters were assumed to be 10^{-10} and 100, respectively.

It is clearly seen from Figure 2.6, in systems where oxygen anion is the sintering rate determining specie ($D_o \ll D_c$) the diffusivity of the oxygen anions is promoted by generation of oxygen vacancies ($x > 0$). Therefore the sinterability of the powder compact is increased.

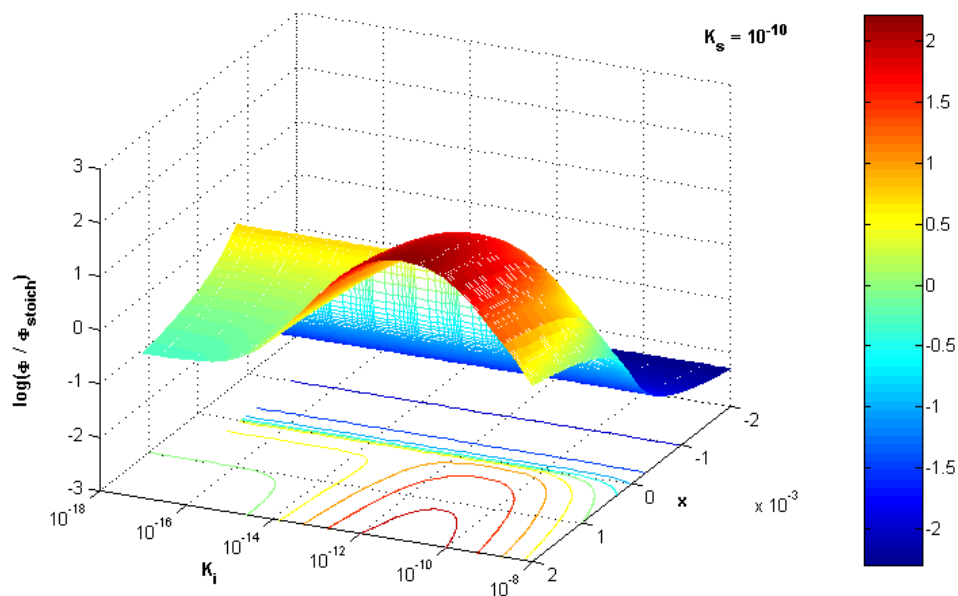


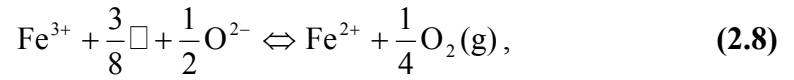
Figure 2.6 The variation of oxygen vacancy flux emitted from a pore in a solid solution of $(1-x) MO + x L_2O$.

2.4.1.2.1 Particles with Excess Fe_2O_3

The diffusivity of ions during sintering is determined to some extent by the defect structure of the particle. The mass transport during sintering occurs mainly by diffusion of ions through the available vacant sites. The rate of sintering is

fixed with the diffusivity of the sluggish ion which is O^{\ominus} in the case of ferrites. Therefore a higher rate of sintering is provided due to a deviation from stoichiometry that results in an increase in concentration of oxygen vacancies in the particle [28].

The non-stoichiometry in ferrites due to variations in the amount of Fe_2O_3 was investigated extensively by P. N. J. Reijnen [28]. Excess Fe_2O_3 was found to dissolve into the spinel lattice partly as γ - Fe_2O_3 with cation vacancies and partly as Fe_3O_4 with formation of Fe^{+2} ions. The equilibrium reaction for dissolution of excess Fe_2O_3 can be given simply as:



where \square stands for cation vacancy [28].

The equilibrium concentrations of both ferrous (Fe^{+2}) cations and cation vacancies can be adjusted by varying sintering temperature and furnace atmosphere. High concentrations of cation vacancies are favored by a high partial pressure of oxygen gas (P_{O_2}) and low sintering temperature. In contrast to this fact, Fe^{+2} formation is assisted with a low P_{O_2} and a high firing temperature [27].

For circumstances favoring the formation of cation vacancies, the sintering rate is diminished due to elimination of oxygen vacancies. In the case of formation of ferrous ions the electrical resistivity of the ferrite is drastically reduced whereas the initial magnetic permeability is maximized [2]. The electrical conduction in ferrites is operated by the hopping of electrons through octahedral sites due to the multivalent behavior of iron cation with respect to the reaction described by Equation (2.5). Thus the electrical resistivity is reduced with increasing concentration of ferrous ions.

In addition to these, the contribution of Fe^{+2} ions to the magnetocrystalline anisotropy constant, K_1 , was found to be positive. As a result of this, the concentration of ferrous ions can be adjusted to obtain a value of K_1 close to zero around room temperature. A diminished value of K_1 implies easy magnetization in ferrite and thereby a high initial magnetic permeability value [2].

The evolution of microstructure in ferrites sintered in an O_2 (g) atmosphere with excess Fe_2O_3 (cation deficient) was found to be controlled with the mobility of pores [28]. During sintering grain growth mechanism can be hindered up to a point by pores due to pinning of grain boundaries. If the force exerted on the pore by the grain boundary is high enough grain boundaries can escape from pores. In addition to these, pores can be swept by grain boundaries if the mobility of the pore is comparable to the grain boundaries' one.

In cation deficient ferrites the mobility of pores is enhanced due to the transfer of oxygen across the pore in gas phase, Figure 2.7, whereas the ferrous ions diffuse through the bulk of crystallites. As a consequence of high pore mobility, the pores are effectively swept by grain boundaries during grain growth and grains remain pore free, Figure 2.8. The disadvantage of high pore mobility is the occurrence of pore growth which retards densification. As a result of pore growth low density values are obtained in cation deficient sintered ferrites [2, 28].

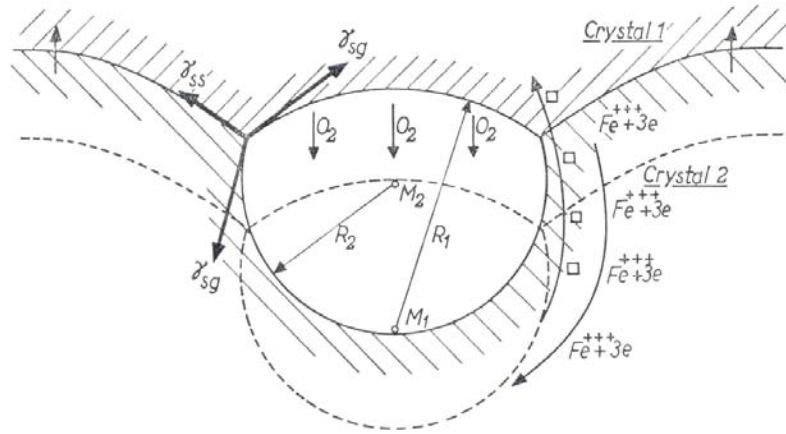


Figure 2.7 Mechanism of pore migration proposed in cation deficient ferrites during firing [28].

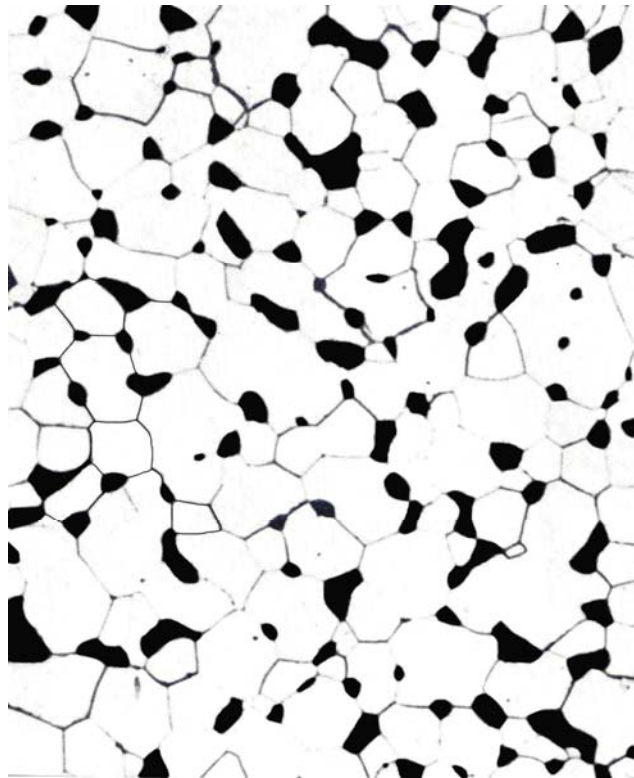


Figure 2.8 Microstructure of a cation deficient ferrite sintered in oxygen. Grains are absolutely free from pores [28].

2.4.1.2.2 Fe₂O₃ Deficient Particles

In the case of Fe₂O₃ deficient ferrites the mobility of the pores are restricted but the sinterability of the ferrite article is enhanced. Fe₂O₃ deficiency results in an increment in the concentration of anion vacancies, and thus the diffusion of oxygen ions through the bulk is promoted. As the oxygen ions are the slowest diffusing specie in the ferrites, the densification rate of the ferrite is increased via ascribing more mobility to oxygen ions.

In contrast to the advantage of anion deficiency mentioned above, the mobility of pores is drastically decreased due to prevention of cation (ferrous ion) diffusion through the bulk of the ferrite. Therefore, pores remain fixed in the grains. As the result of pinning, the pores cannot be swept by grain boundaries during grain growth, therefore, pore growth is avoided. In addition, pore shrinkage is ensured by enhanced densification rate.

A typical microstructure of an anion deficient ferrite is shown in Figure 2.9. The tiny pores trapped in the grains can act as a hindrance to Bloch wall bulging, the essential magnetization mechanism in high permeability ferrites, in initial stages of magnetization. Thus the initial magnetic permeability of the ferrite ceramic is slashed. In contrary to this disadvantage, the magnetic losses encountered due to Bloch wall relaxation at high operation frequencies are avoided [12].

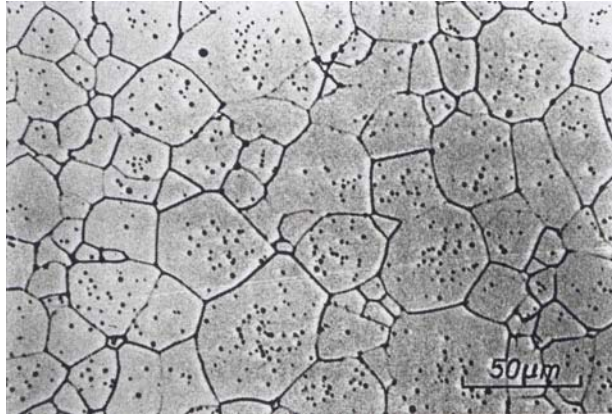


Figure 2.9 Optical micrograph taken from an anion deficient ferrite enlightening trapped tiny pores in grains [12].

2.4.2 Sintering Method

The sintering mechanism reflected in the manner of densification and grain growth can be altered with the way in which sintering process is carried out. Therefore, the final microstructure of the ceramic article can be tailored by changing the parameters involved in sintering. The microstructure of ferrites for high frequency applications is desired to be pore free and consisting of fine grains. One practical way in achieving this objective is the application of pressure on greenware during sintering where the process is known as hot pressing. The application of pressure provokes densification and retards grain growth mechanism. As a result of these benefits, sintering can be conducted at low temperatures and/or at short dwelling times.

On the scope of the content mentioned hitherto, ferrite ceramics having less than 1% porosity were produced from cold isostatically pressed greenwares with utilization of hot pressing. The raw materials used were extremely pure (impurity concentration < 100 ppm), and the particle size was about 0.3 μm [12, 13, 16]. A typical final microstructure is shown in Figure 2.10.

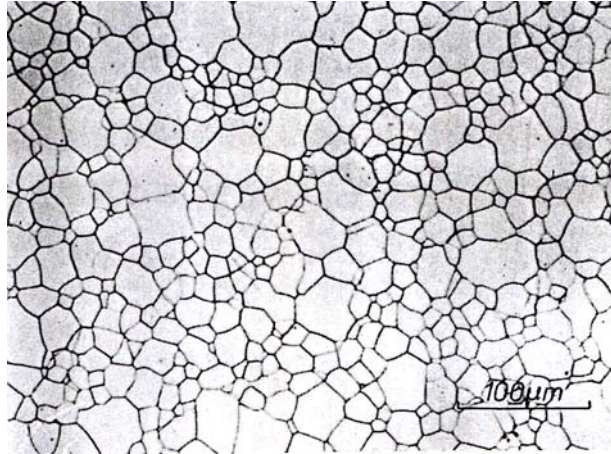


Figure 2.10 The microstructure of a ferrite for microwave frequency applications produced via hot pressing [12].

2.4.3 Chemical Modifications

The electrical and magnetic properties of the NZF ceramics were attempted to be made better via incorporation of various kinds of metal oxides other than the constituting ones. These chemical modifications on the basic NZF system were done as addition or substitution of various kinds of metal oxides. The effects of chemical modifications on various properties of the NZF ceramics are summarized in Table 2.3.

The substitutions mentioned above were done by replacing the cations Ni, Zn or Fe with new ones which can take part in the spinel structure without causing any change in the principal features of the spinel crystal. The substitutions made in this manner aimed to modify the ceramic properties like density, electrical resistivity, saturation magnetization or initial magnetic permeability. For example, Cu has been introduced in place of Ni for increased initial permeability, higher saturation magnetization and lower sintering temperature [29-31]. Co substitution for Ni was found to increase the electrical resistivity [29]. Ca substitution for Ni resulted in lower initial magnetic permeability, μ_i , but the temperature coefficient of μ_i was modified in favor of increased thermal stability [29]. The additions of

elements like La, Gd, Ru, and Y in place of Fe was effective in increasing the electrical resistivity of the ferrite, while Ru caused an increase in μ_i , Y addition had the reverse effect [32, 33].

The NZF ceramics have been known to possess rather low initial magnetic permeabilities as compared to those of the manganese counterparts. Manganese substitution in NZF attracted considerable research interest because of the possibility of obtaining ferrites with μ_i values higher than those of the pure NZF. The results of studies involving Mn substitution [29, 34, 35] for the divalent Ni site in the NZF showed that the resistivity of the ferrite would increase, the dielectric constant would be stabilized, but the rise in μ_i did not meet the expectations.

Table 2.3 Effect of some processing and chemical modifications on electrical and magnetic properties of NZF ceramics.

The symbols are : T_{sint} : peak temperature of sintering, t_{sint} : duration at peak sintering temperature , ρ (gr / cm³) : bulk density of the sintered ceramic, ρ (Ω -cm) : DC electrical resistivity of the ceramic at room temperature, μ_i : initial magnetic permeability, ϵ : dielectric constant, σ_s : saturation magnetization, H_c : coercive field strength.

Ref #	Composition	T_{sint} ($^{\circ}\text{C}$)	t_{sint} (hrs)	ρ (gr/cm ³)	ρ (Ω -cm)	μ_i	ϵ	σ_s (emu/g)	H_c (Oersted)
[29]	$\text{Ni}_{0.5}\text{Zn}_{0.5}\text{Fe}_2\text{O}_4$	1100	4	4,63	$1.32 \cdot 10^5$	304		75,9	
[29]	$\text{Ni}_{0.25}\text{Mg}_{0.25}\text{Zn}_{0.5}\text{Fe}_2\text{O}_4$	1100	4	4,18	$3.00 \cdot 10^5$	396		65,4	
[29]	$\text{Ni}_{0.25}\text{Cu}_{0.25}\text{Zn}_{0.5}\text{Fe}_2\text{O}_4$	1100	4	4,85	$1.64 \cdot 10^5$	1160		75,4	
[29]	$\text{Ni}_{0.25}\text{Co}_{0.25}\text{Zn}_{0.5}\text{Fe}_2\text{O}_4$	1100	4	4,35	$1.51 \cdot 10^7$	4,8		80,6	
[29]	$\text{Ni}_{0.25}\text{Mn}_{0.25}\text{Zn}_{0.5}\text{Fe}_2\text{O}_4$	1100	4	4,22	$3.58 \cdot 10^7$	292		65,5	
[29]	$\text{Ni}_{0.25}\text{Cd}_{0.25}\text{Zn}_{0.5}\text{Fe}_2\text{O}_4$	1100	4	4,58	$3.84 \cdot 10^4$	522		37,9	
[29]	$\text{Ni}_{0.25}\text{Ca}_{0.25}\text{Zn}_{0.5}\text{Fe}_2\text{O}_4$	1100	4	4,35	$1.77 \cdot 10^6$	19,1		35,8	
[32]	$\text{Ni}_{0.5}\text{Zn}_{0.5}\text{Fe}_2\text{O}_4$	1250	4	5,04	$3.66 \cdot 10^4$	275	33 @ 1MHz		
[32]	$\text{Ni}_{0.5}\text{Zn}_{0.5}\text{La}_{0.04}\text{Fe}_{1.96}\text{O}_4$	1250	4	4,78	$5.46 \cdot 10^5$	150	21 @ 1MHz		
[32]	$\text{Ni}_{0.5}\text{Zn}_{0.5}\text{Gd}_{0.04}\text{Fe}_{1.96}\text{O}_4$	1250	4	4,82	$2.80 \cdot 10^5$	150	27 @ 1MHz		
[33]	$\text{Ni}_{0.5}\text{Zn}_{0.5}\text{Fe}_2\text{O}_4$	1100	12		$8.7 \cdot 10^7$	45			
[33]	$\text{Ni}_{0.5}\text{Zn}_{0.5}\text{Gd}_{0.02}\text{Fe}_{1.98}\text{O}_4$	1100	12		$1.0 \cdot 10^9$	50			

Table 2.3 (continued)

Ref #	Composition	T _{Sint} (°C)	t _{Sint} (hrs)	ρ (gr/cm ³)	ρ (Ω-cm)	μ	ε	σ _s (emu/g)	H _c (Oersted)
[33]	Ni _{0.5} Zn _{0.5} Ru _{0.02} Fe _{1.98} O ₄	1100	12		1.6 · 10 ¹⁰	70			
[33]	Ni _{0.5} Zn _{0.5} Y _{0.02} Fe _{1.98} O ₄	1100	12		3.3 · 10 ⁸	25			
[36]	Ni _{0.5} Zn _{0.5} Fe ₂ O ₄	925	3	5,1				77,5	very small
[36]	Ni _{0.5} Zn _{0.5} Bi _{0.2} Fe _{1.8} O ₄	925	3	5,9				49,2	14
[37]	Ni _{0.5} Zn _{0.5} Fe ₂ O ₄	1200	6		3.79 · 10 ³		49 @ 100kHz		
[11]	Ni _{0.5} Zn _{0.5} Fe ₂ O ₄	1200	1		2.2 · 10 ⁸				
[38]	Ni _{0.5} Zn _{0.5} Fe ₂ O ₄	1200	1	4,68			50 @ 100Hz		
[39]	Ni _{0.5} Zn _{0.5} Fe ₂ O ₄	1200	1			125			
[40]	Ni _{0.5} Zn _{0.5} Fe ₂ O ₄	1200	1			125		69	2,69
[41]	Ni _{0.5} Zn _{0.5} Fe ₂ O ₄	1000	1		1.0 · 10 ⁴				
[42]	Ni _{0.5} Zn _{0.5} Fe ₂ O ₄	1400	1			242		79	
[43, 44]	Ni _{0.5} Zn _{0.5} Fe ₂ O ₄	1150	3	4,25	8.8 · 10 ⁸		1600 @ 1kHz		

Table 2.3 (continued)

Ref #	Composition	T _{Sint} (°C)	t _{Sint} (hrs)	ρ (gr/cm ³)	ρ (Ω-cm)	μ	ε	σ _s (emu/g)	H _C (Oersted)
[43, 44]	Ni _{0.5} Zn _{0.5} Fe ₂ O ₄	1250	3	4,55	5.7 · 10 ⁷		1350 @ 1kHz		
[43, 44]	Ni _{0.5} Zn _{0.5} Fe ₂ O ₄	1350	3	4,73	2.6 · 10 ⁷		1300 @ 1kHz		
[30]	Ni _{0.49} Zn _{0.51} Fe ₂ O ₄	1000	2	4,5		150			3
[30]	Ni _{0.18} Cu _{0.31} Zn _{0.51} Fe ₂ O ₄	1000	2	5		370			0,3
[31]	(Ni _{0.3} Cu _{0.2} Zn _{0.5} O)(Fe ₂ O ₃) _{0.98}	1000	4	5,1	2.24 · 10 ¹⁰	610	50 @ 100Hz		
[45]	Ni _{0.5} Zn _{0.5} La _{0.05} Fe _{1.95} O ₄	1250	35	5,301			650 @ 400kHz		
[46]	Zn _{0.65} Ni _{0.35} Fe ₂ O ₄	1200	2					67	2,7
[47]	Zn _{0.65} Ni _{0.35} Fe ₂ O ₄				1.7 · 10 ⁶			5287 (Gauss)	1,1
[47]	Zn _{0.65} Ni _{0.35} Fe _{1.6} Mn _{0.4} O ₄				1.9 · 10 ⁶			4476 (Gauss)	1,1
[34]	Mn _{0.05} Ni _{0.45} Zn _{0.5} Fe ₂ O ₄	1200			7 · 10 ⁸ @ 1kHz		20 @ 100Hz	1978 (Gauss)	1,52

2.4.4 Additives

In general, the sintering additives are introduced into a ceramic powder batch prior to the firing process in order to modify the sintering characteristics. Such additives are inorganic in nature, and quite often they are oxides which can generate a liquid phase that facilitates sintering. In case of electronic ceramics the presence of the second phase is tolerable so long as the basic properties of the material are not harmed.

In case of NZF ceramics the use of inorganic additives has been rather limited. For example, even small amounts of SiO_2 and/or BaSO_4 were found to provoke discontinuous grain growth in the sintered ferrite [28]. CaO addition was detrimental to the magnetic properties because the Ca^{+2} cations were preferentially absorbed at grain boundary surfaces forming CaFe_3O_8 (calcium orthoferrite) as a second phase residing along grain boundaries [13, 29]. Another common additive, V_2O_5 , noted for its liquid phase forming capability in electronic ceramics was noticed to impede grain growth in NZF ceramics; the grains in the microstructure were found to be wetted by a liquid phase of V_2O_5 which blocked diffusion mechanisms essential for sintering [13].

Although fluoride compounds, like LiF or AlF_3 , have been used for achieving enhanced densification in structural ceramics like MgO or MgAl_2O_4 [48, 49], their use in the production of electronic ceramics has been scarce. For instance, the only study in which CaF_2 was used as a sintering additive was the one reported very recently by Zhang and coworkers [50] on zinc niobate ceramics for microwave applications. Their work, which was published shortly after this thesis project was initiated, showed that when CaF_2 was added in quantities not exceeding 1 weight percent (wt %), the ZnNb_2O_6 ceramics could be densified to 97 % of the theoretical density at a firing temperature as low as 1080 °C. The sintered material was single phase columbite, and its microwave characteristics were quite acceptable.

CHAPTER 3

EXPERIMENTAL PROCEDURES

3.1 General

The ferrite ceramics studied in the present thesis were produced from powders synthesized through the mixed oxide process. Samples of nickel zinc ferrite (NZF) ceramics were prepared by sintering the powder compacts in the form of toroids, tablets or discs. The effects of the material chemistry and sintering variables on microstructure development were examined by optical microscopy and by scanning electron microscope (SEM) analyses. The electrical and magnetic properties were measured by well-established characterization techniques.

3.2 Experimental Technique

3.2.1 Synthesis of the Nickel Zinc Ferrite Powder

The NZF powder used in the experiments of this thesis study was prepared by following the conventional thermal synthesis method known as “mixed oxide.” A summary of the procedure followed is given in the flow sheet shown in Figure 3.1. The basic ferrite composition of interest in this thesis was the stoichiometric compound $\text{Ni}_{0.5}\text{Zn}_{0.5}\text{Fe}_2\text{O}_4$. The raw materials used in the synthesis of this compound were NiO, ZnO, and Fe_2O_3 . When necessary, CaF_2 was incorporated as a sintering aid. All raw materials were purchased from Merck (Germany) in the form of high purity powders. A summary of the raw material characteristics are given in Table 3.1.

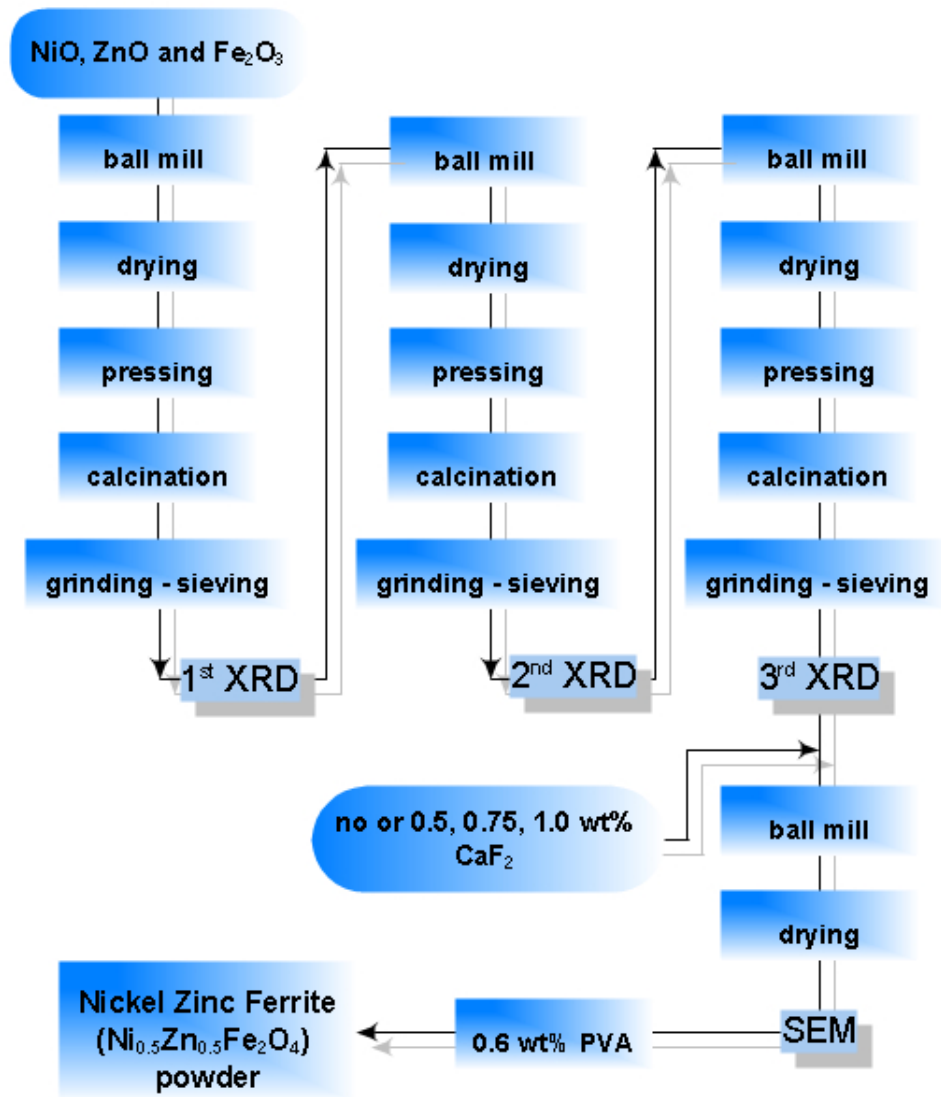


Figure 3.1 The flowchart showing the steps involved in the production of the nickel zinc ferrite powder.

Table 3.1 Characteristics of powders used in the production of ferrite powders.

Powder	Merck Catalogue Number	Impurity concentration guaranteed by the manufacturer
Ni ₂ O ₃	106723	< 0.165 wt%
ZnO	108844	< 0.0815 wt%
Fe ₂ O ₃	103924	< 0.065 wt%
CaF ₂	102842	< 0.0344 wt%

Prior to its use the as received Ni₂O₃ powder, black in color, was heated to 1030 °C in a platinum dish and kept there for 6 hours in order to convert all nickel (Ni⁺³) cations into Ni⁺² state. This process yielded green NiO powder. As preliminary treatment, the Fe₂O₃ powder was heated at 890 °C, and ZnO was heated at 1100 °C each for 6 hours. The cakes obtained from preliminary thermal treatments were powdered by milling in a mortar and pestle. These powders were stored in a desiccator.

For the synthesis of the ferrite compound, first the required proportions of NiO, ZnO and Fe₂O₃ powders were weighed in accordance with the stoichiometric molecular formula of Ni_{0.5}Zn_{0.5}Fe₂O₄. After weighing, the ingredients were intimately mixed in a hardened steel jar by ball milling for 2.5 hours. Ethanol was used as the milling fluid. Ytria stabilized zirconia balls, 8 mm in diameter, were used as the milling medium. Selection of zirconia balls instead of steel milling media mitigated the contamination due to probable abrasion of the latter.

After mixing and milling, the slurry was dried in an oven at 70 °C. The dry powder mix was compacted by pressing uniaxially in a stainless steel die under a load of 1500 kg. The pressed cake was a big tablet measuring 25 mm in diameter and 35 mm in height. The tablet was calcined in a muffle furnace in air

atmosphere until single phase NZF powder was produced. The calcination process was carried out in three successive stages.

The first step calcination was conducted at 950 °C for 3 hours. After that the soft calcined cake was ground in a porcelain mortar and pestle until all particles passed from 150 µm sieve. The x-ray diffraction (XRD) pattern of that powder, shown in Figure 3.2, revealed that substantial ferrite formation took place during the first round of calcination, but yet some NiO and Fe₂O₃ remained unreacted. This powder was ball milled for 6 hours. Then, the tablet pressed from it was calcined again at 950 °C for 3 hours. The XRD analysis, presented in Figure 3.3, showed that the product still contained some free Fe₂O₃. The milling, pressing, and calcination processes were repeated for a third time so that a single phase NZF could be obtained as seen from the XRD pattern in Figure 3.4. The last calcination was also done at 950 °C for a duration of 3 hours.

The fully calcined tablet was crushed and ground in a porcelain mortar and pestle and then it was ball milled for 12 hours in order to obtain the fine ferrite powder used in ceramic production. One observation made later in the sintering stage is worthy to mention here; the procedures followed in powder preparation had considerable influence on its sintering tendency. For example, variations in the cooling rate during the calcination process would effect the relative sintered density considerably. Lower cooling rates yielded powders which could densify better, the reason for this could be the higher oxygen take-up during cooling.

When CaF₂ would be introduced as sintering aid, this was done prior to the last ball milling step. The required proportion (0.50 wt %, 0.75 wt %, or 1.00 wt % CaF₂ by weight of the ferrite powder) was blended with the NZF powder produced until that stage and then the mixture was ball milled for 12 hours in order to obtain a uniform dispersion of CaF₂.

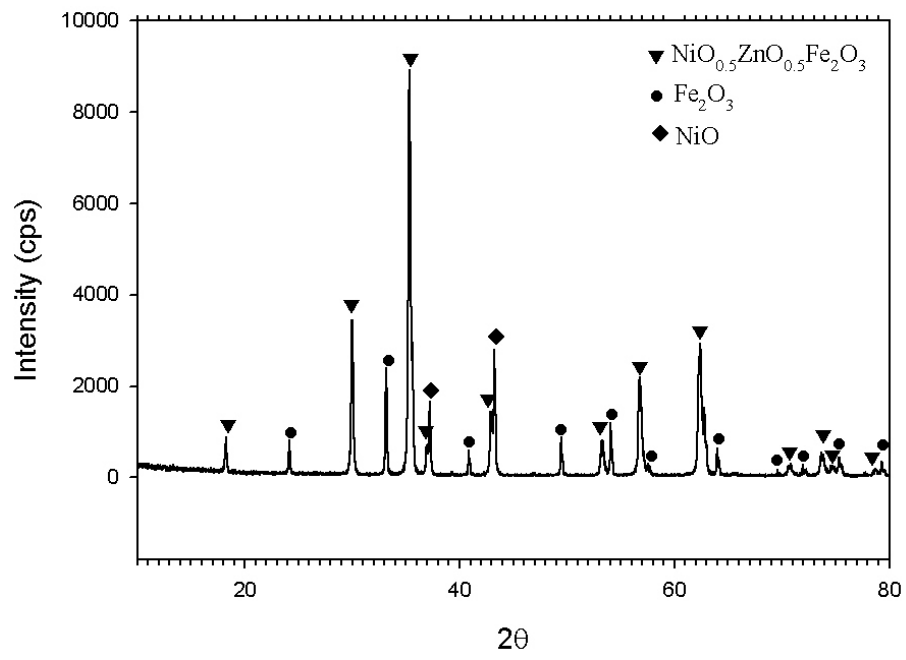


Figure 3.2 XRD of the NZF powder after the first calcination.

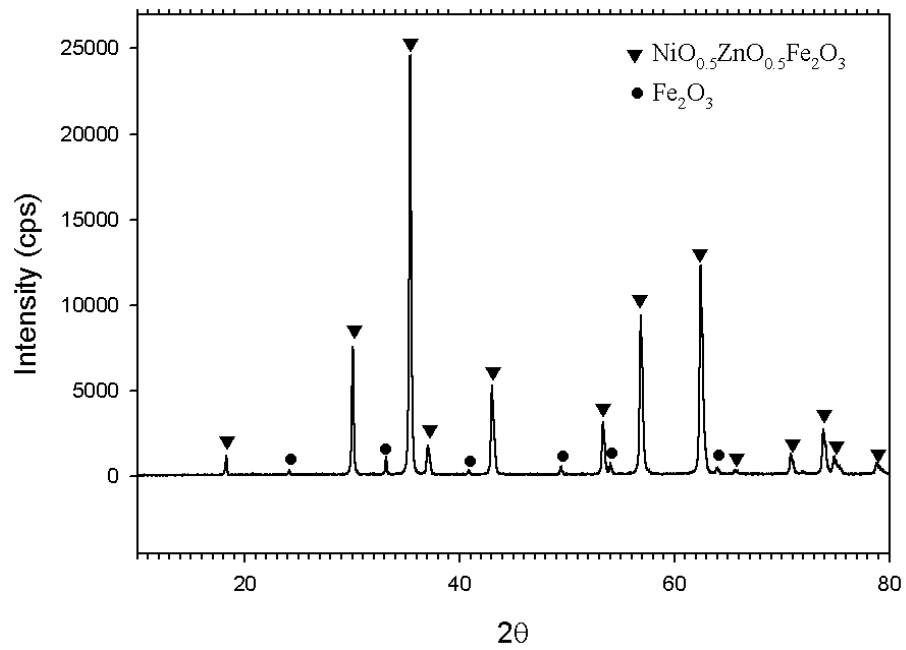


Figure 3.3 XRD of the NZF powder after the second calcination.

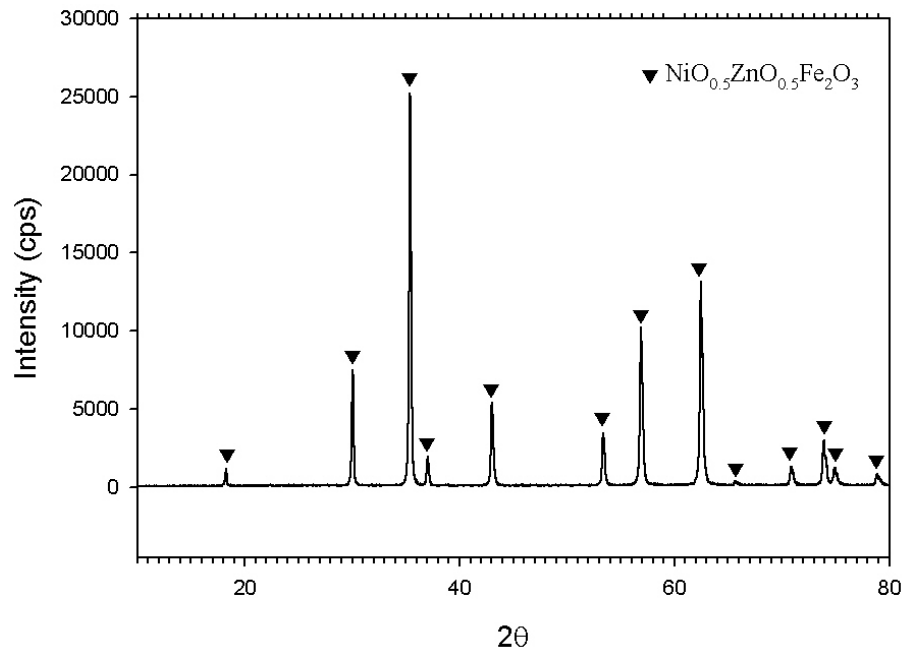


Figure 3.4 XRD of the powder produced after the third calcination showing single phase NZF.

Examination of the ball milled ferrite powder through SEM has led to the decision that the state of comminution of powder was good enough for sintering studies. As seen in the SEM micrograph given in Figure 3.5, the particle size was typically below 1 micrometer (micron, μm). Unfortunately some agglomerates remained in the powder despite extensive milling.

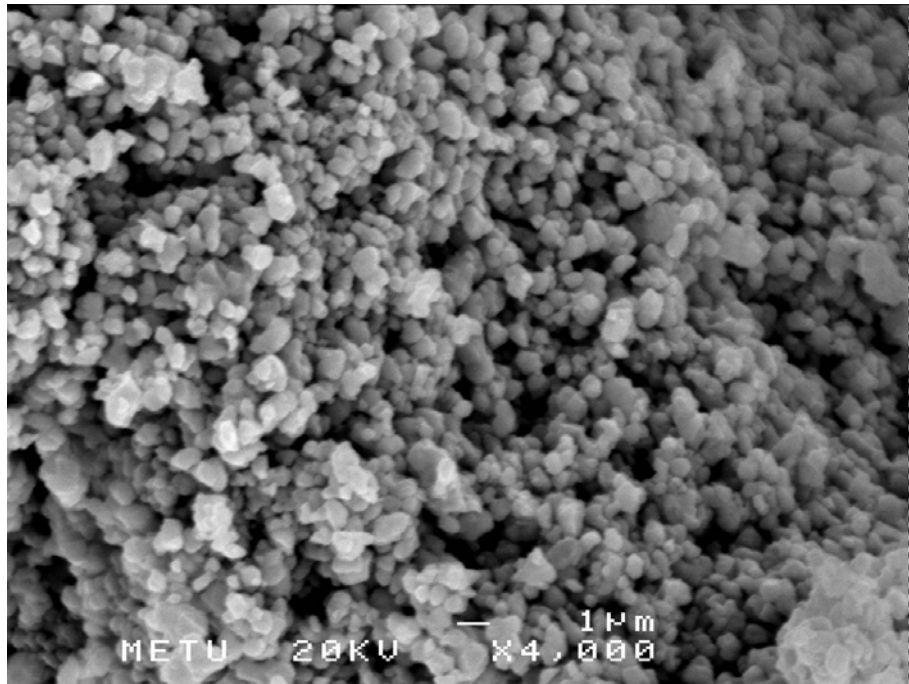


Figure 3.5 A SEM photo of the NZF powder produced by thermal synthesis technique used in this study.

3.2.2 Preparation of Ceramic Samples

The ferrite powder obtained by the thermal synthesis process as described in the previous section was used for the production of magnetic ceramics studied in the present thesis study. Samples in the form of discs and toroid cores were prepared by uniaxial pressing of the powder in hardened steel dies of appropriate design.

Polyvinyl alcohol, PVA, with an amount of 0.6 wt % of the ferrite powder was used as binder. An aqueous stock solution of PVA containing 25 grams of PVA per liter was used for that purpose. The pressing pressure was 100 MPa. After pressing, the discs were 13 mm in diameter and 3.6 mm in height. The outer diameter, inner diameter and height of the pressed toroid cores were 20.4 mm, 8.5 mm and 5.9 mm, respectively.

The pressed samples were sintered in a muffle furnace heated by silicon carbide Globar elements. The furnace was operated and controlled by a Honeycomb 2000 PID unit which allowed executing programmable sintering schedules. The temperatures inside the muffle furnace could be controlled within ± 2 °C of the set values. The accuracy in temperature was checked by an additional standardized Pt-Pt10%Rh thermocouple.

Two disc pellets and one toroid having the same chemical composition were sintered simultaneously at a time. These samples were placed on sintered NZF pedestals which served as saggars. The heating rate was 4 °C/min up to 800 °C beyond this point it was decreased to 2 °C/min until peak temperature was reached. For all samples, the sintering process included a soaking period at 1200 °C. The soaking duration was variable; it was chosen as 2, 6, 12 or 18 hours. Upon termination of the soak the ceramics were allowed to cool down to room temperature at a rate of 1 °C/min. This low rate was adopted in order to avoid generation of thermal stresses during cooling which could lead to the straining and eventual degradation in physical properties of sintered ceramics. The sintering schedule consisting of these basic steps is shown schematically in Figure 3.6.

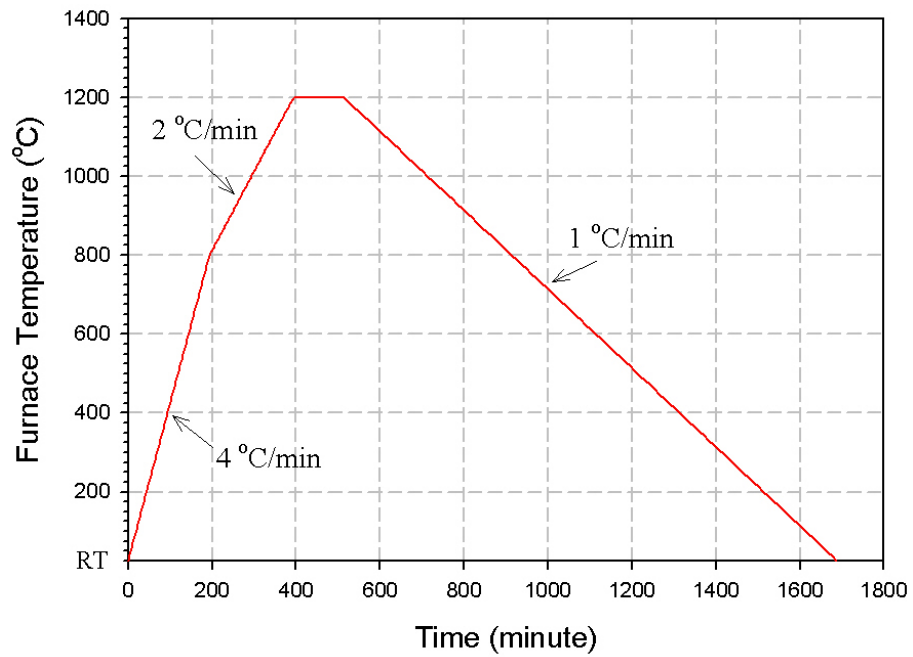


Figure 3.6 The time - temperature program used during sintering experiments of this study.

One of the sintered ferrite discs was used for the evaluation of electrical properties of the ceramic. The second disc was utilized to examine the microstructural features. The toroidal core was used for determination of magnetic properties. A group of sintered ceramics is displayed in Figure 3.7.

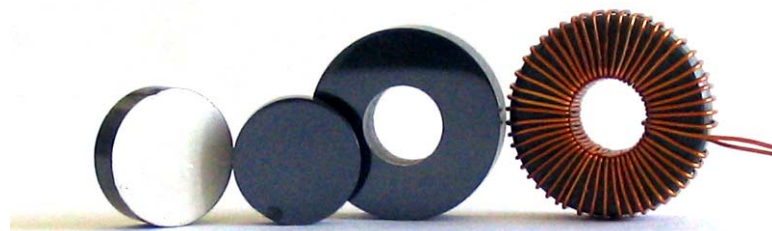


Figure 3.7 NZF samples prepared for experimental studies in this thesis.

3.2.3 Characterization

3.2.3.1 Density Measurements

Densities of sintered ceramics were determined by using the Archimedes' buoyancy principle. Xylene (Merck, extra pure >99.9%) was the immersion medium. Weight measurements were done with an electronic balance (Sartorius CP224S-0CE, Germany) equipped with a density determination kit. The overall accuracy in the density measurements was estimated as $\pm 0.0001 \text{ gr/cm}^3$, hence the percentage error in the measured density was $\pm 0.01\%$.

As-sintered samples were weighed dry, to obtain W_{dry} , and then immersed in xylene until the sample was fully saturated. The minimum immersion period was 48 hours. At this stage the saturated weight, W_{susp} , of the sample was recorded while it was suspended in xylene. Afterwards, the sample was removed from the xylene bath, it was wiped quickly to remove the excess liquid over the surface and then it was weighed again, but this time in air. That last measured weight was noted as the saturated weight, W_{sat} , of the sample. In order to keep away from hazardous emissions, work with xylene was conducted under a ventilated hood.

The bulk density of the sample was calculated with the formula:

$$\rho_{\text{bulk}} = \frac{W_{\text{dry}} \cdot \rho_{\text{xyle}}}{W_{\text{sat}} - W_{\text{susp}}} \quad (\text{gr/cm}^3), \quad (3.1)$$

where:

ρ_{bulk} : bulk density of the sample in gr/cm^3 ,

W_{dry} : dry weight of the sample in grams,

ρ_{xyle} : density of the xylene = 0.86 gr/cm^3 ,

W_{sat} : saturated weight of the sample in grams,

W_{susp} : suspended weight of the sample in grams.

3.2.3.2 Microstructural Characterization

3.2.3.2.1 Grain Size and Grain Size Distribution

Studies on microstructure of ferrite ceramics were conducted on polished and etched sections of the sintered disc pellets. The ceramic selected for this purpose was prepared by conventional metallographic methods which involved grinding the surface on graded emery paper and then polishing it with diamond paste (Struers, Denmark, DP-Paste, P type) with 1 μ m particle size. The polished pellet surface was etched in a boiling aqueous solution of HNO₃ – H₂C₂O₄ – HCl – HClO₄ – H₂SO₄ for 30 minutes. The volumetric proportions of the constituents in the etchant were H₂O: HNO₃: H₂C₂O₄: HCl: HClO₄: H₂SO₄ = 16: 16: 12: 8: 8:1. The etchant for the ceramics containing some amount of CaF₂ did not include H₂SO₄.

The grain size determination in sintered ceramics was done by processing the optical micrographs taken from the plane of polish of each sample. An image analyzing software (The Clemex Vision Professional Edition Image Analysis System, Version 3.5.020) was used to collect and process the grain size data. A typical optical micrograph used for this study is illustrated in Figure 3.8.

The calculations related to grain size distribution were carried out by following the methodology proposed by Oel [51, 52]. The scrappy grains at the edge of each micrograph were excluded from calculations. Grains were assumed to be circular in the plane of polish. Cross sectional area of each grain was calculated by the help of the Clemex image analysis system. A circular diameter for each grain, to be used as raw data, was assigned from the calculated cross sectional area. The plane of polish did not represent the maximum cross section of each grain. Therefore, the diameter data taken from plane of polish had to be corrected by reference to the geometry sketched in Figure 3.9.

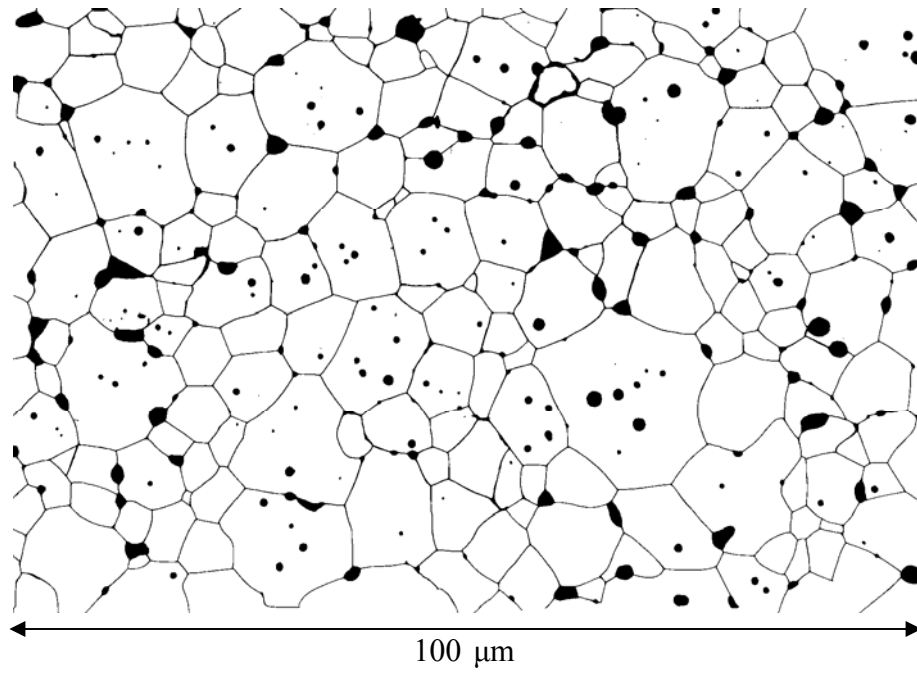


Figure 3.8 An optical micrograph of a nickel zinc ferrite ceramic used for grain size determination.

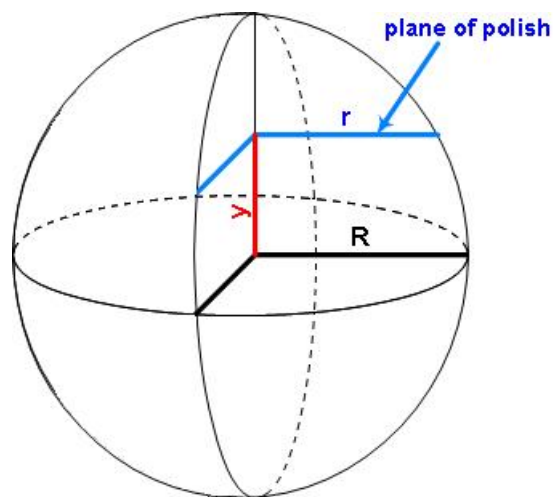


Figure 3.9 The circle with radius r created due to sectioning of a sphere with radius R . The plane of polish includes circle with radius r .

The relation between the distribution function of raw data and the corrected distribution function was given by the Abel integral equation [51, 52]:

$$q(r) = \int_r^{R_{\max}} p(R) \frac{r}{\sqrt{R^2 - r^2}} dR, \quad (3.2)$$

where: $q(r)$: the distribution function for circles of radius r ,
 $p(R)$: the distribution function for spheres of radius R .

The correction of raw data was executed by the solution of the Abel integral equation in summation form:

$$Q(r_n) = \sum_{i=n+1}^m P(R_i) \frac{r_n}{\sqrt{R_i^2 - r_n^2}} \quad R_i \equiv r_i, \quad (3.3)$$

where: $Q(r_n)$: was the number of circles in a class with radius r_n ,
 $P(R_i)$: was the number of spheres in a class with radius R_i ,
 m : was the number of class intervals.

A typical histogram obtained for the raw data gained from image analyzing program is shown in Figure 3.10.

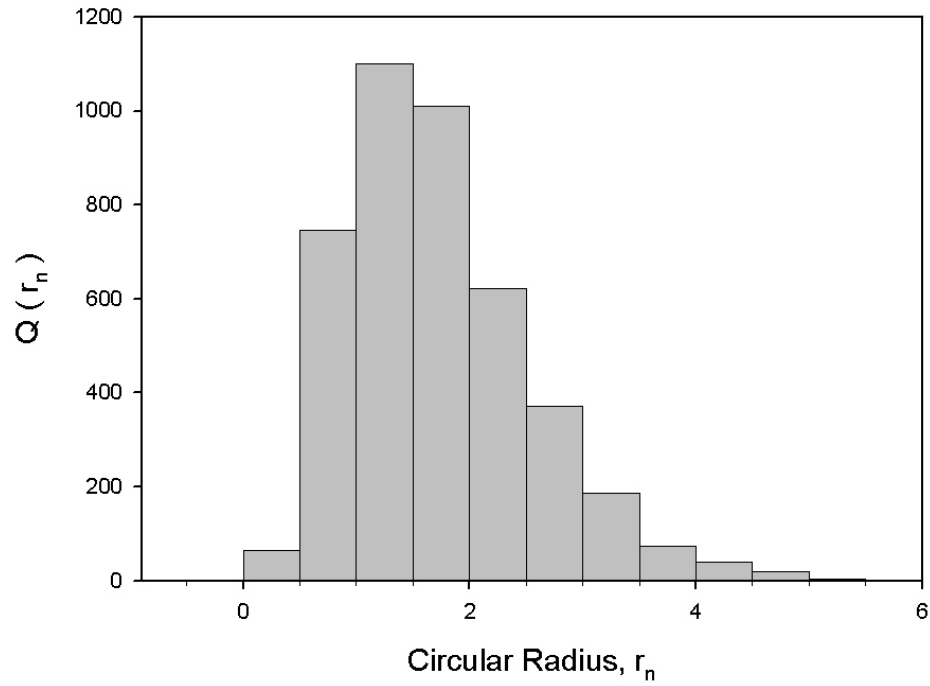


Figure 3.10 A typical histogram obtained from plane of polish of the ferrite ceramic produced in this study.

Introducing the abbreviations $Q_n = Q(r_n)$ and $P_n = P(R_n)$, and beginning with the largest radius, the first equation was found to be:

$$Q_{m-1} = P_m \frac{r_{m-1}}{\sqrt{R_m^2 - r_{m-1}^2}}, \quad (3.4)$$

from which the P_m was calculated. The second term, P_{m-1} of distribution function was calculated from:

$$Q_{m-2} = P_{m-1} \frac{r_{m-2}}{\sqrt{R_{m-1}^2 - r_{m-2}^2}} + P_m \frac{r_{m-2}}{\sqrt{R_m^2 - r_{m-2}^2}}. \quad (3.5)$$

Likewise, the third term, P_{m-2} , of distribution function of spheres was calculated from:

$$Q_{m-3} = P_{m-2} \frac{r_{m-3}}{\sqrt{R_{m-2}^2 - r_{m-3}^2}} + P_{m-1} \frac{r_{m-3}}{\sqrt{R_{m-1}^2 - r_{m-3}^2}} + P_m \frac{r_{m-3}}{\sqrt{R_m^2 - r_{m-3}^2}}, \quad (3.6)$$

and so on. The values of P_n obtained from this treatment yielded the distribution curve shown in Figure 3.11.

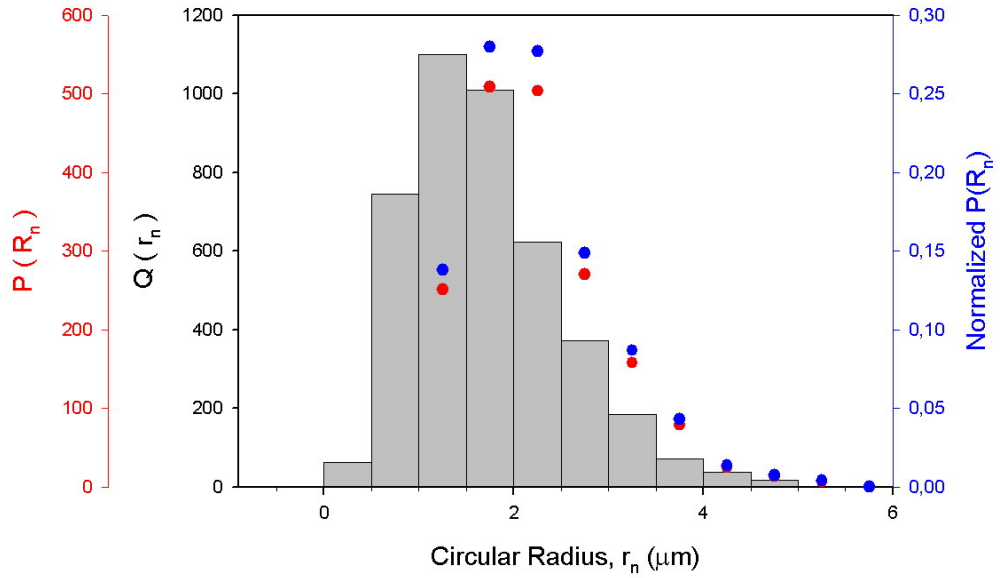


Figure 3.11 The coefficients of the distribution function for spheres, P_n , with observed Q_n values.

The calculated P_n values were normalized and then they were fitted to a log-normal distribution with the following familiar expression:

$$f = a \cdot \exp \left(-\frac{1}{2} \cdot \left(\frac{\ln \left(\frac{x}{x_0} \right)}{b} \right)^2 \right), \quad (3.7)$$

where: a: constant,
 x_0 : mean value of the log-normal distribution,
 b: standard deviation of the log normal distribution.

3.2.3.3 X-Ray Diffraction

The phase analyses on sintered NZF ceramics were supplemented by powder X-ray diffraction (XRD) studies. A fragment from sintered discs was crushed and ground in a mortar and pestle to prepare the powder used in X-ray diffraction analysis. A computerized Rigaku DMAX-B unit was employed for collecting 2θ values of diffraction and the intensity of the diffraction peaks. Phase identification was executed by an automated built in software of the XRD unit. The details of the parameters involved in XRD studies are summarized in Table 3.2.

Table 3.2 The parameters of the X-ray diffraction analysis.

Radiation type	Cu
λ value used	1.542 Å, K_{α}
X-ray operation	40 kV, 40 mA
λ discrim	Diffracted beam, graphite mono
λ detector	Scintillation
Temperature	22±2 °C
Range of 2θ	10° to 80°
Step size	0.02° 2θ
Count time	1.2 sec

3.2.3.4 SEM Investigations

The microstructures of sintered ceramics were examined via scanning electron microscope, SEM. This was carried out on polished and etched surfaces as well as on freshly broken fragments. A JEOL JSM6400 Scanning Electron Microscope, equipped with NORAN X-ray Microanalysis System and Semafore Digitizer was used for this purpose. Prior to SEM investigation all surfaces were coated with a 250 Å thick layer of a Au-Pd alloy.

The EDS attachment on the SEM unit facilitated to make records of the spectra and to obtain in-situ chemical analysis of the samples. The chemical nature of grain interior and grain boundary regions were at the focus of SEM study.

3.2.3.5 Electrical Characterization

3.2.3.5.1 Electrical Resistivity Measurements

The measurements on electrical resistivity were performed on one of the sintered discs. The flat faces of disc were lapped, a record of the thickness and the diameter was done, and then the parallel faces were electroded with fired-on silver paste. Lapping of the opposite faces of the disc was done with SiC abrasive papers down to grade 1200. Silver paste (Code C71208R3, Gwent Electronic Materials Ltd., UK) was applied to the surfaces to provide electrical contact. Silver paste was fired at 600 °C for 15 minutes in a tube furnace in air atmosphere. The heating and cooling rates were 1 °C/min.

DC electrical resistivity measurements were conducted by the two point technique under a potential difference of 1 V. A HP4140B picoammeter unit was employed as a constant DC voltage supply and also to measure the current. All measurements were done at room temperature with the resistivity set-up shown in Figure 3.12.

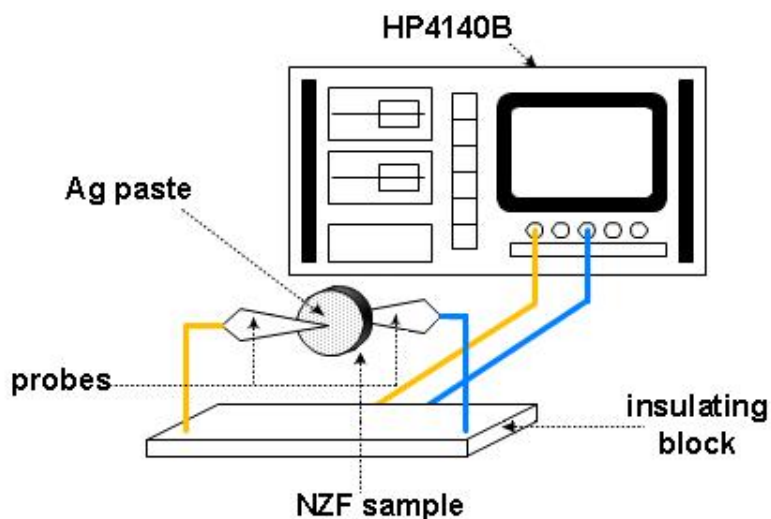


Figure 3.12 Schematic representation of the set up used for DC electrical resistivity measurements.

3.2.3.5.2 Dielectric Constant and Dielectric Loss Factor Measurements

The disc shaped ceramics prepared for DC electrical resistivity measurements were also utilized in the investigation of the dielectric properties. Dielectric properties of nickel zinc ferrite ceramics were determined with the help of a computerized HP4194A Impedance/Gain Phase Analyzer in the 100 Hz – 40 MHz frequency range under a potential difference of 1 V. Experimental set-up used for this purpose is shown schematically in Figure 3.13. The capacitance and the dielectric loss tangent values of the ceramics could be determined simultaneously. The dielectric constants of ceramics were determined from experimentally obtained capacitance values. The data were taken at room temperature.

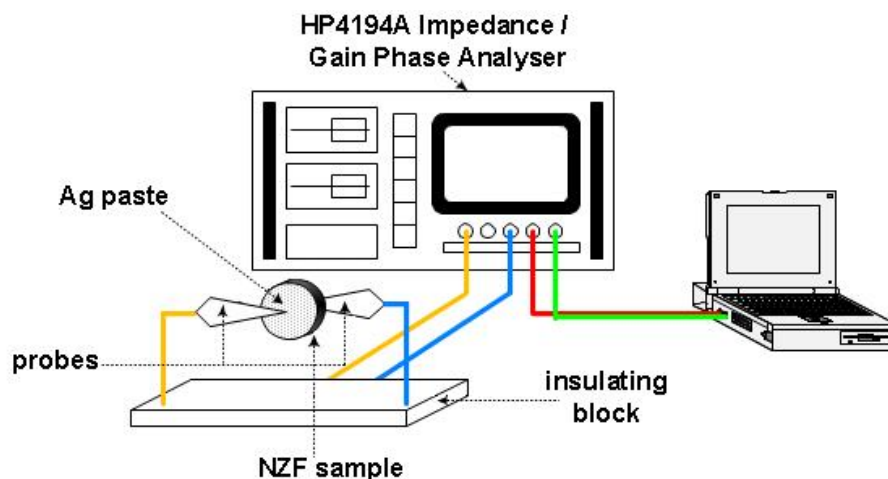


Figure 3.13 Schematic representation of the set-up used for dielectric property investigations.

3.2.3.6 Magnetic Characterization

3.2.3.6.1 Initial Magnetic Permeability and Magnetic Loss Factor

Magnetic characterization of nickel zinc ferrite ceramics were done on toroidal samples. The flat surfaces of the ferrite cores used for this purpose were first lapped with SiC abrasive, and then the sharp edges were chamfered by grinding with emery paper. The dimensions of the cores including the outer diameter, the inner diameter and the thickness were recorded. After that the toroids were tightly wound with about 60 turns of enameled copper wire 0.35 mm in diameter.

The experimental set-up used in magnetic permeability determination is shown in Figure 3.14. A computerized HP4194A Impedance/Gain Phase Analyzer was the basic testing unit used to measure the inductance and magnetic loss factor. The leads of the toroids were connected directly to the terminals of the HP4194A Impedance/Gain Phase Analyzer. The inductance and loss factor measurements were performed in the 100 Hz – 10 MHz frequency range under low excitation voltages. The excitation voltages were selected as 0.01 V, 0.02 V and 0.03 V so

that the value of initial magnetic permeability was determined in the reversible magnetization region.

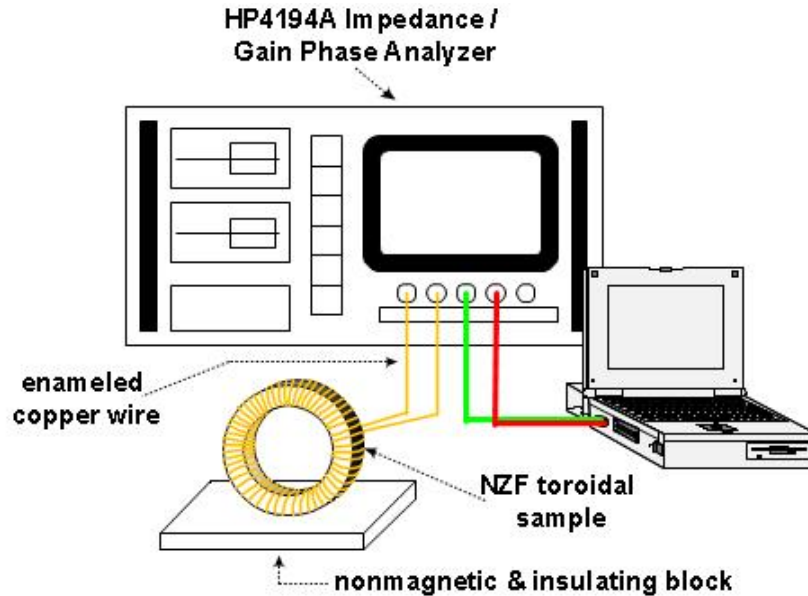


Figure 3.14 Demonstration of the setup used for inductance and loss factor measurements of toroids.

3.2.3.6.2 Magnetic Hysteresis

In order to study the response of the sintered ferrites to external magnetic fields the toroids used in magnetic permeability measurements were modified by putting a secondary winding on top of the primary one. The secondary coil was formed by winding it from 0.1 mm diameter enameled copper wire. For taking the data necessary to examine hysteresis behavior, a home-built hysteresis meter was constructed, which involved a computerized HP 54645 oscilloscope associated with an Agilent 33120A Arbitrary Waveform Generator. The set-up utilized for hysteresis studies is shown in Figure 3.15.

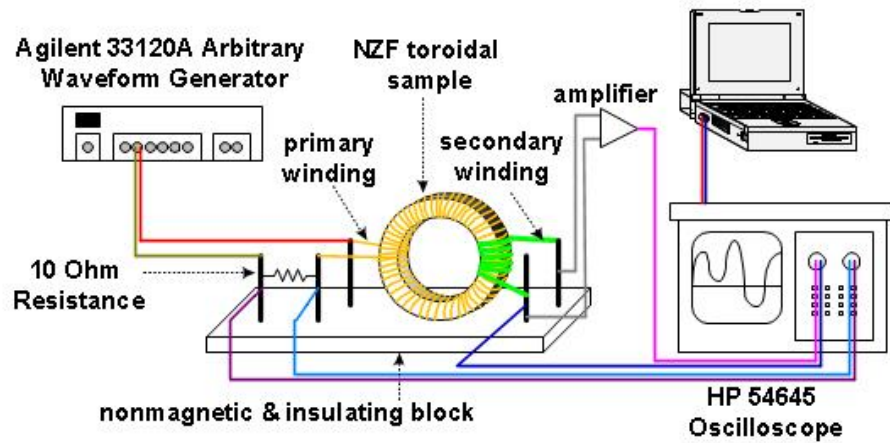


Figure 3.15 Schematic representation of the setup constructed for magnetic hysteresis measurements.

A hysteresis measurement consisted of measuring the voltage induced in the secondary coil of the toroid in response to an ac voltage which was applied to the primary one for obtaining the magnetic field. The frequency of the applied sinusoidal wave was kept constant at 1 kHz. Input and output voltages were recorded continuously. The primary voltage was used for calculating the magnetic field applied to the toroid, while the voltage induced in the secondary was used for calculating magnetization of the ferrite.

Following expression was used for converting the primary voltage into applied magnetic field strength [53]:

$$H = \frac{0.4 \cdot \pi \cdot \sqrt{2} \cdot N_1 \cdot E_H}{l \cdot R}, \quad (3.8)$$

where:

- H : strength of magnetic field applied on the toroid, Oersted (Oe),
- N_1 : number of primary turns,
- E_H : excitation voltage, V,
- l : mean geometric path length, cm,
- R : resistance, (10 Ω was connected to the set-up).

The mean geometric path length, l , required in the evaluation of H was obtained from the formula:

$$l = \frac{\pi \cdot (D_o - D_i)}{2}, \quad (3.9)$$

where: D_o : outer diameter of toroid core, cm,
 D_i : inner diameter of toroid core, cm.

The magnetization of the toroid was calculated from the expression [53]:

$$B = \frac{10^8 \cdot E_B}{\pi \cdot \sqrt{2} \cdot f \cdot N_2 \cdot \alpha \cdot A}, \quad (3.10)$$

where: B : magnetization, Gauss,
 E_B : voltage measured across secondary winding, V,
 f : cyclic frequency, Hz,
 N_2 : number of secondary turns,
 α : amplification coefficient = 3.3,
 A : solid cross sectional area of the toroid core, cm^2 .

The term A_s was obtained from the formula:

$$A = \frac{t \cdot (D_o - D_i)}{2}, \quad (3.11)$$

where: t : thickness of the toroid core, cm,
 D_o : outer diameter of the toroid core, cm,
 D_i : inner diameter of the toroid core, cm.

During the hysteresis study, the oscilloscope HP 54645 in the set-up produced a continuous display of the hysteresis curve of the ferrite. The computer in the system received the information on E_H and E_B and converted them into the values of H and B , respectively, through the expressions given in Equation (3.8) and Equation (3.10). These data could be used to re-generate the hysteresis curve when needed.

CHAPTER 4

EXPERIMENTAL DATA AND RESULTS

4.1 General

The data obtained during the experiments were related to the microstructural features of sintered ferrites and their relationship to the measured magnetic and electrical properties. The details concerning experimental data and the results obtained from their treatment are presented in the following sections.

4.2 X-Ray Diffraction Studies on Sintered Ferrites

A typical XRD pattern of the ferrite powder prepared to use in experiments of this thesis work was already presented in Chapter 2. Examples of the XRD data related to the ferrite ceramics sintered in the presence of CaF_2 are shown in the diffractograms reproduced in Figure 4.1. The material in all diffraction patterns was identified as phase-pure NZF in concordance with the JCPDS-ICDD 2002 PDF-2 data base number 52-0278. There was no second phase formation that could be attributed to the presence of CaF_2 . This led to the conclusion that CaF_2 was dissolved completely in the spinel lattice.

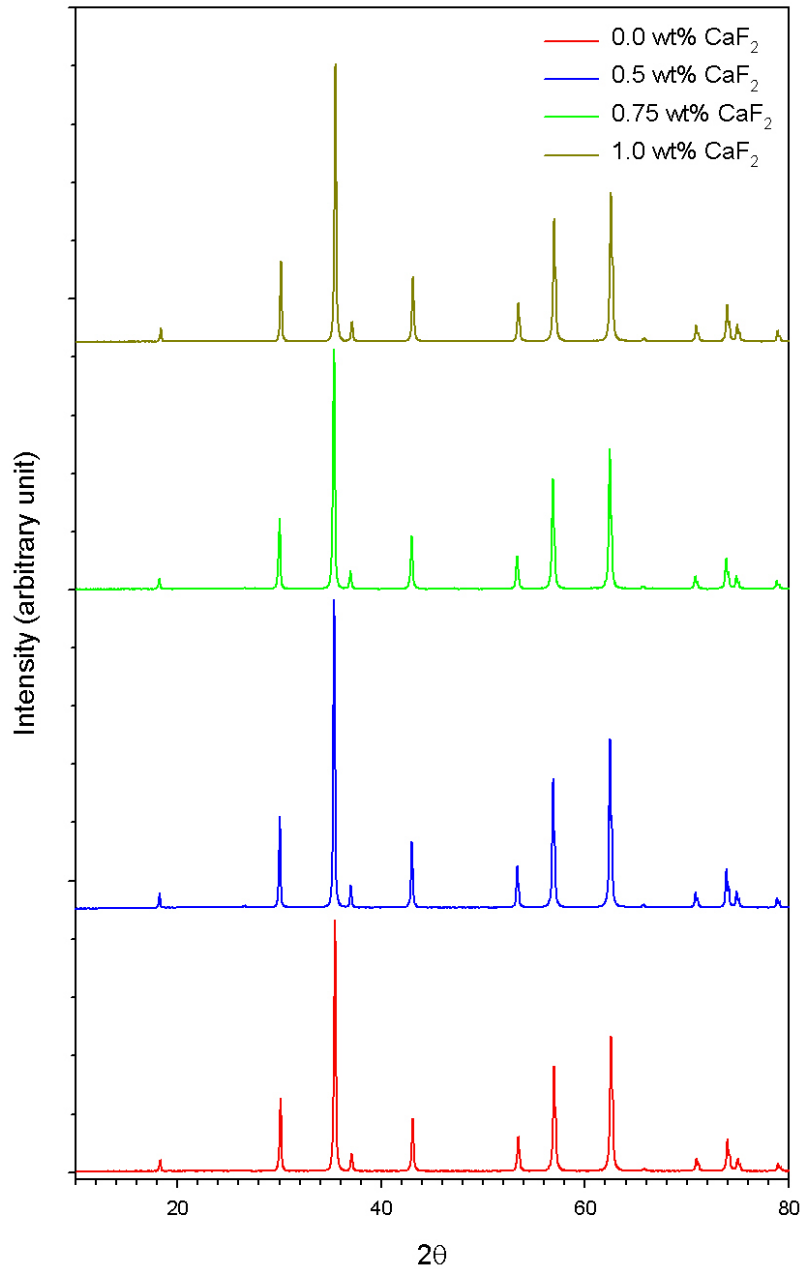


Figure 4.1 XRD patterns of nickel-zinc ferrite ceramics containing various amounts of CaF₂. The samples were soaked at 1200 °C for 2 hours.

The diffractograms seen in Figure 4.1 were taken from samples sintered at 1200 °C for 2 hours. The effect of prolonged sintering on phase constitution was examined by performing XRD studies on the NZF ceramics that contained 1.0 wt% CaF₂. These samples were sintered for durations extended up to 18 hours.

The XRD patterns displayed in Figure 4.2 revealed that no change in the single-phase constitution of the NZF would come out during extended sintering.

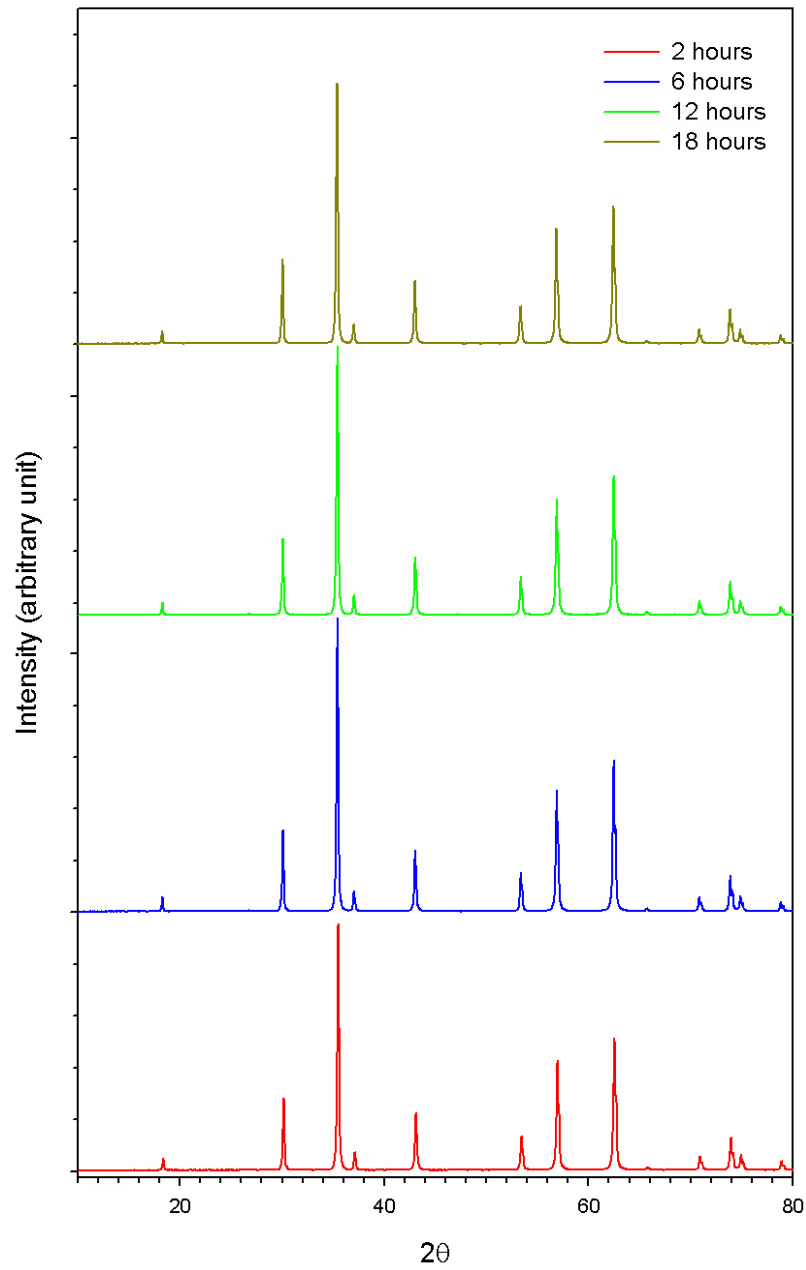


Figure 4.2 XRD patterns for the NZF ceramics soaked for durations up to 18 hours at 1200 °C. The ceramics contained 1.0 wt% CaF₂.

It was observed that CaF₂ additions did not cause detectable shift in the position of the major XRD peak of the ferrite. By using silicon as an external standard, the angle corresponding to the major diffraction plane (311) was determined as $2\theta = 35.48^\circ$. This data was processed to calculate the lattice size of the ferrite as $a = 8.3899 \text{ \AA}$. For the calculation of the X-ray density, $\rho_{\text{x-ray}}$, of the NZF ceramics produced in the present study the value for “a” was inserted into the following expression [20]:

$$\rho_{\text{x-ray}} = \frac{8 \cdot M}{N_A \cdot a^3}, \quad (4.1)$$

The terms M and N_A in Equation (4.1) are the molecular mass of the ferrite compound and the Avogadro’s number, respectively. Thus, the X-ray density of the ferrites was calculated as 5.347 gr/cm³. In the treatment of densification data, this value was used as the theoretical density of the NZF ceramic.

4.3 Data and Results on Sintered Density

Density measurements were conducted on the sintered ferrite tablets according to the Archimedes’ principle as described in Section 3.2.3.1. The data obtained in these measurements are given in Table 4.1. These data correspond to density values attained at the peak sintering temperature 1200 °C. The data cover pure ferrites as well as those which contained different levels of CaF₂ addition. The left-hand-side column of the table represents the soak durations at the peak firing temperature.

Table 4.1 The bulk density data for the NZF ceramics produced in the present study.

Soaking Time (hours)	Bulk Density (gr/cm ³)			
	wt% CaF ₂ addition			
	0.0	0.5	0.75	1.0
2	4.915	5.016	5.006	5.013
6	5.045	5.083	5.073	5.065
12	5.095	5.124	5.104	5.100
18	5.124	5.149	5.124	5.120

The data given in the above table was converted into “degree of densification” by calculations based on the following expression:

$$\rho_{\%th} = \frac{\rho_{bulk}}{\rho_{x-ray}} \cdot 100, \quad (4.2)$$

where:

- $\rho_{\%th}$: bulk density of the ceramic with reference to the theoretical density,
- ρ_{bulk} : the bulk density of the sample,
- ρ_{x-ray} : the X-ray density of the ferrite, 5.347 gr/cm³.

Table 4.2 The extent of densification in the NZF ceramics of the present work, expressed as percentage of the theoretical density of the ferrite.

Soaking Time (hours)	% of Theoretical Density			
	wt% CaF ₂ addition			
	0.0	0.5	0.75	1.0
2	91.93	93.81	93.63	93.75
6	94.36	95.07	94.87	94.73
12	95.29	95.82	95.46	95.38
18	95.83	96.29	95.83	95.76

The values on the densification of the NZF ceramics, presented in Table 4.2, are displayed graphically by the densification curves as shown in Figure 4.3. The horizontal axis of the diagram represents the durations of soak during sintering at 1200 °C. The NZF ceramic which contained no CaF₂ displayed the densification behavior shown by the dashed red curve; the density levels in the pure NZF ceramic remained always inferior to those which contained CaF₂ as the sintering aid. The pure NZF ceramic could be densified to a level of almost 96 percent of the theoretical density by a prolonged sintering which lasted for 18 hours.

CaF₂ additions caused a great modification in the sintering tendency of the NZF ceramics particularly during the early stages of firing. The green density of all ferrite compacts after pressing in the die was around 58 % of the theoretical density. During the first 60 minutes of soak period the densification rate in the pure NZF ceramic was about 0.028 gr.cm⁻³.min⁻¹. With CaF₂ additions the rate was raised to 0.031 gr.cm⁻³.min⁻¹ corresponding to a boost by about 11 percent.

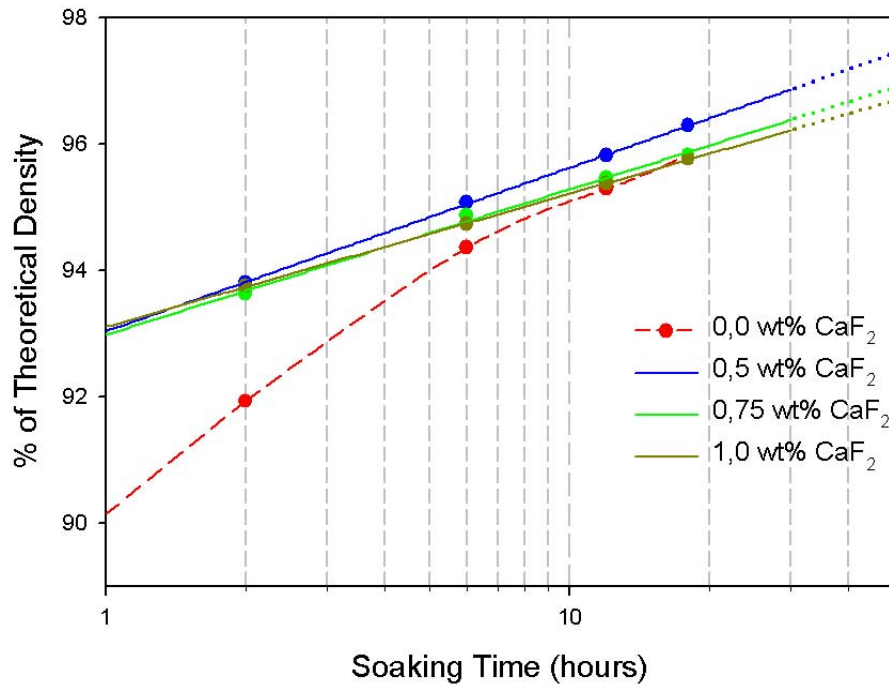


Figure 4.3 Variation in the degree of densification of the ferrite ceramics containing different amounts of CaF₂ with soak duration.

Small amounts of CaF₂ additions beyond 0.5 wt% did not produce any benefit in the densification process as shown in Figure 4.3. In fact, the sintered density tended to decline when the amount of CaF₂ exceeded 0.5 wt%. The reason for this was attributed to the pore-grain boundary separation which will be taken up in the section on microstructures.

In the NZF ceramics containing CaF₂, the existence of a linear relationship between densification and the soak duration was apparent as seen in Figure 4.3. The data obtained for the NZF ceramics containing different amounts of CaF₂ could be fitted with a linear equation as given in Table 4.3. It should be noted that, in these equations the time term was logarithmic and the unit for time was taken as “hour”.

Table 4.3 Time dependence of densification (fitted equations).

wt% CaF₂ addition	Densification Equation
0.50	$\rho = 0.9304 + 11.25 \times 10^{-3} \cdot \ln t$
0.75	$\rho = 0.9298 + 9.993 \times 10^{-3} \cdot \ln t$
1.00	$\rho = 0.9311 + 9.146 \times 10^{-3} \cdot \ln t$

4.4 Microstructural Features by SEM Analyses

SEM investigations conducted mainly on freshly fractured surfaces gave information with respect to grain morphology and bonding characteristics. The polished and etched sections were examined as well to obtain information on chemical compositions of the grains and grain boundaries.

SEM photograph of CaF₂-free NZF sample shown in Figure 4.4 revealed that the fracture occurred mainly along grain boundaries. The reason of such a fracture surface formation was partially development of intergranular contacts due to short sintering duration. Grain growth was kept at minimum. The average grain size was estimated as 1 μm which was slightly larger than the average particle size of the powder. The grain edges were sharp and the three dimensional structure of grains resembled octahedral (square bipyramidal) geometry consistent with the spinel structure.

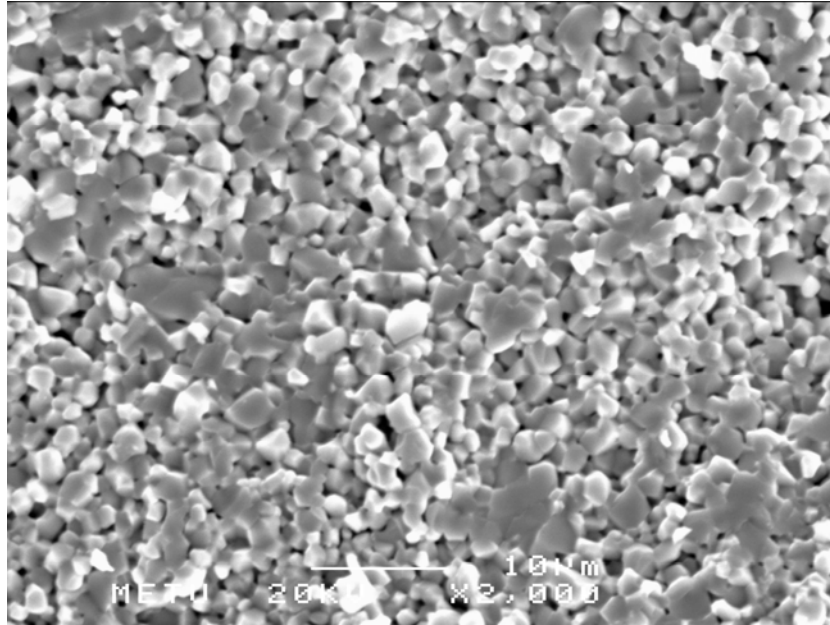


Figure 4.4 SEM image obtained from fracture surface of CaF₂-free NZF ceramic. The sample was soaked at 1200 °C for 2 hours.

An addition of 0.5 wt% CaF₂ into the NZF ceramic containing no CaF₂ activated bridging between grains. The grain growth was evident as seen in Figure 4.5. Fracture occurred partly in intergranular behavior. It was deduced that the grain - grain contact strength was higher compared to the NZF sample containing no CaF₂. The edges of grains were still sharp and the octahedral resemblance of grain structure was preserved. SEM micrograph of the polished and etched surface, shown in Figure 4.6, revealed that the average grain size was about 3 μm. Furthermore, the microstructure was homogeneous in terms of grain size. It could clearly be seen that pores were located along grain boundaries, indicating that if the soaking duration would be extended beyond 2 hours the densification could be effectively furthered.

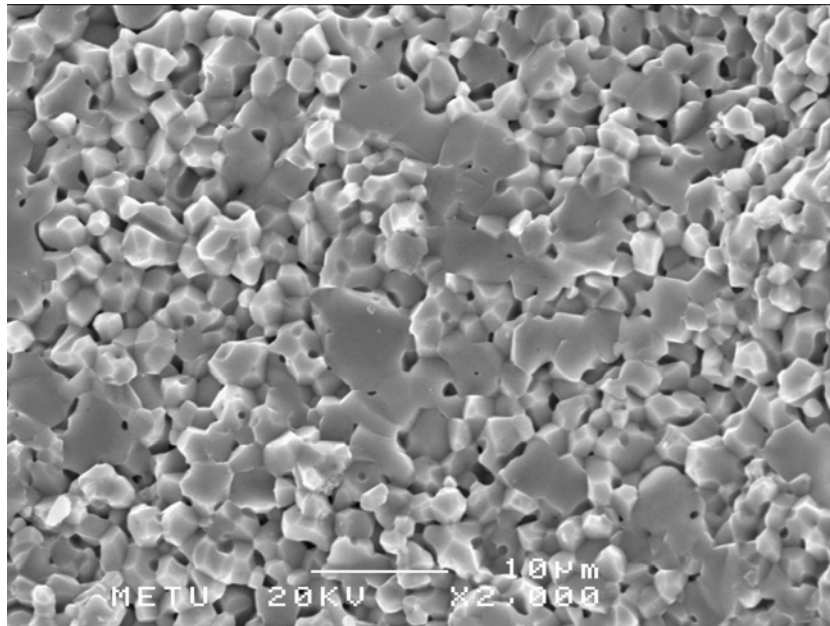


Figure 4.5 SEM fractograph of the NZF ceramic containing 0.5 wt% CaF₂. The ceramic was soaked for 2 hours at 1200 °C.

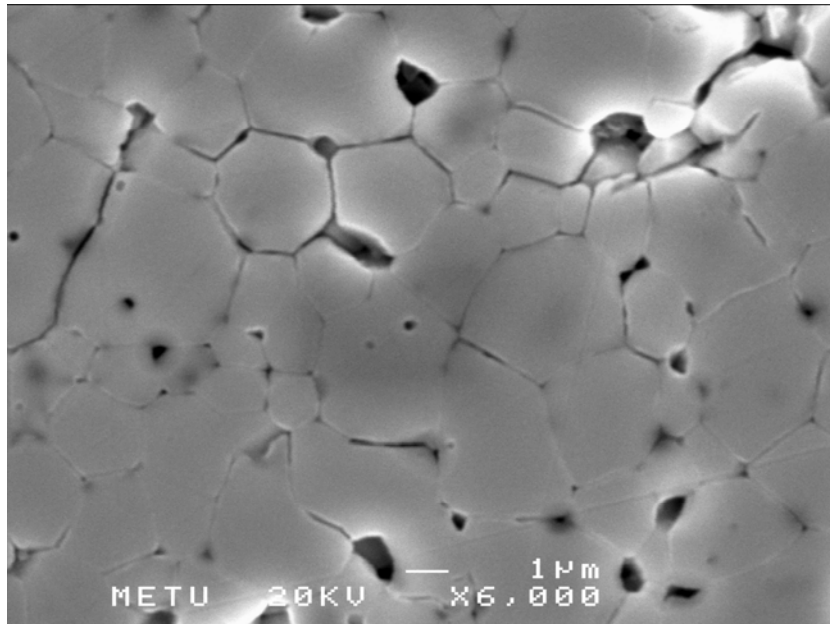


Figure 4.6 SEM micrograph of the NZF ceramic containing 0.5 wt% CaF₂. The sample was soaked for 2 hours at 1200 °C and etched.

The fracture shifted towards an intragranular mode when the CaF_2 content was increased to 0.75 wt%, as seen in Figure 4.7. This indicated that 2 hours soaking was sufficient to establish intergranular contacts. The ceramic attained adequate strength so that fracture could occur through the grains. SEM micrograph of the polished surface, shown in Figure 4.8, disclosed that the porosity was distributed homogeneously throughout the sample. Considerable amount of porosity was situated inside the grains. The pore-grain boundary separation was achieved. Therefore, the elimination of intragranular pores was retarded. The grains were equiaxed with an estimated average grain size of about 4 μm .

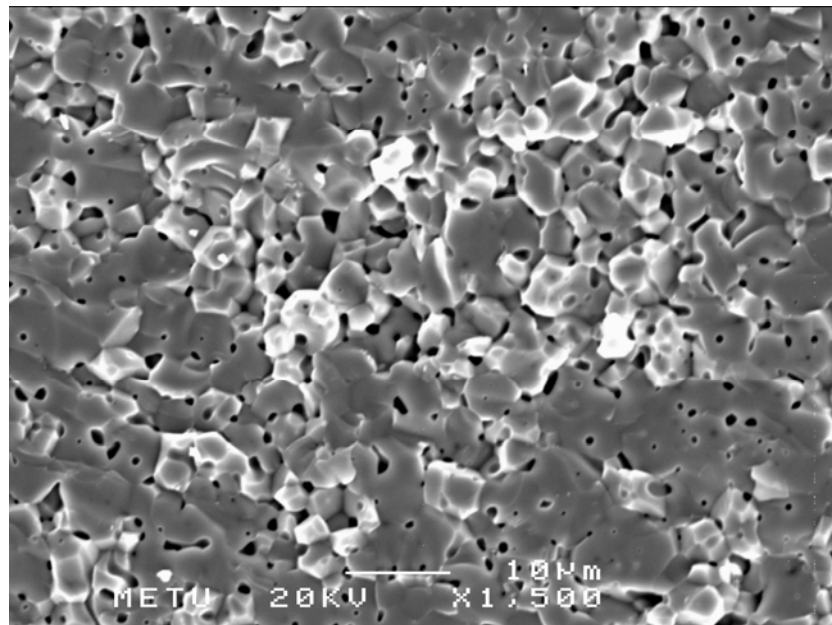


Figure 4.7 SEM fractograph of the NZF ceramic containing 0.75 wt% CaF_2 . Sample was soaked at 1200 °C for 2 hours.

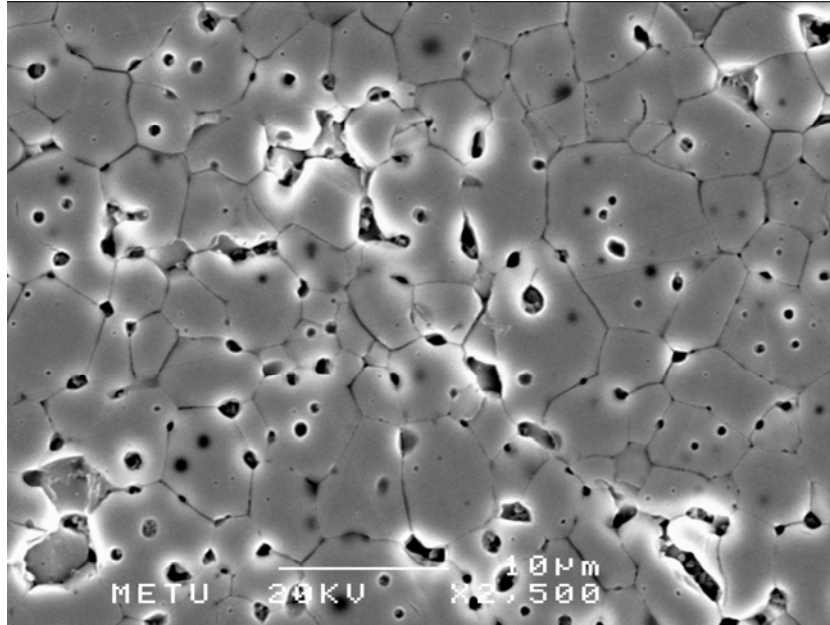


Figure 4.8 SEM micrograph of the NZF ceramic containing 0.75 wt% CaF_2 . The ceramic was soaked for 2 hours at 1200 °C.

SEM image of the NZF ceramic containing 1.0 wt% CaF_2 is presented in Figure 4.9. The micrograph revealed that the interfacial bonding between grains was fully developed as the fracture surface exposed was totally an intragranular section. The microstructural development was complete within a soak duration of 2 hours. The average grain size of the ceramic deduced from the polished surface in Figure 4.10 was close to 6 μm . The microstructure consisted of equiaxed grains. The spatial distribution of porosity in the ceramic was homogeneous.

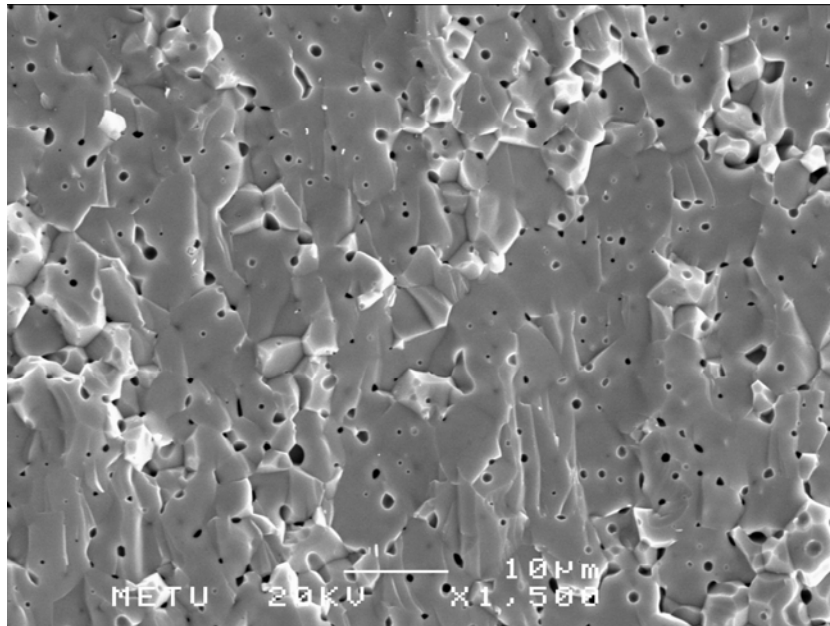


Figure 4.9 SEM fractograph of the NZF ceramic containing 1.0 wt% CaF₂. The ceramic was soaked for 2 hours at 1200 °C.

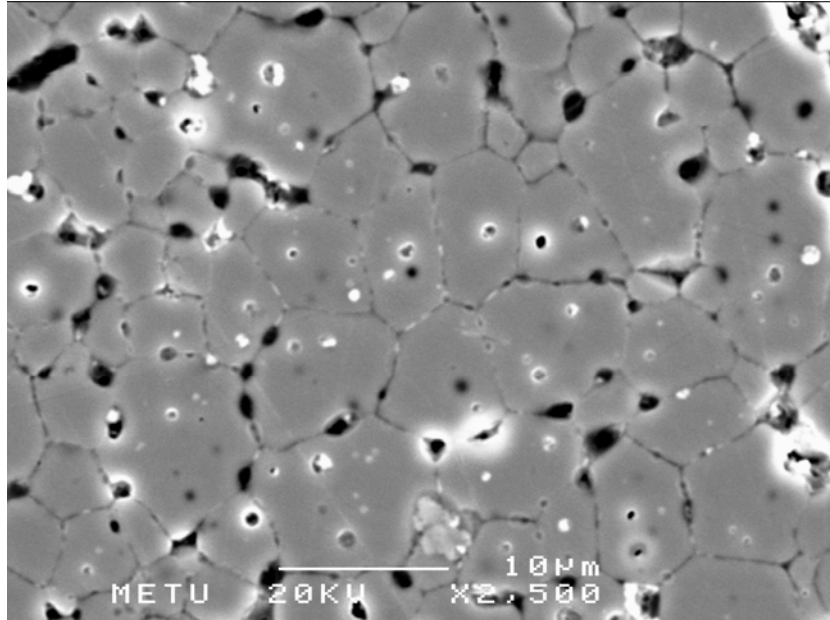


Figure 4.10 SEM micrograph of the NZF ceramic containing 1.0 wt% CaF₂. The sample was soaked for 2 hours at 1200 °C and etched.

The aforementioned SEM images of the NZF ceramics revealed that homogeneous microstructures were attained in all samples. The homogeneity in terms of chemical composition was also examined via the Energy Dispersive Spectroscopy (EDS) attachment of SEM. The results of EDS analyses are given below.

In order to see how Ca of the CaF_2 was distributed across the microstructure, the NZF ceramic containing 0.5 wt% CaF_2 and soaked for 18 hours at 1200 °C was subjected to EDS scan. The fractured section examined for this purpose is shown in Figure 4.11. The EDS spectra and the results of computations for chemical composition at the grain boundary and grain interior regions marked on Figure 4.11 were those given in Figures 4.12 and 4.13, respectively. The distribution of chemical constituents showed no evidence of chemical segregation either at grain boundary or in grain interior of the NZF ceramic.

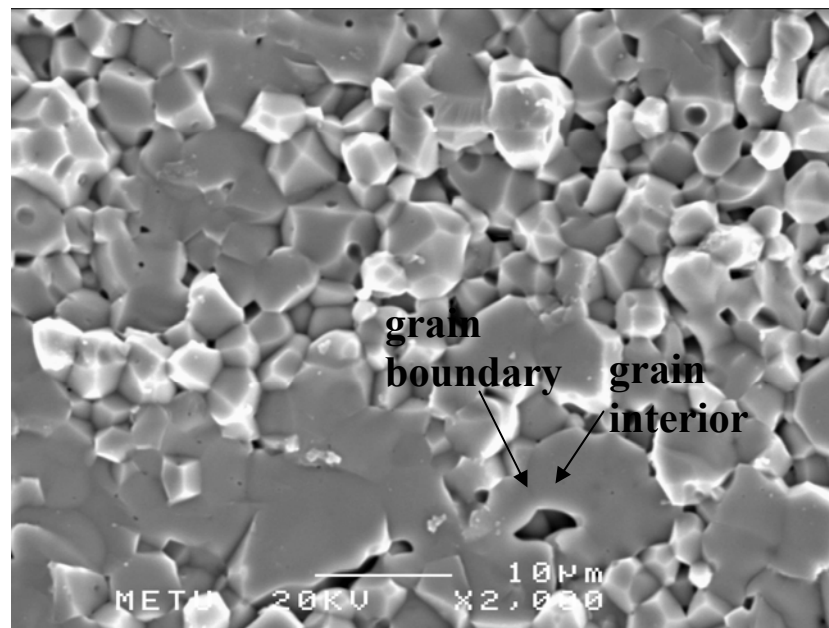


Figure 4.11 SEM fractograph of the NZF ceramic containing 0.5 wt% CaF_2 . Sample was soaked at 1200 °C for 18 hours.

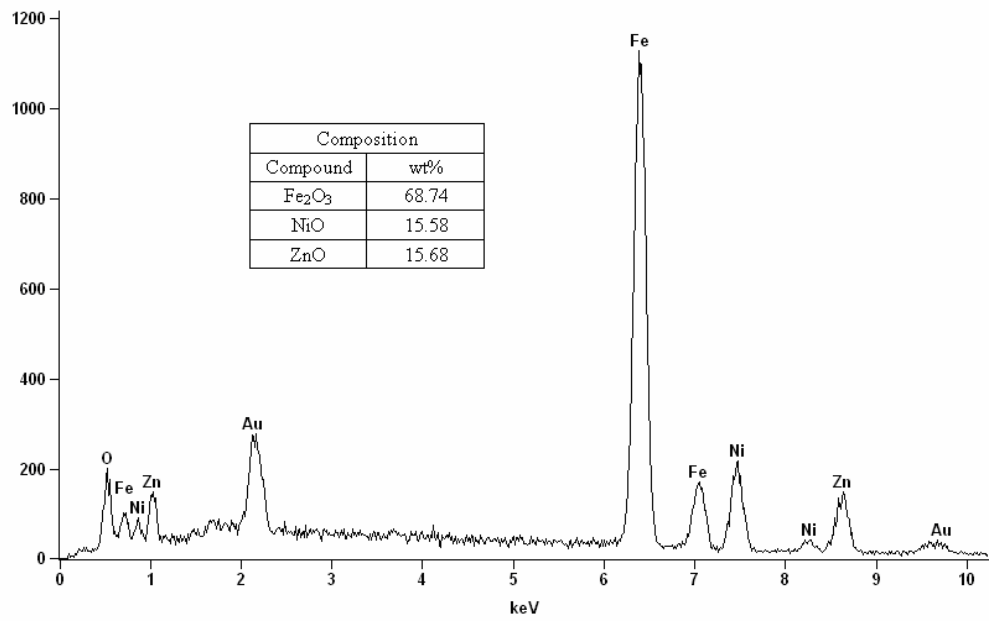


Figure 4.12 The EDS pattern of a grain boundary in the NZF ceramic containing 0.5 wt% CaF₂

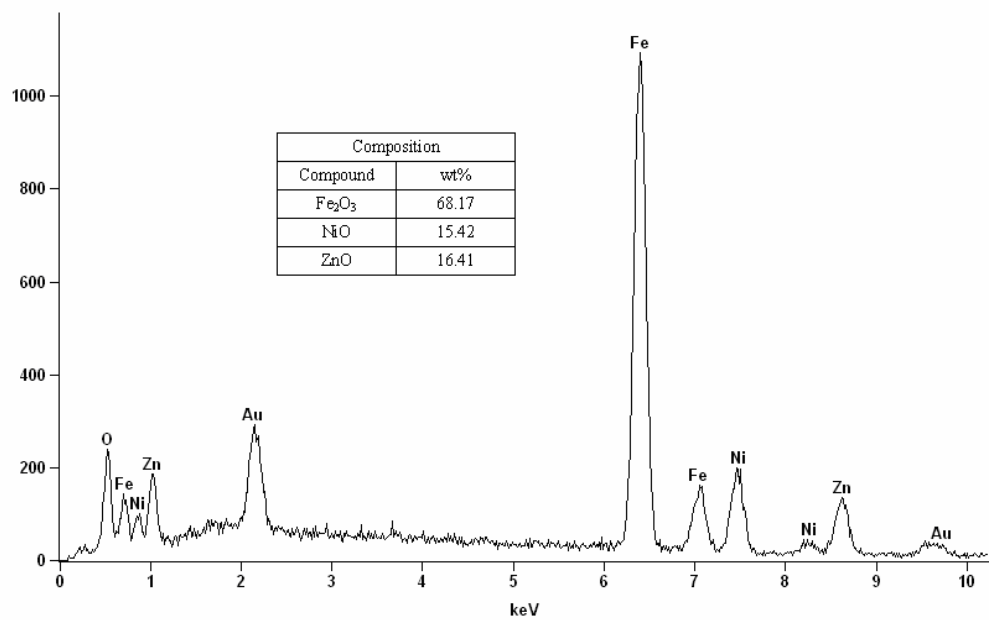


Figure 4.13 The EDS pattern of grain interior in the NZF tablet doped with 0.5 wt% CaF₂

Although SEM does not have sufficient resolution to yield reliable information on the exact chemical composition of the grain boundary, nonetheless the EDS analyses of the regions indicated on Figure 4.11 did not reveal large compositional differences between grains and grain boundaries. Within the sensitivity of EDS, Ca was detected neither at grain boundaries nor in the grains. From the data given on Figure 4.13 the molecular composition of the grain was ascertained as $(\text{NiO})_{0.506}(\text{ZnO})_{0.494}(\text{Fe}_2\text{O}_3)_{1.046}$. This formula predicted that some zinc loss had occurred during the sintering process but the original stoichiometric composition of the ceramic was largely preserved.

The microstructure of the NZF ceramic containing 1.0 wt% CaF_2 soaked at 1200 °C for 2 hours is shown in Figure 4.14. The EDS patterns obtained from locations marked as A and B on Figure 4.14 are presented in Figures 4.15 and 4.16. Location A represents grain boundary and location B represents grain interior.

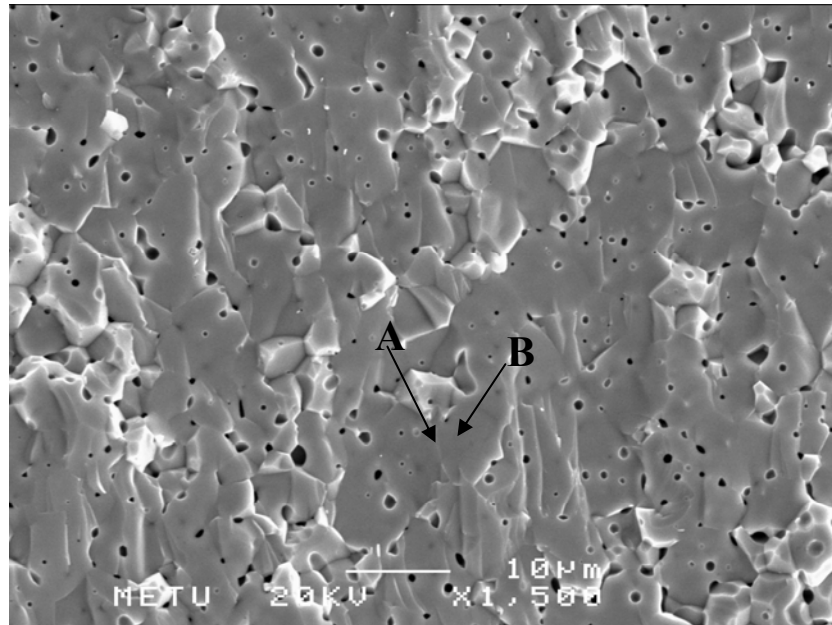


Figure 4.14 SEM fractograph of the NZF ceramic containing 1.0 wt% CaF_2 . Sample was soaked at 1200 °C for 2 hours.

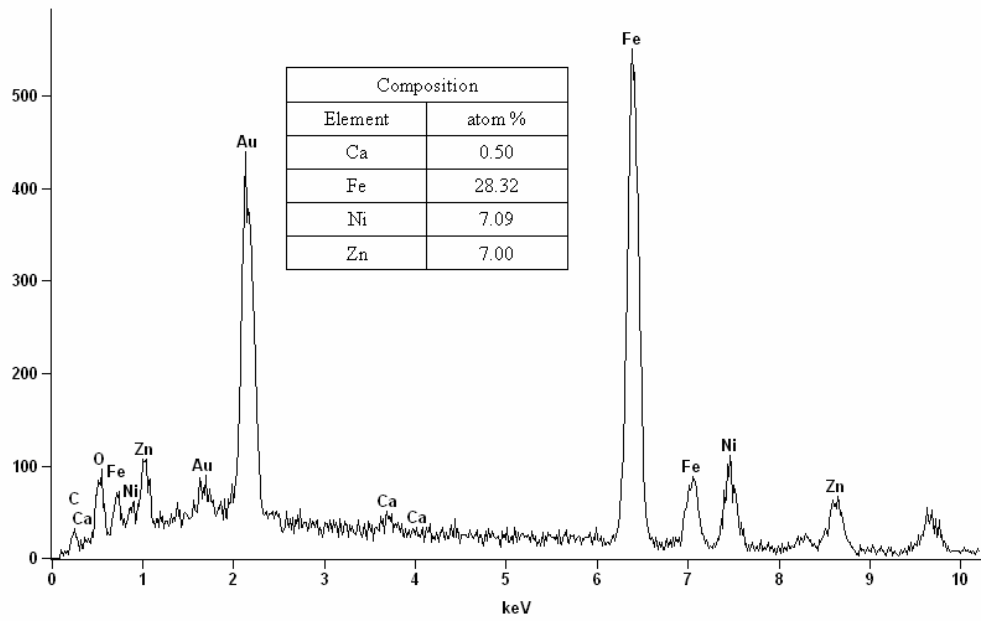


Figure 4.15 The EDS pattern obtained from the grain boundary of NZF ceramic containing 1.0 wt% CaF₂.

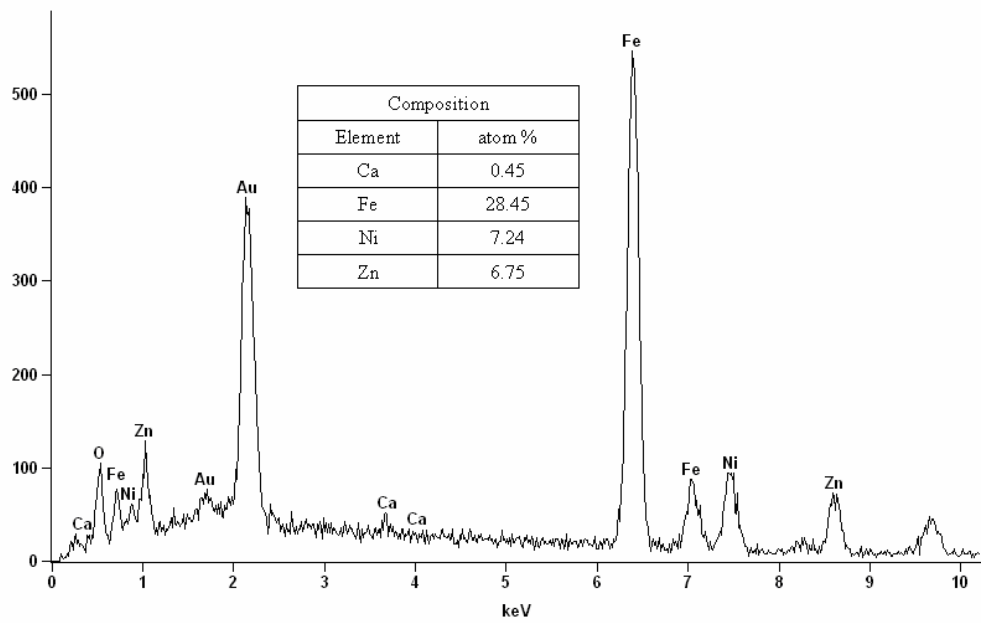
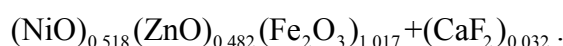


Figure 4.16 The EDS pattern of grain interior of 1.0 wt% CaF₂ added NZF disk.

The elemental analyses shown on the spectra did not suggest calcium segregation at grain boundaries. The data on elemental analysis of the grain was used for calculating the molecular formula of the NZF ceramic. In the calculations, Ca^{+2} ions were assumed to be bound to the F^- ions and CaF_2 was not associated with the spinel formula. The remaining cations; Ni^{+2} , Zn^{+2} and Fe^{+3} , were thought to be bound to the oxygen anions. This procedure yielded the following molecular representation:



The concentration of CaF_2 deduced from the above representation was 1.045 wt%. This was in excellent concordance with the original batch formulation of the ceramic. In addition, the molecular formula of the ferrite revealed that, within limits of analytical error, there was no appreciable variation in the original Fe^{3+} concentration of the ferrite. This was a clue for the preservation of chemical and structural homogeneity during sintering process. These observations were not confined to the sites marked in Figure 4.14 but covered the entire ceramic.

4.5 Microstructures by Optical Microscope

The examination of the polished and etched surfaces of sintered ferrite ceramics through optical microscope was useful because this yielded a clear picture of the overall microstructural features of the ceramics. In addition, useful quantitative information could be derived with respect to grain size and grain size distribution which led to the assessment of the mechanisms involved during the sintering process.

The optical micrograph of the NZF ceramic containing no CaF_2 displayed the duplex grain structure shown in Figure 4.17. The grains in the ceramic, which was soaked for 18 hours, could be categorized into two distinct size groups; it looked as if islands consisting of large grains were dispersed in a sea of fine grains. This kind of structure could be typically identified as a product of exaggerated grain

growth if a liquid phase would be present. Since there was no liquid in the present case, the reason for the unbalanced growth of some grains could be due to the straining of the NZF powder during milling and comminution processes.

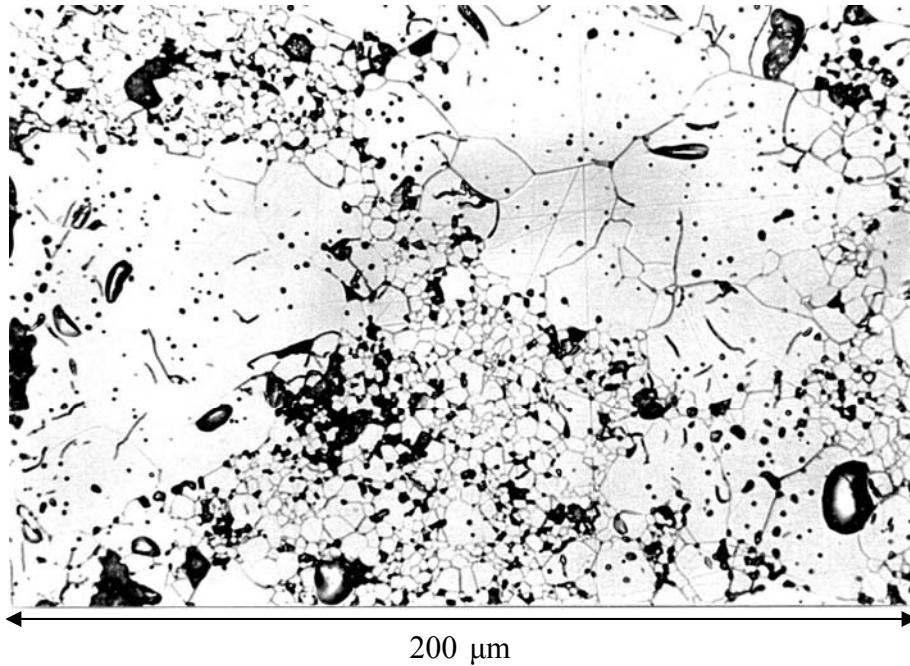


Figure 4.17 The optical micrograph of the NZF ceramic containing no CaF_2 . The sample was soaked for 18 hours at $1200\text{ }^\circ\text{C}$.

The optical micrograph of the NZF ceramic containing $0.5\text{ wt}\% \text{CaF}_2$, given in Figure 4.18, was quite different from the previous one. The duplex structure was absent and, in general, the grain size distribution was quite uniform. The grains were substantially free of pores. The black areas seen in the micrograph are due to the grain pull-out encountered in metallographic preparation.

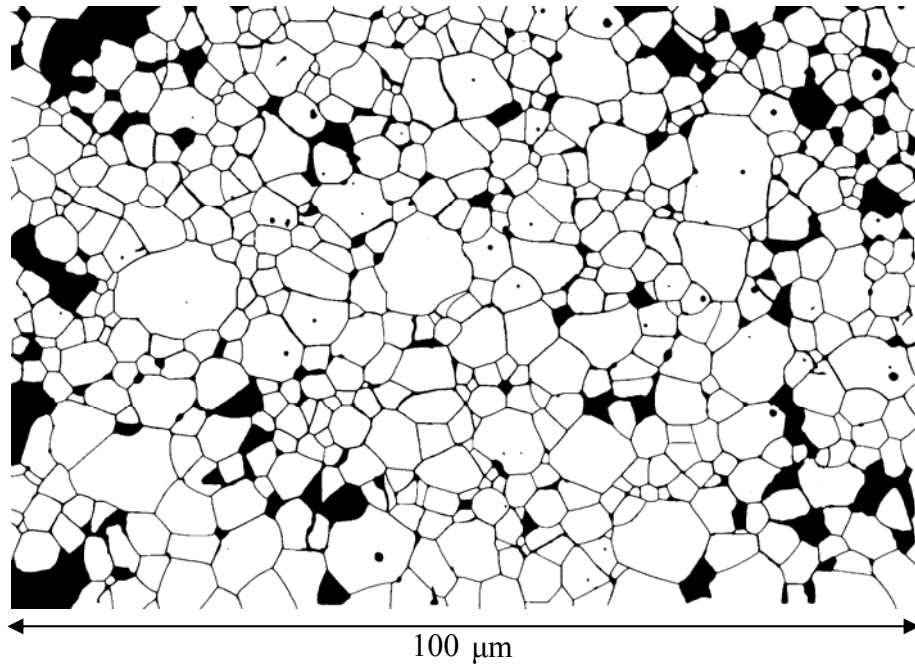


Figure 4.18 Optical micrograph of the ferrite containing 0.5 wt% CaF_2 . The sample was sintered for 18 hours at 1200 °C.

When the amount of CaF_2 addition was raised to 0.75 wt%, the grain growth process was accompanied with pore entrapment inside the grains. This was evident in the micrograph presented in Figure 4.19. The presence of intragranular porosity indicated that sintering was fast.

The enlargement of grains continued upon raising the CaF_2 addition to 1.0 wt%. Grains as large as 15 μm was apparent as seen in Figure 4.20. Here, the pores inside the grains grew larger as well, and their quantity seemed to increase.

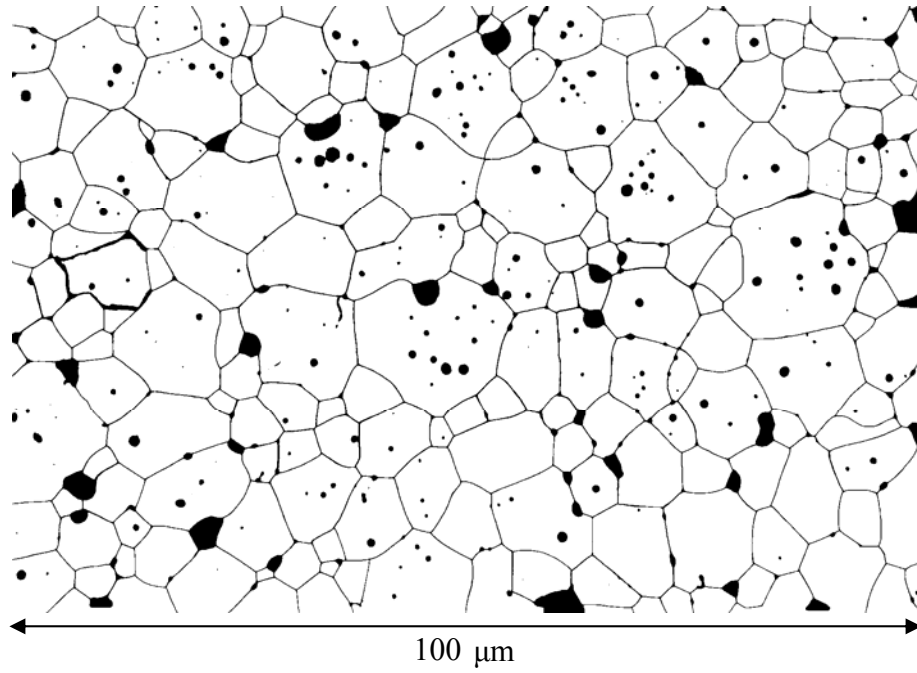


Figure 4.19 The microstructure of 0.75 wt% CaF₂ incorporated NZF sample after soaking at 1200 °C for 18 hours.

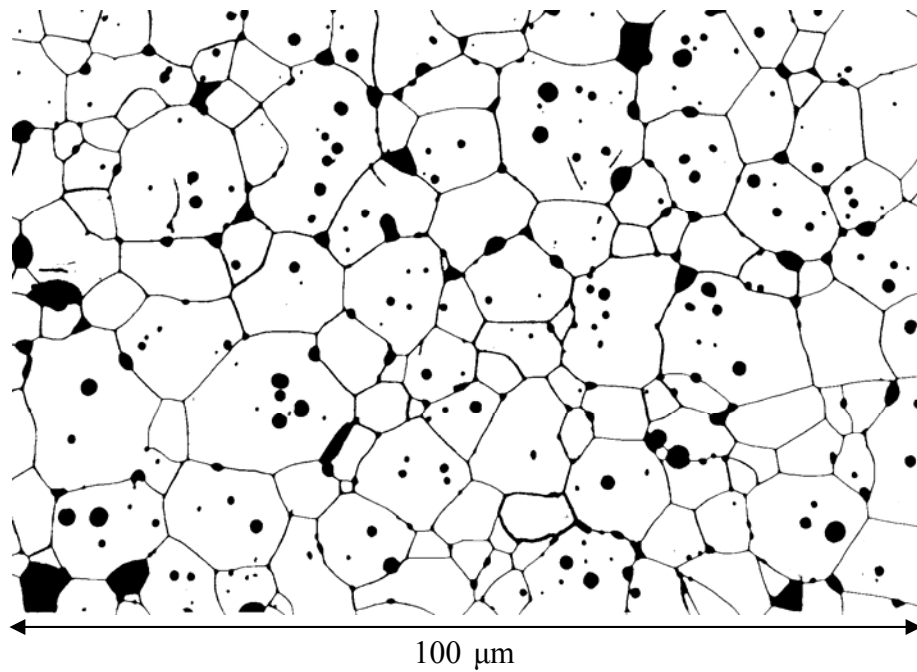


Figure 4.20 Optical micrograph of the NZF ceramic containing 1.0 wt% CaF₂. The ceramic was soaked for 18 hours at 1200 °C.

The micrographs of the NZF ceramics displayed above suggested that CaF_2 was effective not only as a mere sintering aid but also it helped in organizing the microstructure with respect to porosity and homogeneity in grain size. Local structural irregularities were not observed within the NZF ceramics containing some amounts of CaF_2 .

4.6 Grain Size and Grain Size Distribution

A data depository has been established for making a permanent record of the optical micrographs of all the NZF ceramics produced during this thesis work. The depository is accessible through the author of this manuscript and his advisor [54]. The micrographs in this depository were used for quantitative assessment of the grain size and the grain size distribution in the ceramics produced in this study.

All CaF_2 -free NZF ceramics exhibited duplex grain structure. Because of the difficulty in arriving at unambiguous average grain size determination these were excluded from quantitative grain size study. The method followed in obtaining grain size data and the subsequent treatment from the NZF ceramics containing CaF_2 has been explained already in Section 3.2.3.2.1. The histograms presented in Appendix A summarize graphically the information obtained from image analyses of the optical micrographs belonging to NZF ceramics sintered with the aid of CaF_2 . As an example, the histogram shown in Figure 4.21 was selected to represent the grain size distribution in the NZF ceramic containing 0.5 wt% CaF_2 which was sintered at 1200 °C for 18 hours.

In all CaF_2 containing NZF ceramics, the grain size distribution was of log-normal type which could be approximated by the following expression:

$$f = a \cdot \exp\left(-\frac{1}{2} \cdot \left(\frac{\ln\left(\frac{x}{G_0}\right)}{\sigma}\right)^2\right), \quad (4.3)$$

where :

- f : normalized frequency,
- a : a constant,
- x : circular radius,
- G_0 : mean of the log-normal distribution,
- σ : standard deviation of the distribution.

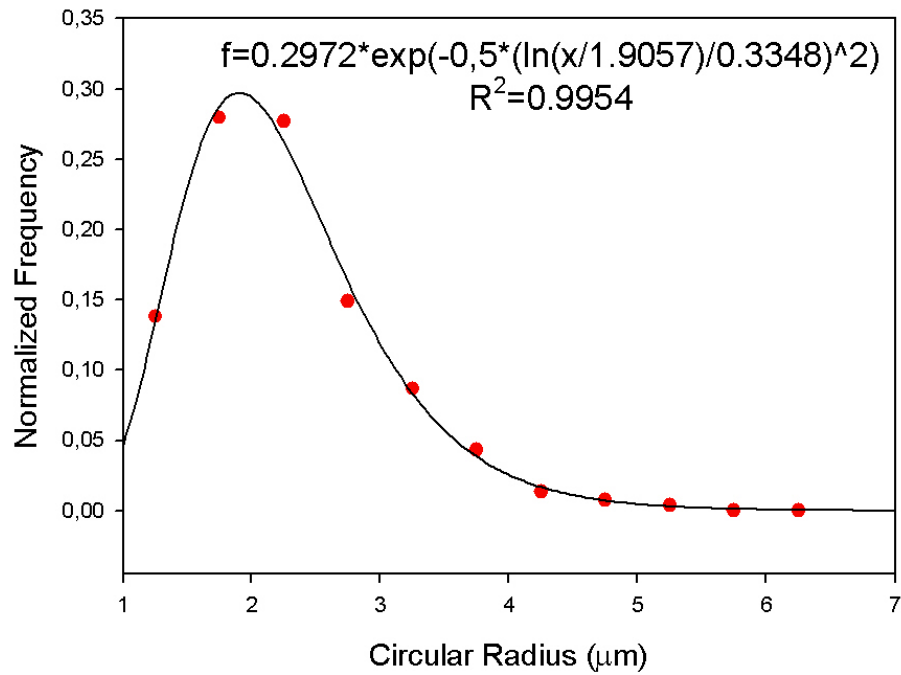


Figure 4.21 Experimentally determined grain size distribution in the NZF ceramic containing 0.5 wt% CaF_2 . The sample was soaked at 1200 °C for 18 hours.

Equation (4.3) was used to obtain information on the average grain size of the ceramic. The values obtained for the mean grain size, G , and the deviations there from, are given in Table 4.4.

Table 4.4 The variation of average grain size with soaking time and with the amount of CaF₂.

Soaking Time (hours)	Average Grain Size (μm)		
	wt% CaF ₂ addition		
	0.5	0.75	1.0
2	2.85 \pm 0.02	4.28 \pm 0.05	5.60 \pm 0.13
6	3.28 \pm 0.12	5.20 \pm 0.07	6.84 \pm 0.11
12	3.64 \pm 0.04	5.82 \pm 0.10	7.83 \pm 0.06
18	3.81 \pm 0.03	6.05 \pm 0.10	8.40 \pm 0.10

4.6.1 Factors Effecting Average Grain Size

As seen in Table 4.4, soaking time has a profound effect on average grain size of the NZF ceramics. Figure 4.22 was constructed to show the changes that would occur in the average grain size with extended soaking time at the peak sintering temperature of 1200 °C.

The curves in Figure 4.22 suggested that at all CaF₂ additions the grain size increased linearly with the extent of the soak period. Furthermore, the change in the average grain size exhibited a linear dependence on the soak duration when the time axis was chosen logarithmic. The rate of grain growth, measured as the slope of the respective line, was highest for the NZF ceramics containing the highest amount of CaF₂.

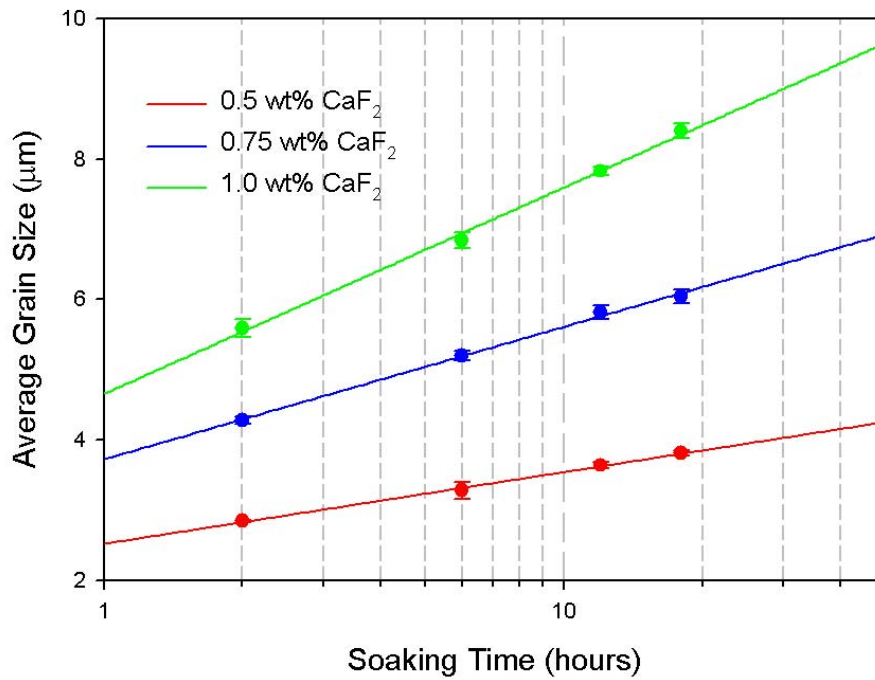


Figure 4.22 The effect of soaking time on average grain size of the NZF ceramics containing various amounts of CaF₂.

Small amount of CaF₂ additions had a critical role with respect to the increase in grain size and the tendency of grain growth. The data given in Table 4.4 was used to display graphically the effect of CaF₂ additions on the grain growth process. Figure 4.23 indicated that, irrespective of the soak period, the NZF ceramics containing 1.0 wt% CaF₂ attained highest values in the average grain size.

Within the range of CaF₂ additions studied in this thesis, the average grain size in the NZF ceramics exhibited a linear fit with CaF₂ additions. The four lines displayed in Figure 4.23 intersected at around 0.25 wt% CaF₂. As a speculation, the point of intersection could be interpreted as the minimum amount of CaF₂ required for the passage to the grain growth mechanism that resulted in the disappearance of the duplex grain morphology observed earlier in the CaF₂-free NZF ceramics.

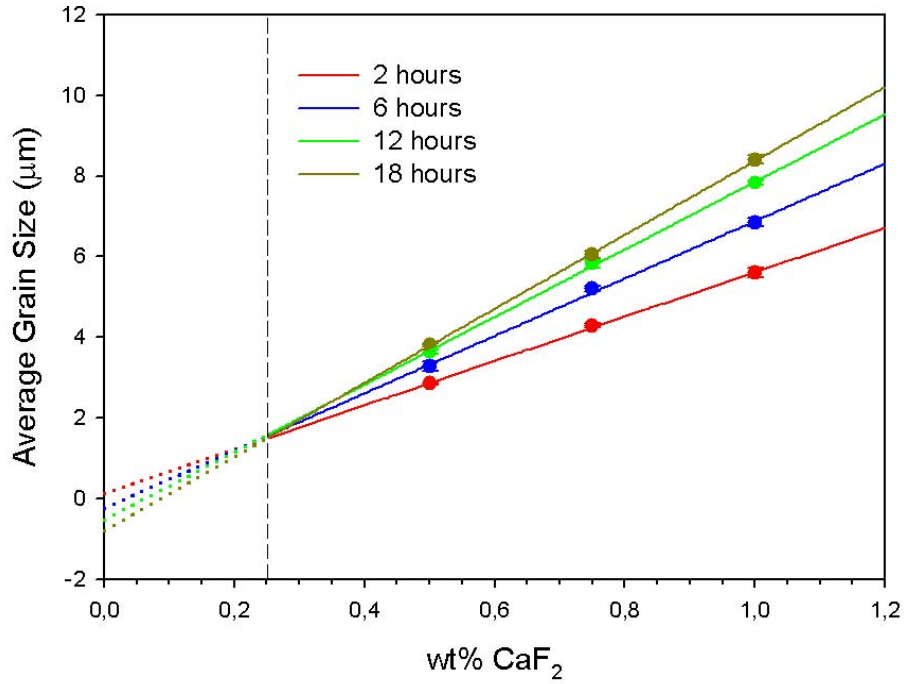


Figure 4.23 Variation in average grain size of the NZF ceramics with CaF₂ addition for different soaking durations.

4.7 Densification Mechanism

According to the commonly accepted sintering models, the densification rate equation could be written in the following general form [55-60]:

$$\frac{d\rho}{dt} = \frac{CN_g D \gamma \Omega}{kTG^n}, \quad (4.4)$$

where: $\frac{d\rho}{dt}$: densification rate at time t,

$\rho = \frac{\rho_{\text{bulk}}}{\rho_{\text{x-ray}}}$: fractional density of ceramic,

C : a constant,

N_g : number of pores per grain at time t,

D : diffusion constant of rate determining specie,

γ : solid-gas surface energy,
 Ω : volume of rate controlling specie,
 k : Boltzmann's constant,
 T : peak sintering temperature,
 G : average grain size at time t ,
 n : grain size exponent.

The value of the index “ n ” in the above expression has been accepted to serve as a guide for assessing the predominant mechanism prevailing in the sintering process. For example, in solid state sintering a value like $n = 3$ would indicate bulk diffusion controlled densification mechanism [56], and $n = 4$ would mean that densification is controlled by surface diffusion [57]. Values of n lower than 3 would indicate the involvement of a liquid phase in the sintering process [60].

Taking the logarithm of both sides in Equation (4.4) we get:

$$\log\left(\frac{dp}{dt}\right) = \log\left(\frac{CN_g D\gamma\Omega}{kT}\right) - n \cdot \log G . \quad (4.5)$$

For sake of simplicity, Equation (4.5) was normalized with respect to N_g by rearranging it as follows:

$$\log\left(\frac{dp}{dt} \cdot \frac{1}{N_g}\right) = \log\left(\frac{CD\gamma\Omega}{kT}\right) - n \cdot \log G . \quad (4.6)$$

The parameters of importance for the determination of “ n ” were $\log G$ and $\log\left(\frac{dp}{dt} \cdot \frac{1}{N_g}\right)$. For each ceramic produced in the experiments, $\log G$ values were calculated from the G values listed in Table 4.4. The $\frac{dp}{dt}$ term in the left-hand-side of Equation (4.6) was evaluated as the derivative of the time-dependent

densification equations given in Table 4.3. The number of pores per grain, N_g , was obtained by considering the following expression proposed for N_g [57]:

$$N_g = \frac{8\sqrt{\pi}}{27\sqrt{3}} * \frac{N_A^{3/2} * G^3}{(1-\rho)^{1/2}}. \quad (4.7)$$

Here, N_A represented the number of pores per unit area (# of pores/ μm^2), G and ρ were the same as in Equation (4.4). In order to arrive at N_A , the pores in the optical micrographs of the sintered NZF ceramics were treated quantitatively. The values of the parameters $\left(\frac{d\rho}{dt} \cdot \frac{1}{N_g}\right)$ and G needed for the treatment of Equation (4.4) are listed in Table 4.5.

Table 4.5 Values of the parameters relevant to the assessment of densification mechanism in the NZF ceramics sintered with the aid of CaF_2 .

		t	$\frac{dp}{dt}$	N_A	$N_A^{3/2}$	G	G^3	ρ	$(1 - \rho)$	$(1 - \rho)^{1/2}$	N_g	$\frac{dp}{dt} \cdot \frac{1}{N_g}$
wt% CaF_2 addition	0.5	2	5.63×10^{-3}	0.0759	0.0209	2.8458	23.0469	0.9381	0.0619	0.2488	0.5874	9.577×10^{-3}
		6	1.88×10^{-3}	0.0547	0.0128	3.2804	35.3005	0.9507	0.0493	0.2220	0.6170	3.039×10^{-3}
		12	9.38×10^{-4}	0.0468	0.0101	3.6378	48.1411	0.9582	0.0418	0.2045	0.7232	1.296×10^{-3}
		18	6.25×10^{-4}	0.0397	0.0079	3.8114	55.3673	0.9629	0.0371	0.1926	0.6892	9.070×10^{-4}
	0.75	2	5.00×10^{-3}	0.0693	0.0182	4.2836	78.6008	0.9363	0.0637	0.2524	1.7229	2.900×10^{-3}
		6	1.67×10^{-3}	0.0546	0.0128	5.1976	140.4134	0.9487	0.0513	0.2265	2.3981	6.945×10^{-4}
		12	8.33×10^{-4}	0.0437	0.0092	5.8208	197.2187	0.9546	0.0454	0.2131	2.5681	3.243×10^{-4}
		18	5.55×10^{-4}	0.0414	0.0084	6.0450	220.8965	0.9583	0.0417	0.2042	2.7641	2.009×10^{-4}
	1.0	2	4.57×10^{-3}	0.0734	0.0199	5.5952	175.1648	0.9375	0.0625	0.2500	4.2244	1.083×10^{-3}
		6	1.52×10^{-3}	0.0561	0.0133	6.8410	320.1539	0.9473	0.0527	0.2296	5.6134	2.716×10^{-4}
		12	7.62×10^{-4}	0.0528	0.0121	7.8292	479.9016	0.9538	0.0462	0.2149	8.2194	9.273×10^{-5}
		18	5.08×10^{-4}	0.0508	0.0115	8.4002	592.7463	0.9576	0.0424	0.2059	10.0010	5.081×10^{-5}

The variation of the normalized densification rate with respect to the average grain size in the NZF ceramics are shown in Figure 4.24. Both axes in the figure are logarithmic.

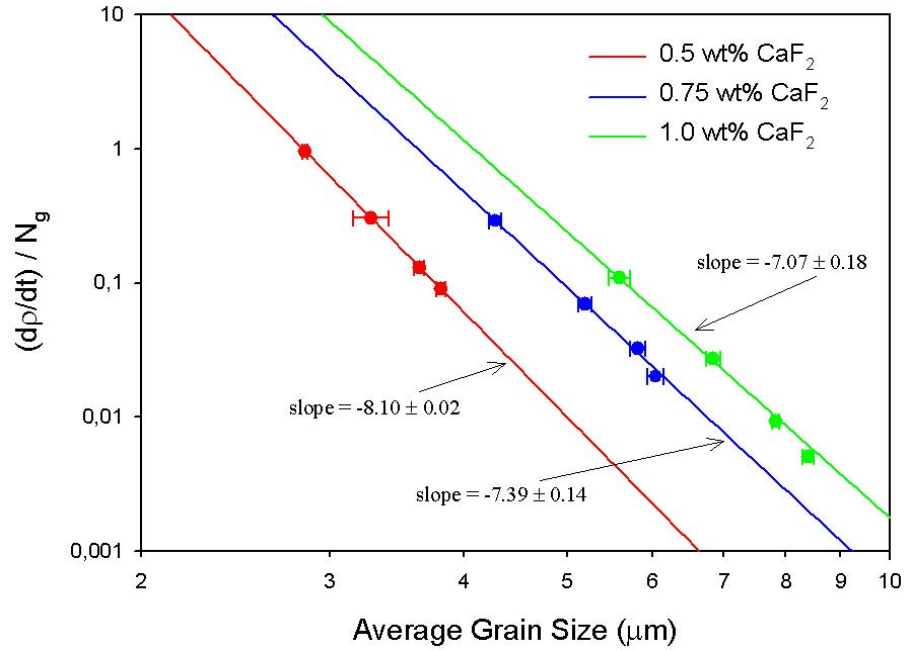


Figure 4.24 Effect of CaF₂ content on densification behavior of NZF ceramics.

The data for each NZF ceramic could be fitted with straight lines expressed by the following equations:

$$\text{For CaF}_2 = 0.50 \text{ wt\%,} \quad \log\left(\frac{dp}{dt} \cdot \frac{1}{N_g}\right) = 3.66 - 8.10 \cdot \log G . \quad (4.8)$$

$$\text{For CaF}_2 = 0.75 \text{ wt\%,} \quad \log\left(\frac{dp}{dt} \cdot \frac{1}{N_g}\right) = 4.13 - 7.39 \cdot \log G . \quad (4.9)$$

$$\text{For CaF}_2 = 1.00 \text{ wt\%,} \quad \log\left(\frac{dp}{dt} \cdot \frac{1}{N_g}\right) = 4.32 - 7.07 \cdot \log G . \quad (4.10)$$

The value of the grain size exponent “n” obtained from the above equations for different amounts of CaF₂ addition, were tabulated in Table 4.6.

Table 4.6 Values of the grain size exponent “n” with respect to wt% CaF₂ addition.

wt% CaF ₂ addition	“n”
0.50	8.10 ± 0.02
0.75	7.39 ± 0.14
1.00	7.07 ± 0.18

The values for “n” were quite larger than the densification exponents 3 and 4 encountered commonly in solid state sintering process. Hence, on the basis of the results presented, the densification in the NZF ceramics containing some amount of CaF₂ must have involved other mechanisms which interfered with the kinetic aspects of solid state sintering.

4.8. Electrical Properties

The electrical properties of interest were the alterations in the electrical resistivity of the NZF ceramic due to CaF₂ additions as well as the changes in the dielectric properties, reflected in the dielectric constant and the related loss tangent.

4.8.1 Electrical Resistivity

DC electrical resistivity measurements were carried out on sintered ferrites according to the procedure described in Section 3.2.3.3.1. The voltage-current relationship defined by the Ohm’s Law was used to determine the electrical resistance, R, of the ceramics:

$$V = I \cdot R = I \cdot \rho \cdot \frac{t}{A} \quad (4.11)$$

To calculate the resistivity, this expression was re-written as:

$$\rho = \frac{V \cdot A}{I \cdot t}, \quad (4.12)$$

where: V: the potential difference between two probes, Volt,
I: current passing through the ceramic, Ampere,
R: resistance of the ceramic, Ohm,
 ρ : DC electrical resistivity of the ceramic, Ohm-cm,
t: thickness of the ceramic, cm,
A: area of the metallic electrode of the ceramic, cm².

The results on electrical resistivity determination are given in Table 4.7. According to the data given in this table the NZF ceramics without CaF₂ exhibited much lower resistivities than those which contained some amount of CaF₂. This could be attributed to the differences in the concentration and mobility of charge carriers. In all composition groups, the resistivity decreased with longer soak duration. These effects were believed to be related to the grain size; as expected, for a ceramic of fixed chemical composition the grain growth caused decline in resistivity.

Table 4.7 DC electrical resistivity of NZF ceramics prepared in this thesis.

Soaking Time (hours)	DC Electrical Resistivity ρ , (Ω -cm)			
	wt% CaF ₂ addition			
	0.0	0.5	0.75	1.0
2	2.441×10^6	1.050×10^9	1.073×10^{10}	1.384×10^{11}
6	5.318×10^5	7.139×10^7	7.736×10^8	7.923×10^9
12	2.087×10^5	1.081×10^7	8.499×10^7	7.085×10^8
18	1.565×10^5	3.308×10^6	4.584×10^7	2.038×10^8

The data on electrical resistivity given in Table 4.7 were combined with the information on grain size of the ceramics provided in Table 4.4 to display the variation of DC electrical resistivity with average grain size, as shown in Figure 4.25. When DC electrical resistivity was drawn on a logarithmic scale, in each ceramic group having a distinct CaF₂ addition, a linear relationship was obtained between average grain size and the logarithm of DC electrical resistivity. This behavior verified the following empirical relationship for the dependence between electrical resistivity, ρ , and grain size, G :

$$\rho = a \cdot e^{(-b \cdot G)}, \quad (4.13)$$

where a and b are positive constants.

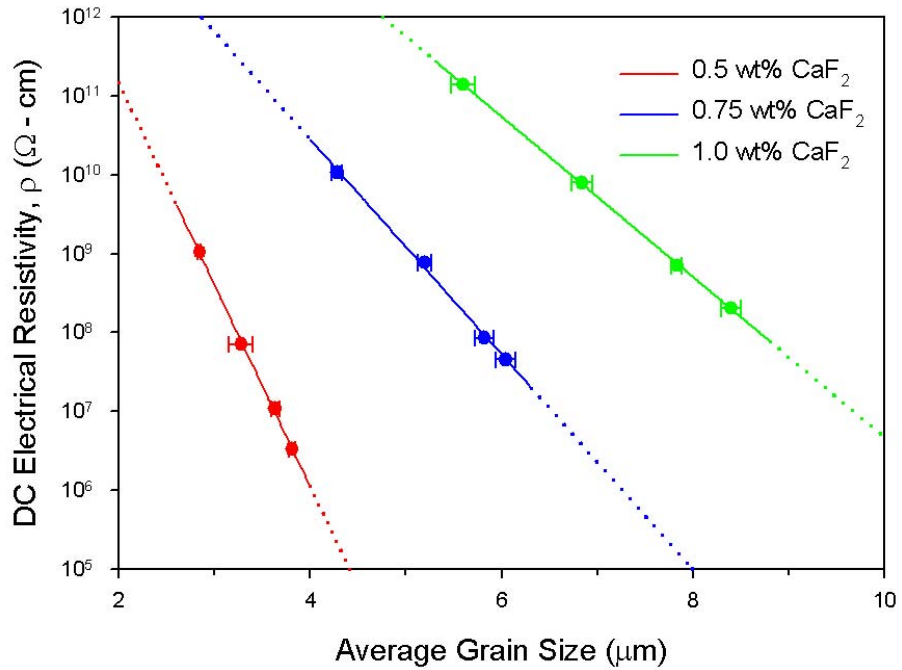


Figure 4.25 The variation in DC electrical resistivity of the NZF ceramics with respect to average grain size for various amount of CaF₂ additions.

Strikingly, CaF₂ played a profound role on electrical resistivity. The effect of CaF₂ additions on electrical resistivity was far beyond that of the grain size. Although the grain size of the ceramic would increase by CaF₂ additions the electrical resistivity exhibited large hikes upon increasing the CaF₂ amount. This behavior could be illustrated graphically in Figure 4.26. The curves suggest that, for a prescribed sintering duration, the electrical resistivity would increase by about two orders of magnitude when CaF₂ content was doubled.

The increase in resistivity accompanying with the CaF₂ addition could be attributed to the alterations that might have taken place in the electronic structure of the ferrite. Although this subject will be elaborated further in later parts of the thesis, it should suffice here to state that small additions of CaF₂ seemingly hindered the charge mobility giving rise to loss in electrical conductivity. In service, this feature is a big advantage for ceramics.

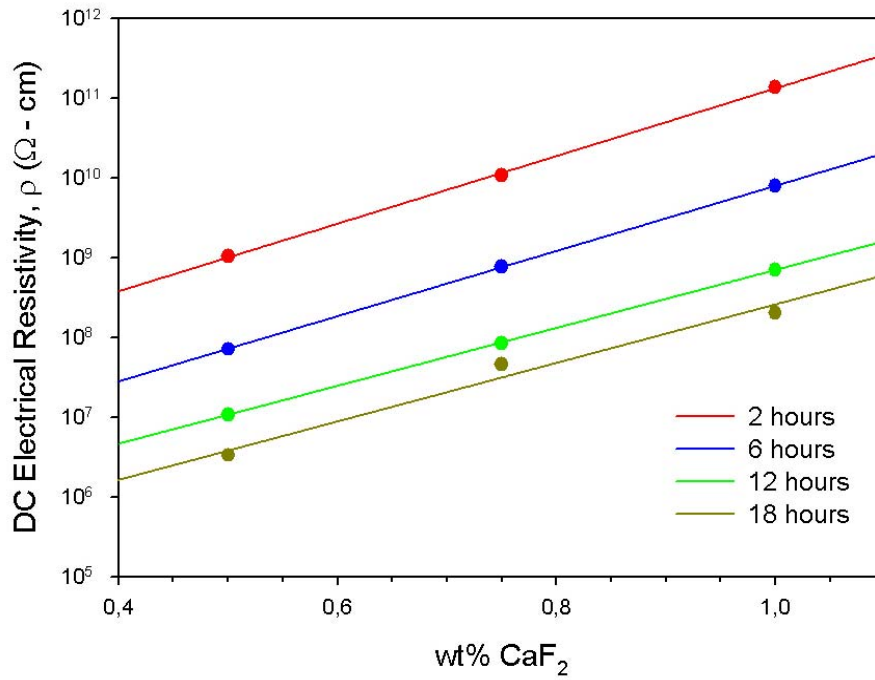


Figure 4.26 The effect of CaF₂ on the electrical resistivity of NZF ceramics studied in this thesis.

4.8.2 Dielectric Properties

The dielectric properties of the NZF ceramics were examined by following the procedure described in Section 3.2.3.3.2. The capacitance “C” and the dielectric loss tangent “ $\tan\delta_\epsilon$ ” of the ceramics were measured over a wide frequency range starting from 100 Hz and running up to 40 MHz, the maximum being limited by the capability of the HP 4194A Gain Phase Analyzer.

4.8.2.1. Dielectric Constant

Following expression was used in the calculation of the dielectric constant ϵ from the measured capacitance C, and the geometry of the sample:

$$C = \epsilon_0 \cdot \epsilon \cdot \frac{A}{t}, \quad (4.14)$$

where: ϵ_0 : dielectric permittivity of space, $8.854 \cdot 10^{-14}$ Farad/cm,
A: metallized area of one circular face, cm^2 ,
t: thickness of the ceramic, cm.

4.8.2.1.1 Dielectric Constant of the CaF_2 -free NZF Ceramics

In the NZF ceramic containing no CaF_2 , the variation of the dielectric constant with sintering time and frequency is displayed with the curves as shown in Figure 4.27. Three features were worth mentioning: (a) the dielectric constant exhibited a smooth and continuous decline with increased frequency, (b) at a fixed frequency the dielectric constant of the ceramic sintered for longer soaking duration was higher, and (c) at very high frequencies the dielectric constant curves converged.

These effects will be discussed in detail in Section 4.8.2.1.2.

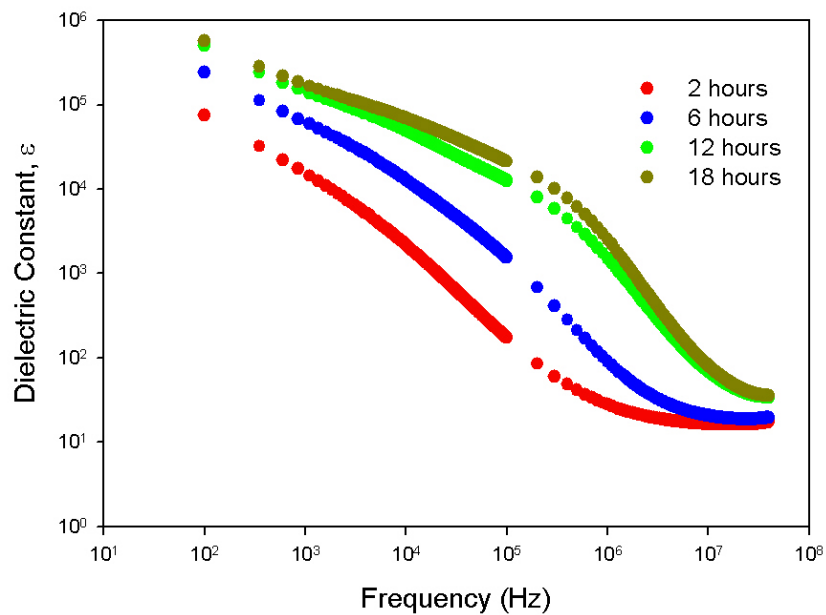


Figure 4.27 Variation of the dielectric constant of the NZF ceramics with frequency and sintering duration.

4.8.2.1.2 Dielectric Constant of NZF Ceramics Containing CaF₂

The effect of CaF₂ additions on the dielectric constant of the NZF ceramics produced at different soak durations were expressed by the diagrams given in Figures 4.28 through 4.31. The one shown in Figure 4.28 represents the influence of CaF₂ additions for a fixed sintering period of 2 hours. At low frequencies, in the KHz range, addition of 0.5 wt % CaF₂ to the CaF₂-free NZF ceramic resulted in a drastic decline in the dielectric constant. The same effect was observed with increased CaF₂ additions. These changes were attributed to the weakening in the polarizability of the NZF ceramic by the incorporation of CaF₂. The dielectric constant of the ceramic containing 1 wt% CaF₂ on was almost constant, indicating that the charge storage capacity of this ceramic remained insensitive to the variations in the external field.

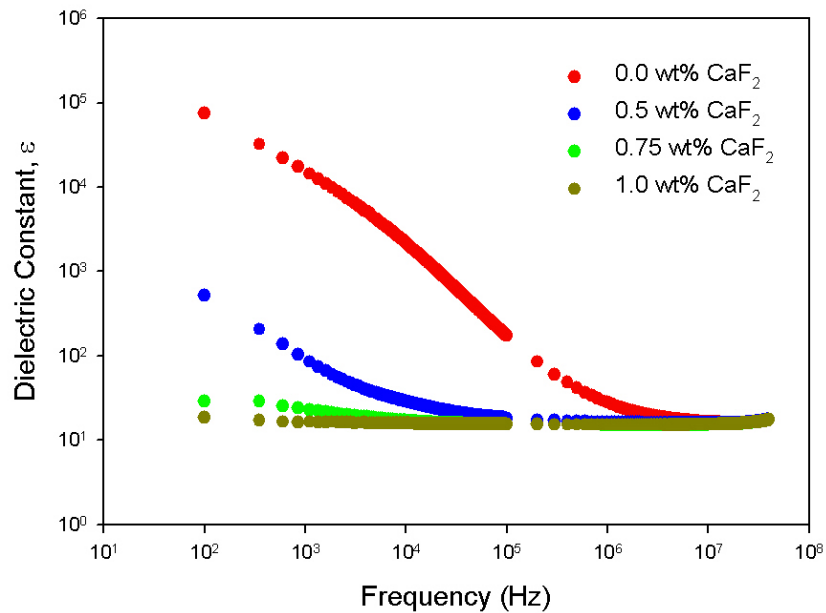


Figure 4.28 The effect of CaF₂ additions on the dielectric constant of NZF ceramics containing CaF₂. Soak duration was 2 hours.

Figures 4.29 through 4.31 illustrate the effect of prolonged sintering on the dielectric constant. As the soak duration at the peak sintering temperature was extended, the baseline in the dielectric curves tended to shift to higher ϵ values. This behavior, which represented increased polarization tendency, was related to the electronic events that took place in the grains of the NZF ceramic and to the disorder at grain boundaries during the sintering process.

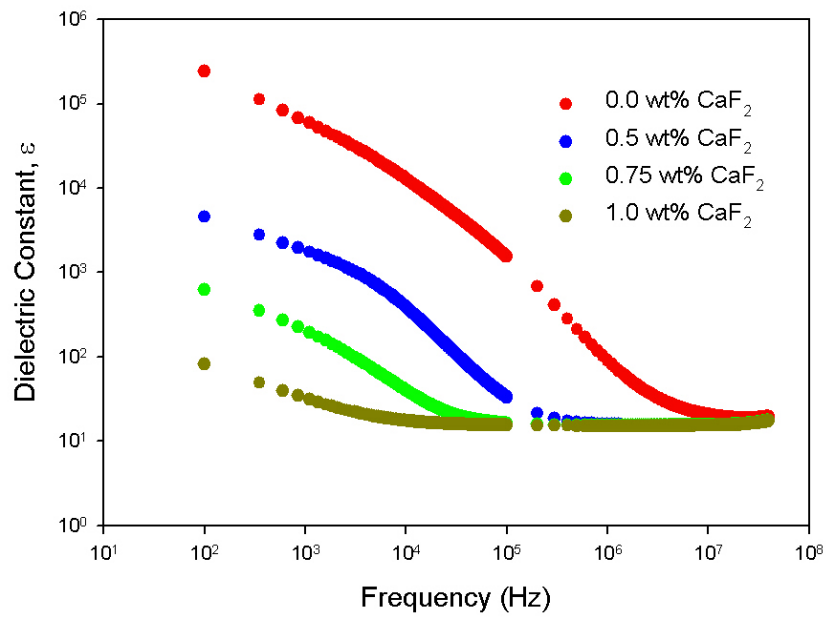


Figure 4.29 The effect of CaF₂ additions on the dielectric constant of NZF ceramics containing CaF₂. Soak duration was 6 hours.

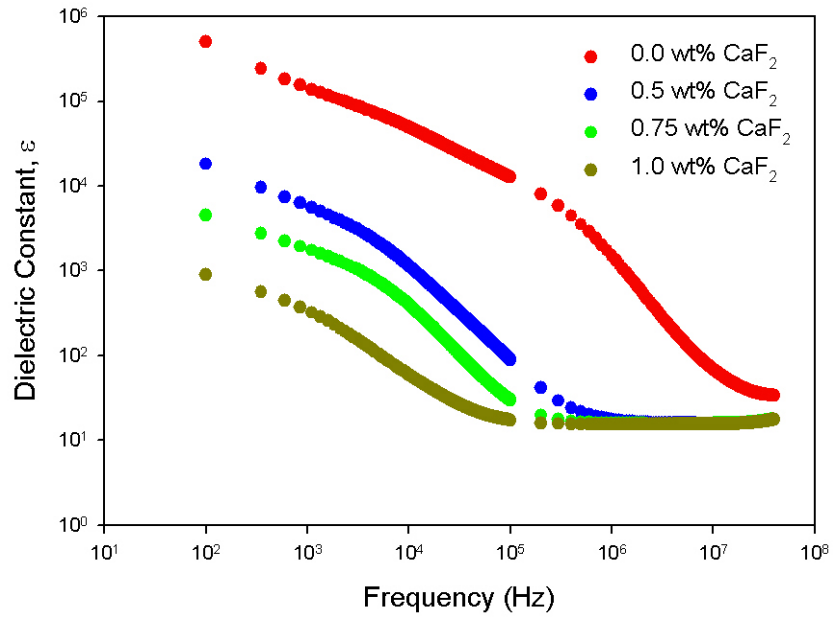


Figure 4.30 The effect of CaF₂ additions on the dielectric constant of NZF ceramics containing CaF₂. Soak duration was 12 hours.

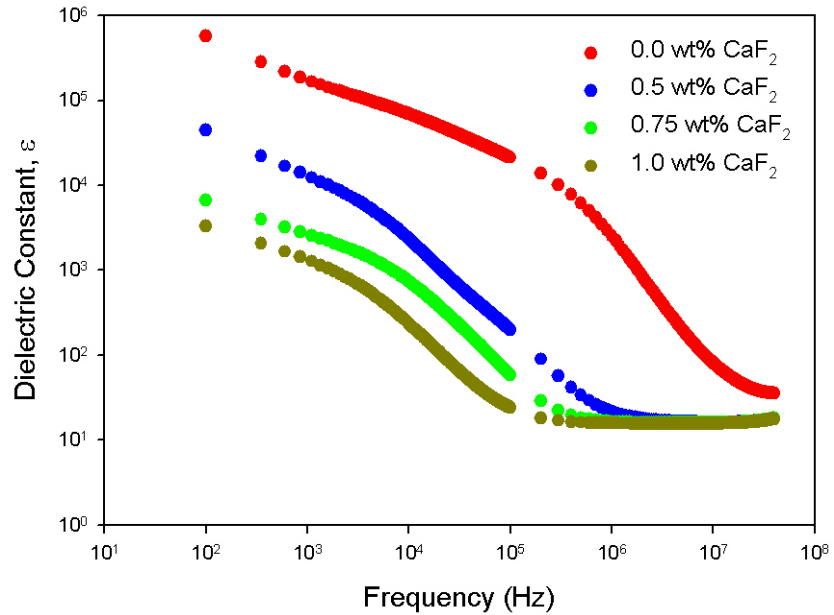


Figure 4.31 The effect of CaF₂ additions on the dielectric constant of NZF ceramics containing CaF₂. Soak duration was 18 hours.

The ferrite ceramics are known to consist of conducting grains separated from each other by poorly conducting grain boundaries [61, 62]; the conductivity in the grains being ascribed to the hopping mechanism that prevails between Fe^{+3} and Fe^{+2} ions [20, 24]. When the ceramic is exposed to an external electric field the electrons reaching the grain boundary pile up there if the resistance of the grain boundary is sufficiently high. As the frequency is increased the electrons reverse their direction of motion more often. This decreases the population of electrons reaching the grain boundary, as a result the polarization decreases. The continuous decline observed with increased frequency in the dielectric constant curves is due to this effect.

When ferrite ceramics containing zinc are fired at high temperatures zinc losses occur due to the vaporization tendency of this element [38, 63]. Higher sintering temperatures and/or longer soak durations increase these losses. During the evaporation of zinc a commensurate amount of the neighboring Fe^{+3} cations are converted to Fe^{+2} state. The increased presence of ferrous ions, Fe^{+2} , creates more hopping sites which lead to enhanced conduction. Therefore the electron pile-up at the grain boundaries tends to increase. In addition, the Fe^{+2} ion is stated to be more polarizable than the Fe^{+3} ion [38]. These effects are the main causes which shift the dielectric constant curves to higher values upon prolonged soak periods.

4.8.2.2. Dielectric Loss Factor

The data on the dielectric loss factor, $\tan\delta_\epsilon$, was used for examining the effects of sintering conditions and of CaF_2 additions on the lossy characteristics of the NZF ceramics. Figure 4.32 shows the loss behavior of the CaF_2 -free NZF ceramic. The ceramic manufactured with low soaking period exhibited a diffuse maximum in the low frequency range, around 10^3 Hz. As the soak duration was extended the maximum in the loss curve shifted towards higher frequencies. The NZF ceramics soaked for 12 hours exhibited a sharp peak at a frequency like 400

KHz. When the soaking period was raised to 18 hours the frequency of the peak remained almost unchanged but its amplitude increased.

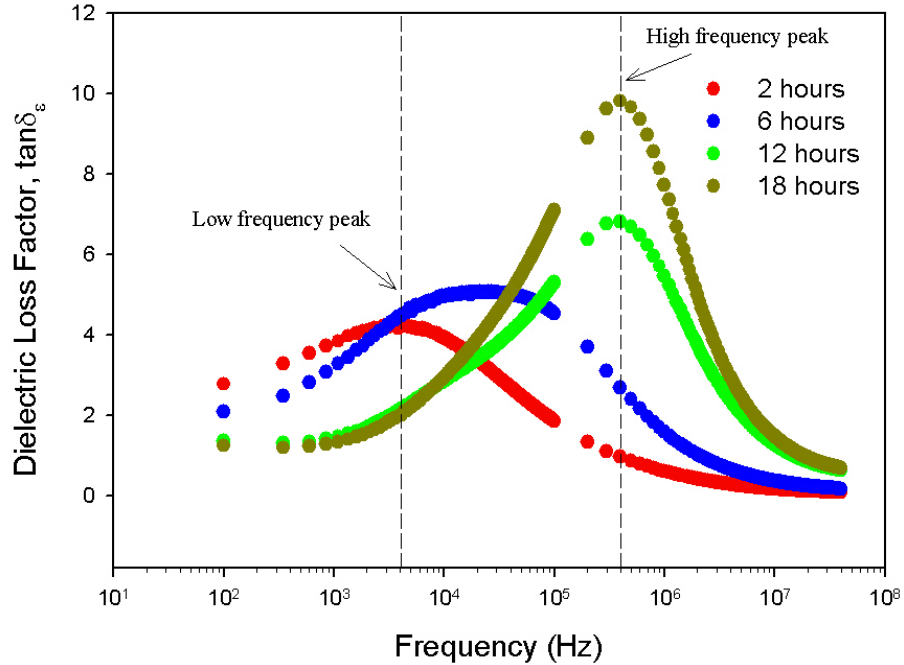


Figure 4.32 The effect of the sintering duration on the dielectric loss factor of the NZF ceramics without CaF₂ addition.

In a ferrite ceramic the dielectric loss arises due to the lag of polarization behind the applied alternating electric field; the main causes of the loss have been identified as the impurities and imperfections in the crystal lattice [38, 64]. These structural defects give rise to trapping centers, also known as correlated states, for the electrons. The response time of the electrons in the trapping centers is higher than the time taken for hopping between the sites of charged particles. The lag of polarization gives rise to the dielectric loss.

The peak observed in the dielectric loss curve at low frequencies has been attributed to the resonance of the correlated states with the applied field. The amplitude of the peak was found to depend on the extent of imperfections in the

structure [35]. The shift of the peak towards higher frequencies with increased sintering temperature or extended soak duration was attributed to the changes in the state of imperfections in the ferrite lattice. The extra Fe^{2+} ions created under these circumstances would increase the probability of jumps between the polaron sites resulting in higher dielectric losses. Thus the dielectric loss at high frequency was ascribed predominantly to the increase in electrical conductivity.

The frequency spectra of dielectric loss factor in the NZF ceramics containing 0.5, 0.75 and 1.0 wt% CaF_2 are shown in Figures 4.33 through 4.35, respectively. In the dielectric loss spectra of these ceramics, there was either no peak, or a single peak at fixed frequency would appear. In all ceramics containing some amount of CaF_2 the amplitude of the peak was depressed to much lower dielectric loss values as compared to the CaF_2 -free NZF ceramics. The presence of CaF_2 somehow inhibited the polaron formation practiced with prolonged soak during sintering. Therefore, the CaF_2 addition improved the structural features of the NZF ceramics in terms of dielectric behavior.

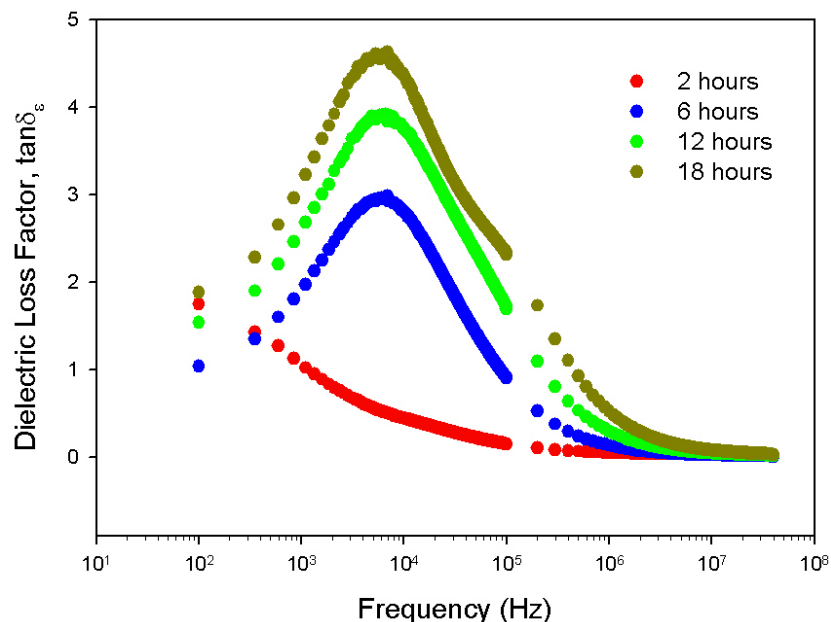


Figure 4.33 The dielectric loss factor spectra for the NZF ceramics containing 0.5 wt% CaF_2 .

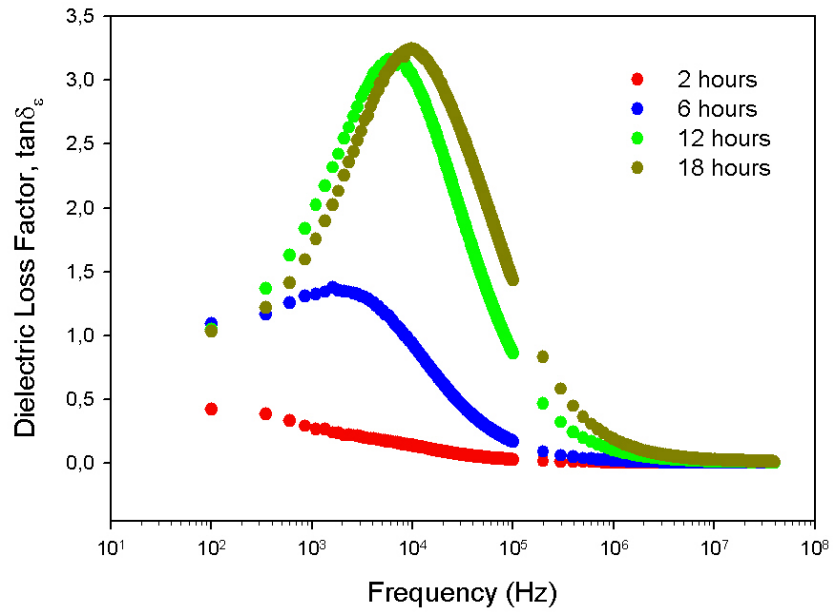


Figure 4.34 The dielectric loss factor spectra for the NZF ceramic containing 0.75 wt% CaF_2 .

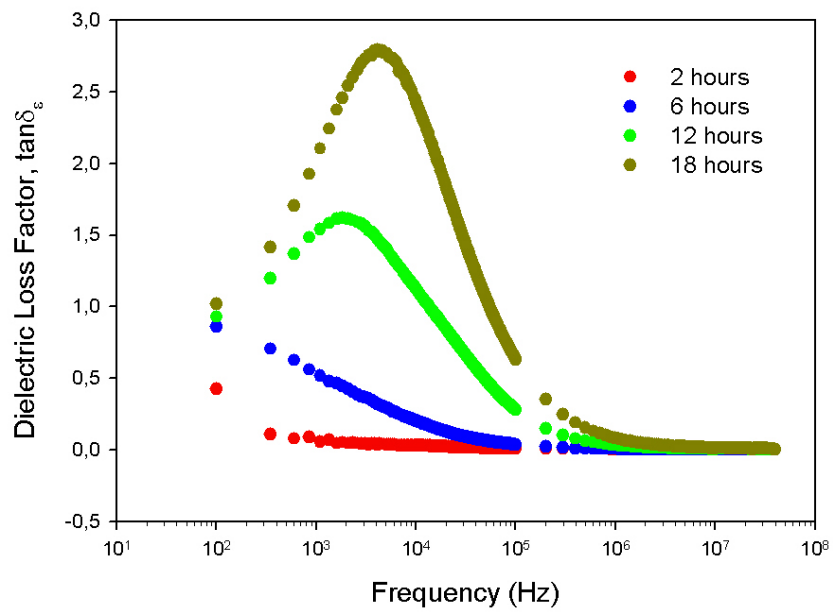


Figure 4.35 The dielectric loss spectra for the NZF ceramic containing 1.0 wt% CaF_2 .

4.9 Magnetic Properties

4.9.1 Initial Magnetic Permeability

The procedure described in Section 3.2.3.6.1 was followed in order to determine the initial magnetic permeability of ceramics. The values for initial permeability of toroidal NZF ceramics were calculated by using the following expression [3]:

$$\mu_i = \frac{L_o \cdot \pi \cdot (D_o + D_i)}{N^2 \cdot \mu_o \cdot t \cdot (D_o - D_i)}, \quad (4.15)$$

where:

- μ_i : initial magnetic permeability,
- L_o : inductance at zero applied field, H,
- D_o : outer diameter of the toroid, cm,
- D_i : inner diameter of the toroid, cm,
- N : number of turns,
- μ_o : permeability constant = $4\pi \cdot 10^{-9}$ H/cm,
- t : thickness of the toroid, cm.

The term L_o , inductance at zero applied field, was determined from the extrapolation of the inductance data obtained at low excitation voltages to the zero volt condition. The low excitation voltages attainable in the HP 4194A test rig were varied in the range 0.01 to 0.03 volt. The extrapolation procedure was carried out graphically. The values of μ_i obtained by this method at 1kHz frequency are given in Table 4.8.

Table 4.8 Initial magnetic permeability in the NZF ceramics.

Soaking Time (hours)	Initial Magnetic Permeability, μ_i , at 1kHz			
	wt% of CaF ₂ addition			
	0.0	0.5	0.75	1.0
2	314	320	311	326
6	351	341	379	352
12	421	358	378	413
18	322	403	392	416

The data given in the above table indicated that at 1 kHz frequency the initial magnetic permeability of NZF ceramics containing different amounts of CaF₂ were almost identical. The variations in soaking duration and the changes in the CaF₂ content did not produce noticeable changes in permeability.

4.9.2 Dispersion in Magnetic Permeability with Frequency

The data on the initial magnetic permeability of the NZF ceramics under variable frequency conditions are presented graphically in Figures 4.36 through 4.39. The data given in these figures indicated that the sintering conditions, expressed as soak duration, and the amount of CaF₂ content had significant effects on magnetic permeability.

For all CaF₂ additions, the initial magnetic permeability increased as the soak duration was extended. This behavior could be explained with variations in the grain size [8, 10, 65] which control the Bloch wall population in the magnetic material. When the grain size of the magnetic ferrite increases the number of Bloch walls confined in a grain also increases. The reversible bulging ability of Bloch walls under an external magnetic field determines the initial magnetic permeability response of the material. Therefore, an increase in the number of possible bulging sites resulted in enhanced initial magnetic permeability.

The resonance behavior, the hump followed by the sharp drop in initial magnetic permeability, observed at high frequency was due to the sample mounting or connection technique. When the technique was altered the resonance was replaced by relaxation which took place within a higher frequency range.

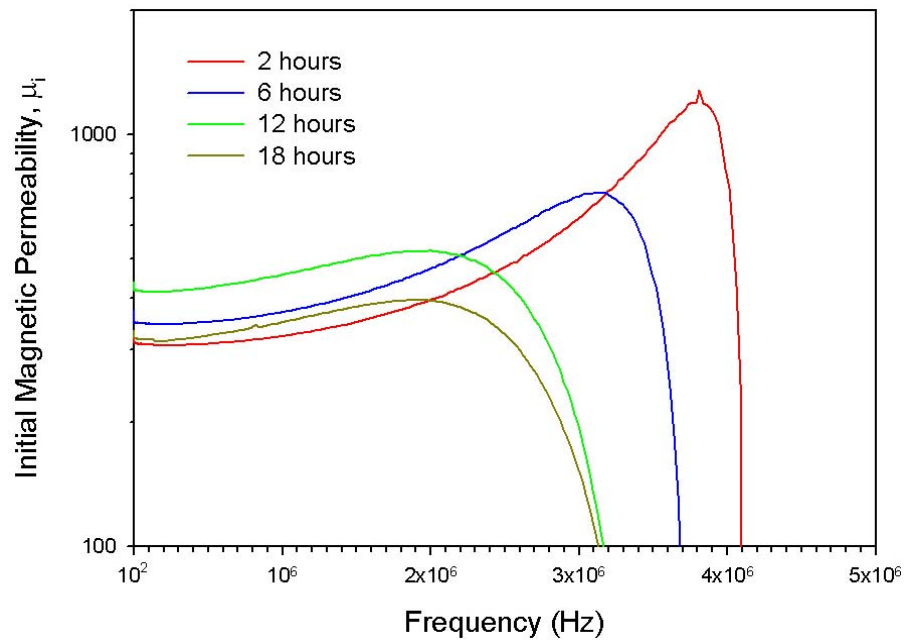


Figure 4.36 The dispersion of initial permeability with frequency in NZF ceramics without CaF_2 .

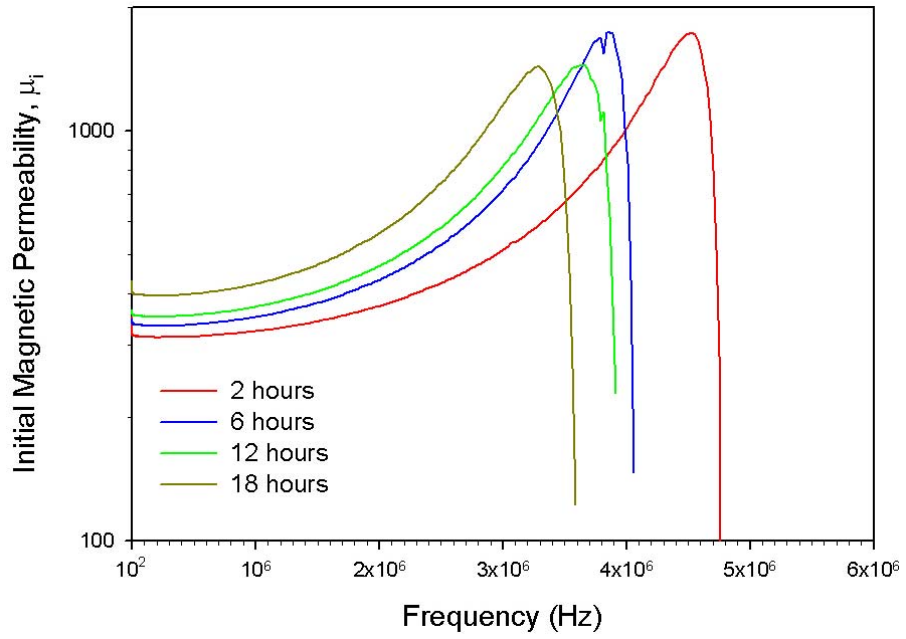


Figure 4.37 The dispersion of initial permeability with frequency in NZF ceramics containing 0.5 wt% CaF₂.

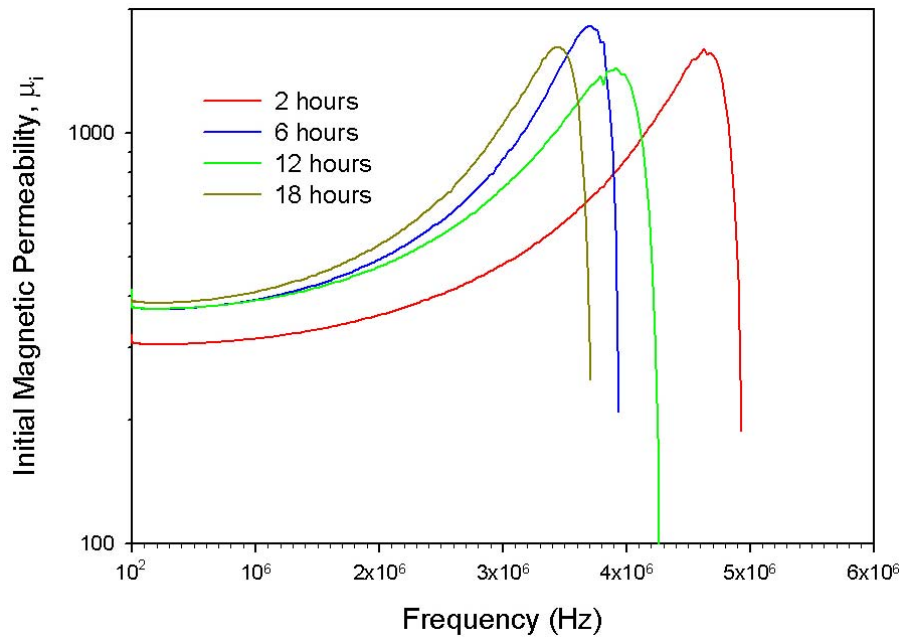


Figure 4.38 The dispersion of initial permeability with frequency in NZF ceramics containing 0.75 wt% CaF₂.

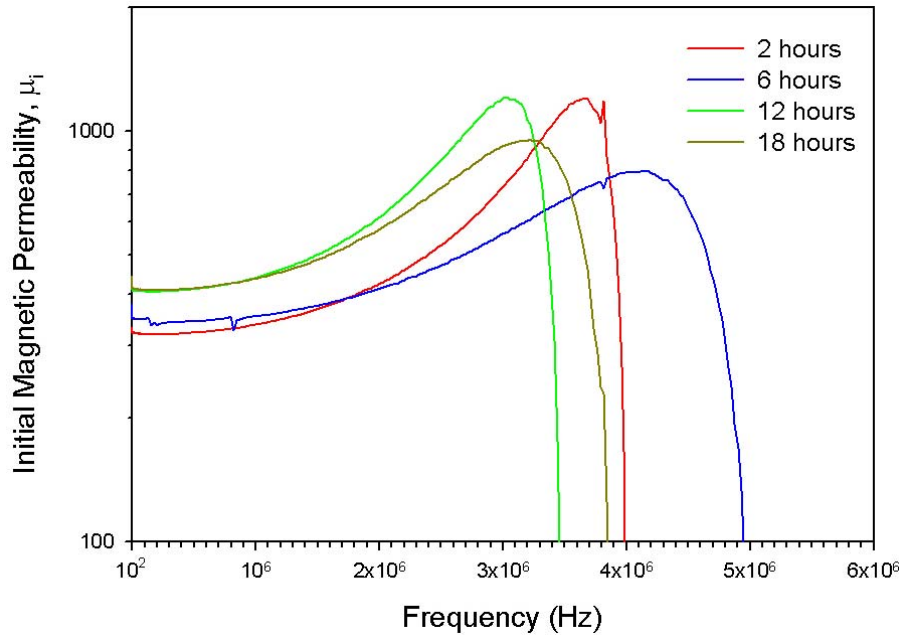


Figure 4.39 The dispersion of initial permeability with frequency in NZF ceramics containing 1.0 wt% CaF₂.

4.9.3 Relative Loss Factor

The relative loss factor (RLF) of a magnet toroid was calculated by using the following expression [6, 40]:

$$\text{RLF} = \frac{\tan\delta_{\mu}}{\mu_i}, \quad (4.16)$$

where: $\tan\delta_{\mu}$: magnetic loss factor of the toroid,
 μ_i : initial magnetic permeability of the toroid.

The RLF becomes important because of its role in comparing the magnetic quality of ferrite ceramics having different chemical compositions. In the absence of Eddy current losses the RLF turns out to be an intrinsic material property [6]. The RLF values of the ferrite ceramics were evaluated from data obtained on the magnetic loss factors as a function of applied frequency and the corresponding

initial magnetic permeability. The results on RLF determination are presented graphically in Figures 4.40 through 4.43.

The relative loss factor of all NZF ceramics prepared in this study exhibited an increase with soak duration. The effect of prolonged soaking on RLF could be correlated with the structural imperfections [39] generated in the ceramics as discussed in Section 4.8.2.2. The increase in RLF at a certain prescribed frequency, like 10^6 Hz, was diminished in the NZF ceramics containing higher proportion of CaF_2 .

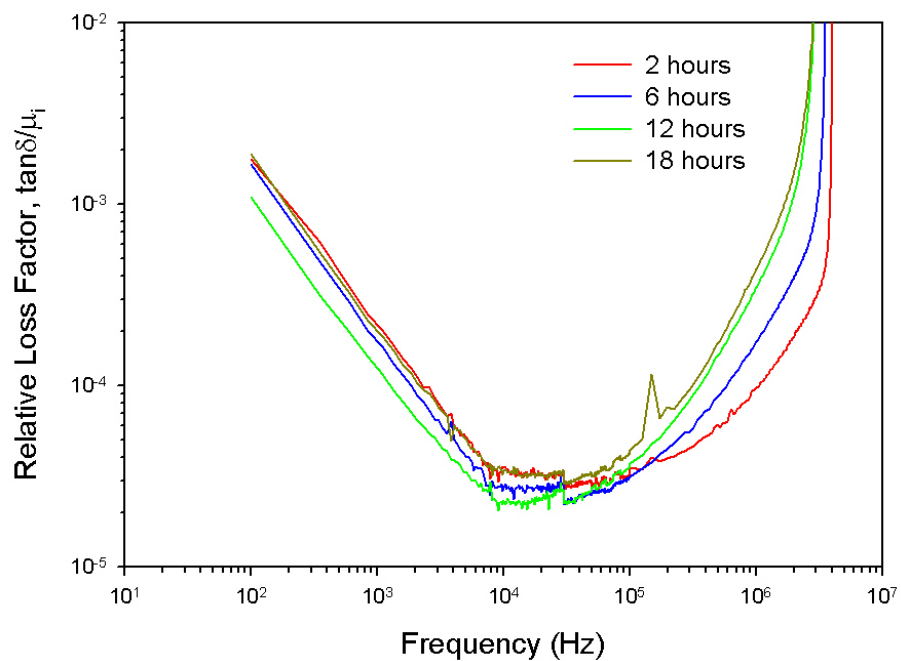


Figure 4.40 RLF spectra of NZF ceramics without CaF_2 addition.

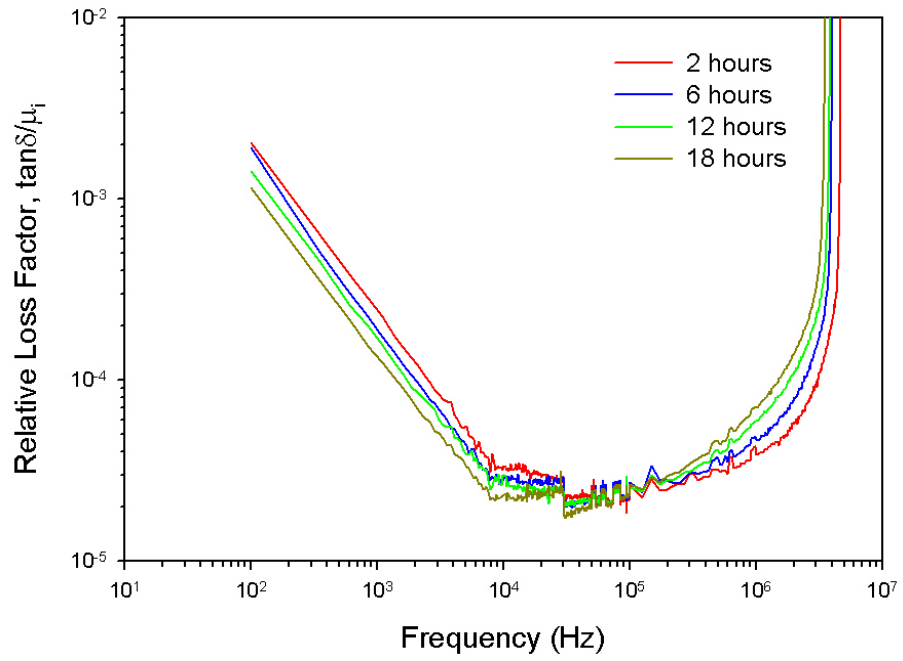


Figure 4.41 The frequency response of RLF in NZF ceramics containing 0.5 wt% CaF_2 .

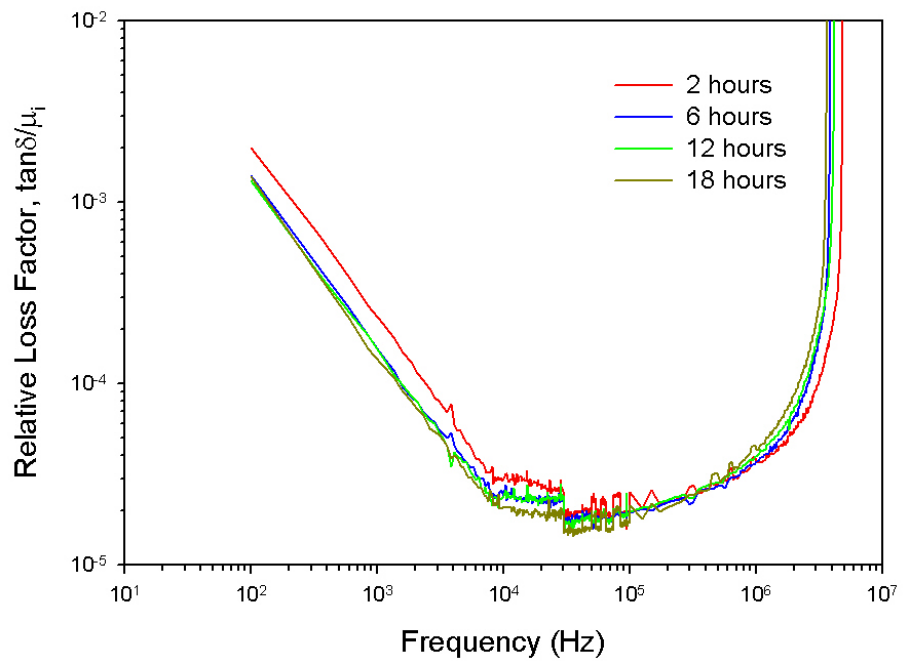


Figure 4.42 The frequency response of RLF in NZF ceramics containing 0.75 wt% CaF_2 .

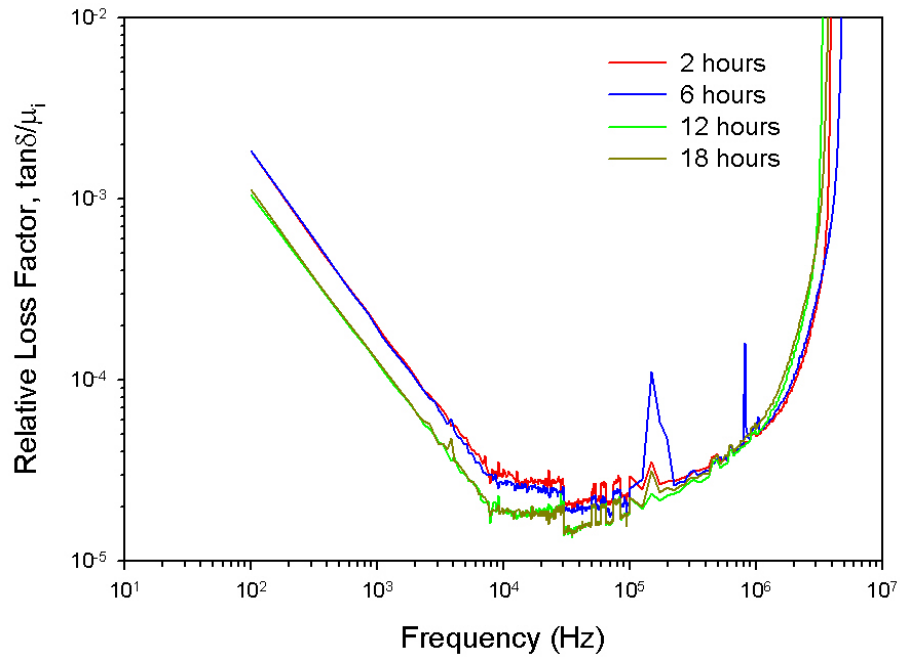


Figure 4.43 The frequency response of RLF in NZF ceramics containing 1.0 wt% CaF_2 .

4.9.4 Magnetic Hysteresis

Studies on magnetic hysteresis were conducted according to the procedure described in Section 3.2.3.6.2. The hysteresis data, reproduced graphically in the form of B (magnetization) versus H (applied field) curves, are presented in Figures 4.44 through 4.47.

4.9.4.1 Hysteresis in CaF_2 -free NZF Ceramics

The magnetic hysteresis loops of the CaF_2 -free NZF ceramics are shown in Figure 4.44. As would be observed from the curves, the saturation magnetization of ceramics was enhanced while the coercivity was decreased with extended soak duration. The increase in saturation magnetization could be attributed to the extent of densification attained in the firing process; the volume fraction of pores, which served as demagnetizing regions in the ceramic, decreased with longer soaking.

The decrease in coercivity was related to the grain growth which increased the population of Bloch walls in a grain. When the number of Bloch walls increased, the direction of magnetization prevailing in a grain could be deflected more easily in other directions. Therefore, the abrupt decrease observed in Figure 4.44 in the coercivity of the ceramics sintered for durations exceeding 6 hours was probably due to the increased proportion of large grains.

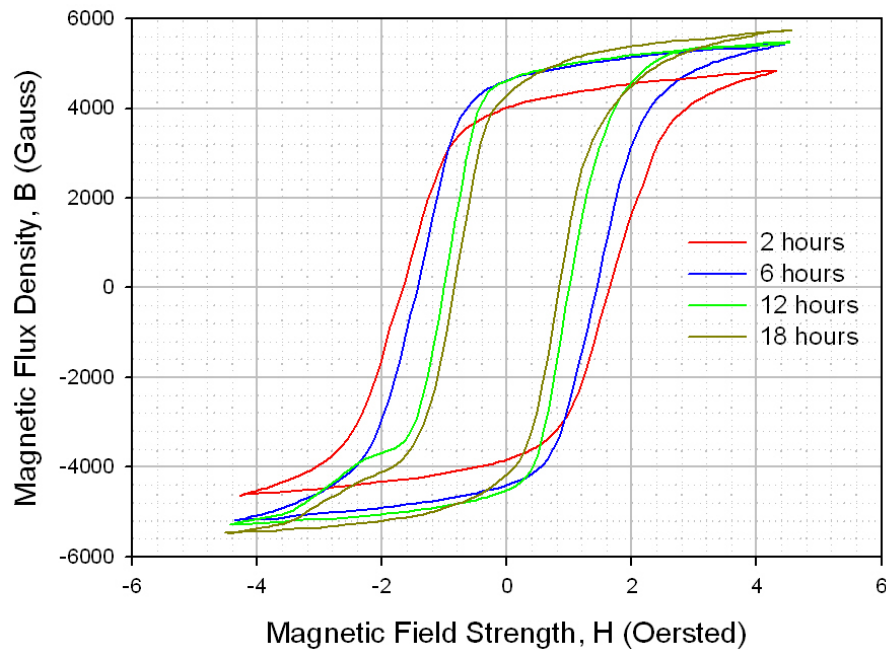


Figure 4.44 The hysteresis curves of pure NZF ceramics fired at 1200 °C with different soak durations.

4.9.4.2 Hysteresis in the NZF Ceramics Containing CaF_2

The decrease in coercivity and improvement in saturation magnetization with extended soak durations observed in CaF_2 -free NZF ceramics was also valid for ferrites containing some amount of CaF_2 . The B-H curves of the NZF ceramics containing different amounts of CaF_2 are given in Figures 4.45 through 4.47.

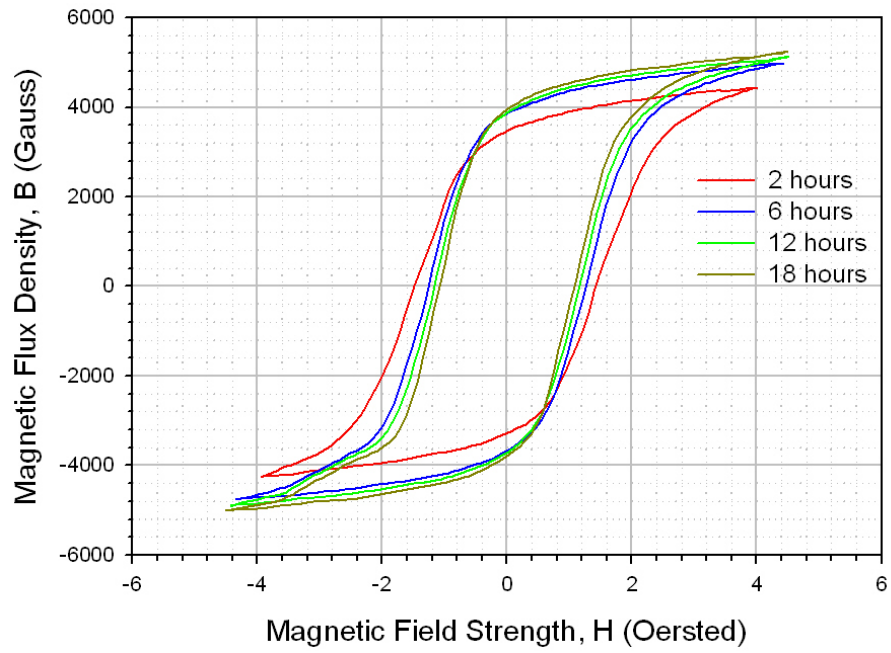


Figure 4.45 The hysteresis behavior of NZF ceramics containing 0.5 wt% CaF₂.

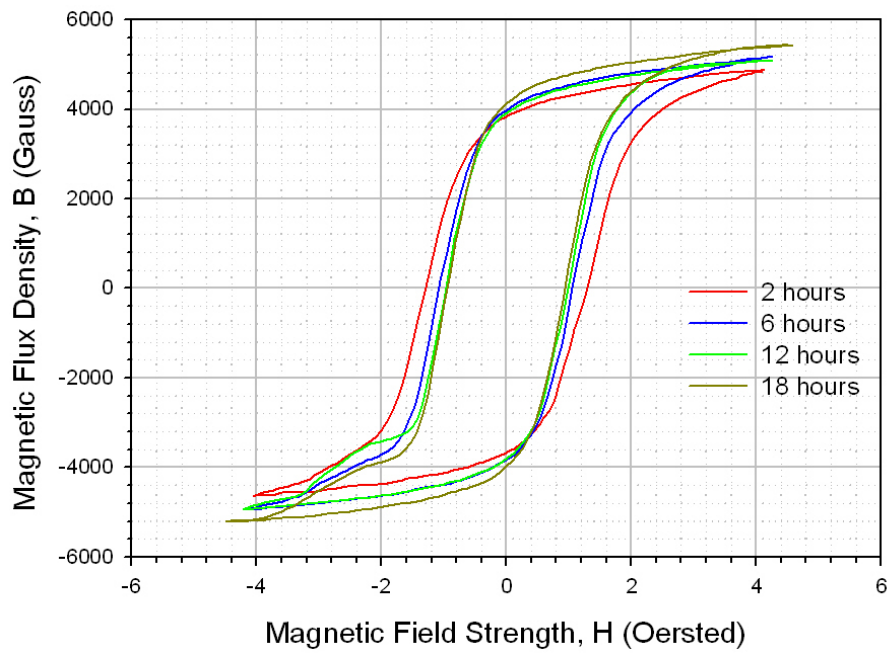


Figure 4.46 The hysteresis behavior of NZF ceramics containing 0.75 wt% CaF₂.

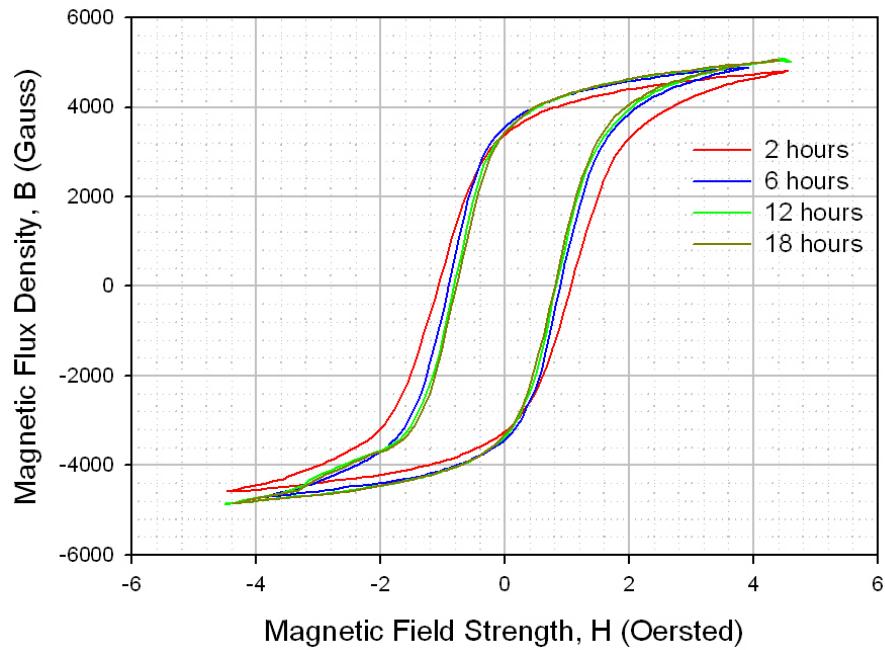


Figure 4.47 The hysteresis behavior of NZF ceramics containing 1.0 wt% CaF₂.

The values for saturation magnetization, remanent magnetization, and coercivity for all the ferrite ceramics studied in the thesis are tabulated in Table 4.9. The information given in this table revealed that additions of CaF₂ had significant effects on various magnetic parameters of the NZF ceramics. As an example, the variations in the coercivity H_C with CaF₂ content and soak duration were displayed in Figure 4.48. The curves showed that the coercivity would decline with increase in the amount of CaF₂. Prolonged sintering would exert the same effect.

Coercivity is a measure of the response of the ferrite ceramic towards successive magnetization-demagnetization cycles. The results displayed in Figure 4.48 indicated that the increasing amounts of CaF₂ made NZF more sensitive to the variation in the external magnetic field. As will be explained later, this behavior was due to the enlarged grain size attending higher CaF₂.

Table 4.9 Hysteresis parameters of the NZF ceramics studied in this thesis.

wt% CaF ₂ addition	Soakig Time (hours)	B _S (Gauss)	B _R (Gauss)	H _C (Oersted)
0.0	2	4744	3921	1.6536
	6	5315	4515	1.4338
	12	5399	4557	1.0012
	18	5618	4223	0.8379
0.5	2	4351	3375	1.4562
	6	4875	3768	1.2611
	12	5016	3795	1.1606
	18	5132	3866	1.0809
0.75	2	4772	3755	1.2954
	6	5065	3904	1.0641
	12	5026	3858	0.9760
	18	5308	4050	0.9407
1.0	2	4704	3320	1.0673
	6	4807	3489	0.8958
	12	4940	3398	0.8227
	18	4949	3368	0.7896

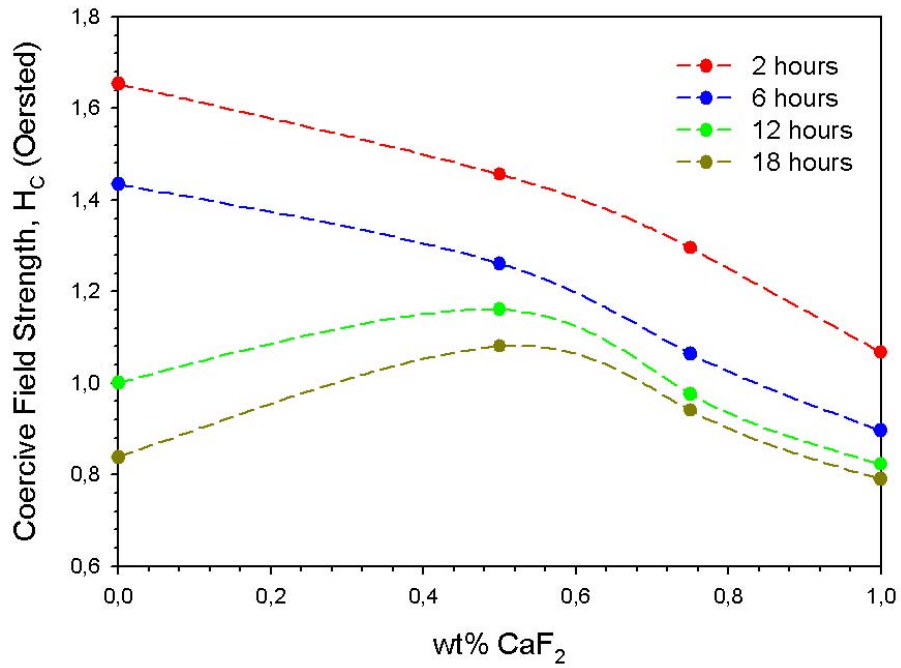
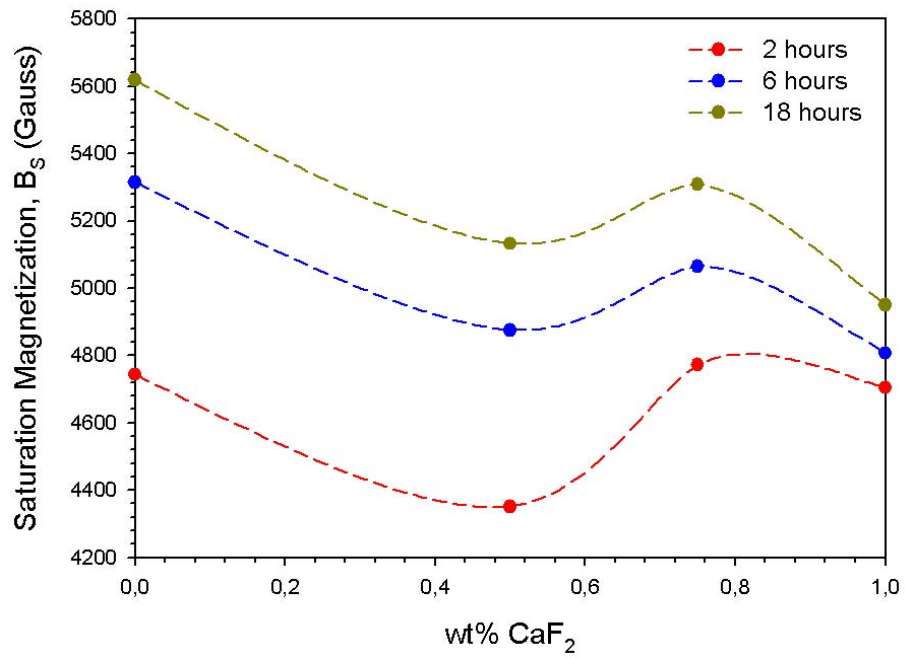
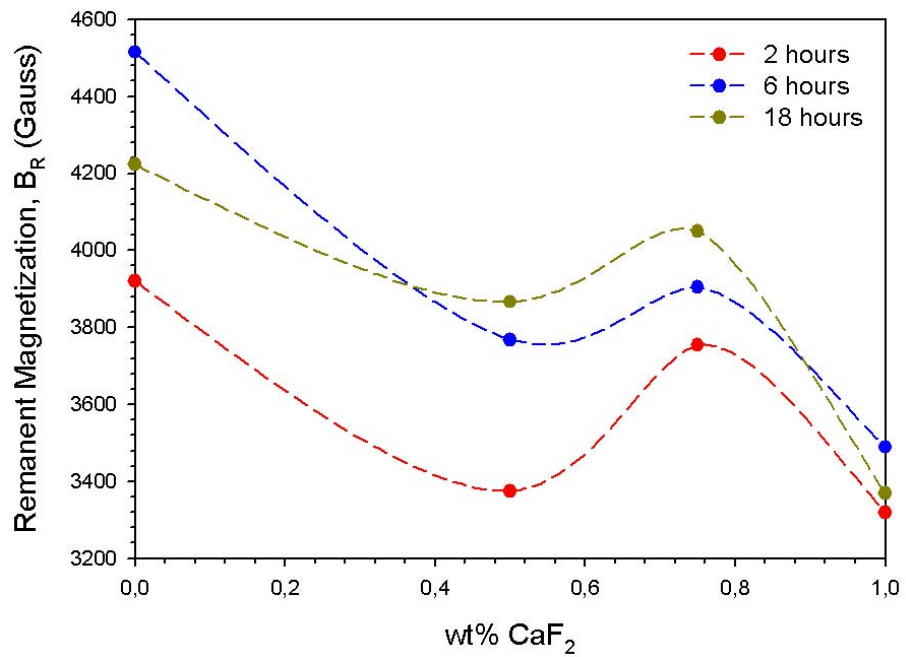


Figure 4.48 Variation in coercivity of NZF ceramics with CaF₂ content and sintering duration.

The effects of CaF₂ additions on the remanent magnetization B_R , and the saturation magnetization B_S are represented graphically in Figure 4.49. The general tendency in the B_r curve was a decline towards lower values with increased CaF₂ additions. The explanation of fluctuations observed on the B_R and B_S curves will probably require further study. At this stage, however, it should suffice to state that the values of these parameters compare quite favorably with those available in the literature [47].



(a)



(b)

Figure 4.49 Variations in remanent magnetization (a) and saturation magnetization (b) of NZF ceramics doped with CaF_2 .

CHAPTER 5

DISCUSSION AND CONCLUSION

Among the ceramic ferrite family used for communication nickel zinc ferrites (NZFs) represent the most versatile group. These materials are preferred for high frequency applications due to their high electrical resistivity, and therefore, low eddy current losses and relatively low dielectric permittivity. Electronic and magnetic properties of NZF ceramics are known to be influenced strongly with the methods used in their production. The basic chemistry of the ferrite in terms of the proportions of the constituent oxides NiO, ZnO, and Fe₂O₃ has great influence on electrical and magnetic behavior. For a ferrite of selected chemical composition, the characteristics of ceramic powders and the processing techniques involving compaction and sintering play a dominant role on the outcome.

Previous studies on dielectric properties of the NZF ceramics had already revealed that sintering at rather high temperatures had detrimental effects on the performance of these ceramics. Prolonged soak durations at high temperatures would worsen the situation. Therefore, increasing proportion of current research effort on these materials shifted towards finding means for lowering the firing temperature. One approach for attaining this goal has been benefiting from the ultra fine ferrite powders that could be sintered to a high density with minimum of porosity. Along this line, the most comprehensive study was the work reported in 1999 and then in 2005 by a research group directed by Professor D. C. Dube in Indian Institute of Technology [38, 66].

In Dube's group, Verma et al. [38, 66] used a citrate precursor route which, they claimed, yielded ferrite powders with excellent chemical uniformity at

atomic level. No information was given on powder size, but the micrographs of the fractured surfaces of the ceramics made from their powders displayed grain size not exceeding a few microns. Their NZF ceramics could be sintered at 1200 °C; in a 1 hour soak at this temperature the ceramic could be densified to within 92 to 95% of the theoretical density. The higher sintering temperature was noted to cause increased zinc losses leading to higher electrical conductivity and higher dielectric loss factors.

The second approach in attaining lower sintering temperatures would be to benefit from sintering aids. In general, the additives used for that purpose generate a liquid phase which facilitates the sintering process, but the liquid deteriorates the electronic and magnetic properties once it solidifies as a second phase. It may be due to this reason that the additive approach did not find much popularity in previous studies conducted on sintering of nickel zinc ferrite ceramics. Efforts have rather been concentrated in examining the effects of substitutions which would decrease the firing temperature but also occupy positions in the crystal structure of the ferrite. So far copper has been the only example where this approach had success [29-31].

The main objective of the present thesis project has been to examine the possibility of using CaF_2 as a sintering aid for the NZF ceramics. For this purpose, sintering studies were conducted with samples prepared from NZF powders produced by the conventional mixed oxide technique. The ceramic powder was synthesized with a fixed chemical composition represented as $\text{Ni}_{0.5}\text{Zn}_{0.5}\text{Fe}_2\text{O}_4$. The particle size attained by the MO technique was far coarser than that of the nano-scale citrate powder but yet it could be used to manufacture NZF ceramics of comparable densities.

The additions of CaF_2 in small proportions to the powder were effective in improving the densification of the ferrite. Because of time limitation sintering experiments were conducted at a single temperature of 1200 °C. Therefore, a full analysis related to the densification mechanism could not be performed. Attempts

on the treatment of the densification data in terms of existing sintering models raised more questions than answers. The sintering mechanism could be more complicated than already existing solid state sintering models, probably due to the vaporization tendency of zinc contained in the ferrite. The EDS analyses conducted on numerous ferrites sintered in the presence of CaF_2 revealed even distribution of calcium throughout all microstructures examined under SEM. Therefore, the presence of a transient liquid phase in early stages of the sintering process may be considered as a viable possibility. This aspect needs further consideration in the future.

The micrographs of the NZF ceramics containing more than 0.5 wt% CaF_2 indicated that for these ferrites the sintering temperature could perhaps be decreased to lower than 1200 °C. This would allow avoiding pore-grain boundary separation by hindering grain boundary migration. This aspect is also left to future investigations.

CaF_2 additions affected the electrical and dielectric properties of the ceramic. In general the effects were on the advantageous side. For example, in the first place, the DC electrical resistivity, summarized in Table 4.7, shifted to higher values with increasing amounts of CaF_2 in the NZF ceramic. For example, the resistivity of the CaF_2 -free NZF ceramic sintered for 2 hours was in the order of 10^6 ohm-cm. This value was raised to 10^9 ohm-cm with 0.5 wt% CaF_2 addition and then to 10^{11} ohm-cm upon increasing CaF_2 amount to 1.0 wt%. These compare quite favorably with the electrical resistivity 10^8 ohm-cm reported for a citrate-route NZF sintered at 1200 °C for 1 hour.

CaF_2 additions modified the dielectric constant and dielectric loss factor in the NZF ceramics considerably. The NZF ceramics produced by chemical powders have been praised for extremely low dielectric loss factors in high frequency applications. The dielectric loss factors of some of the NZF ceramics produced in this study with CaF_2 additions were even lower than those reported by Verma et al [38] for their citrate-route products. The loss factor curves displayed in Figure 5.1

show clearly that at all frequencies, the NZF ceramic containing both 0.75 and 1.0 wt% CaF_2 and sintered at 1200 °C for 2 hours had much lower $\tan\delta_\epsilon$ values.

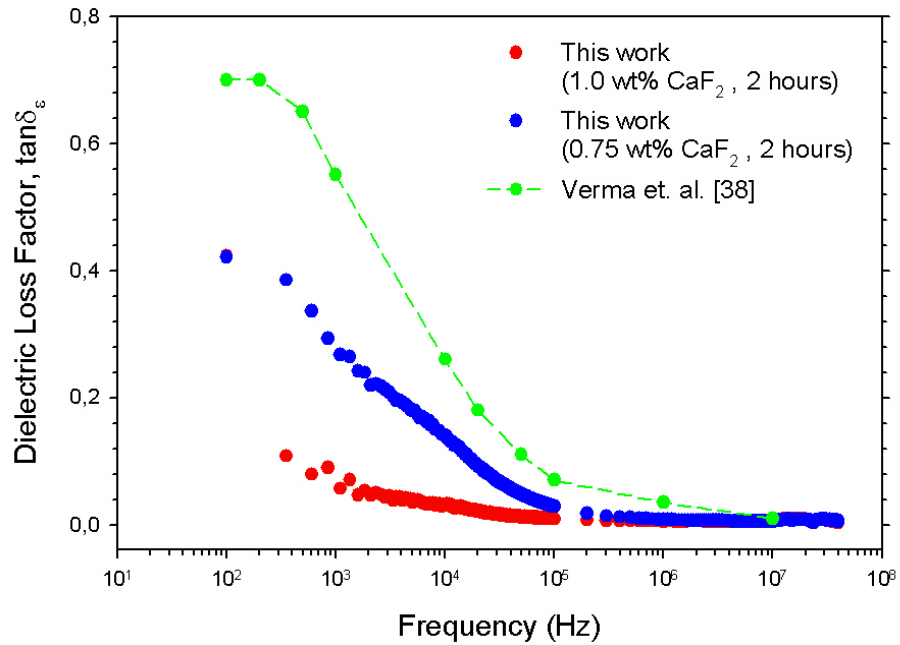


Figure 5.1 Comparison of the NZF ceramics produced via mixed oxide route in this study to the one manufactured by the citrate precursor method.

It was interesting to note that NZF ceramics doped with low amounts of CaF_2 could find application in fields outside communications. The sharp rise in the dielectric loss factor with extended soak duration may render these materials candidate for electromagnetic interference.

The study on the magnetic properties of the NZF ceramics produced in the present investigation showed that various magnetic properties could be tailored by manipulating the processing parameters. These included parameters like magnetic permeability, magnetic loss factor, and the hysteresis behavior. For example, the hysteresis loop became more slender with increasing CaF_2 addition. This would

mean an improved squareness in B-H characteristics of the NZF ceramic, making it more favorable for the communication circuit.

The CaF_2 additions resulted in a continuous decline in the coercive field strength. Prolonged sintering would produce a similar effect. The variation in coercive field strength, H_C , was related to the change in grain size. A wide range of grain size could be obtained by changing the amount of CaF_2 additions and by the soak duration. The dependence of H_C on the grain size and the amount of CaF_2 addition could be represented graphically as shown in Figure 5.2.

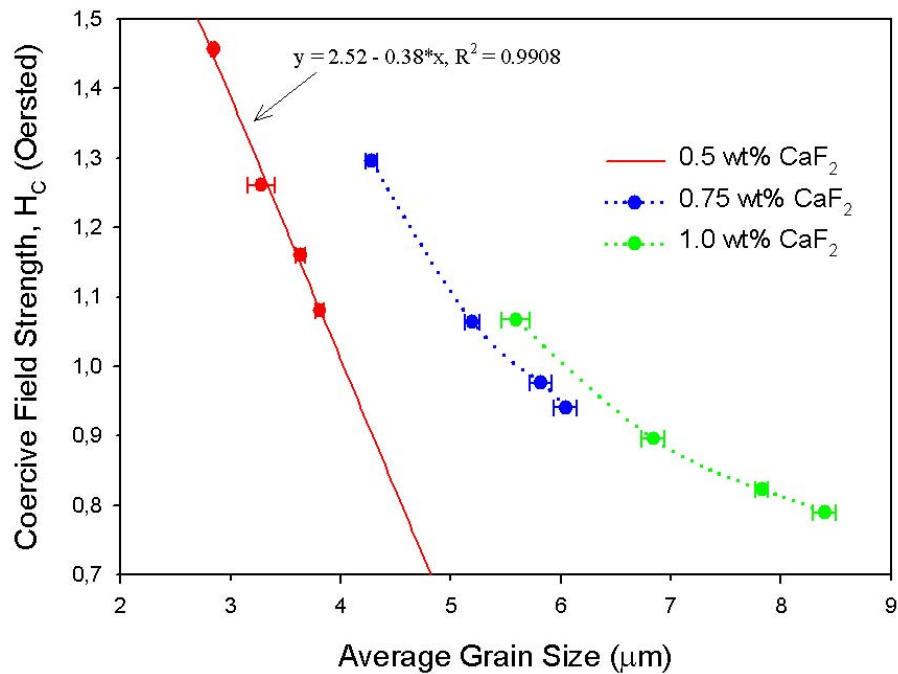


Figure 5.2 The dependency of coercive field strength on average grain size of NZF ceramics.

The initial magnetic permeability values measured in the NZF ceramics produced in this study lied in the range 300 to 1000, depending on the frequency of the external field. Regardless of the CaF_2 content, at 1 kHz frequency, the initial magnetic permeability of all NZF ceramics sintered for 2 hours was around

300. Since NZF ceramics have been classified as low μ_i materials this value should be considered quite satisfactory. Permeability values as low as 130 have been reported for citrate-route products [66].

This thesis study showed that CaF_2 had far reaching effects than a simple sintering aid. In addition to the benefits gained in the sintering behavior of the NZF it modified various electrical and magnetic properties to limits not even anticipated at the beginning of this study. Therefore, it would be quite appropriate to extend the study along the suggestions made in this chapter.

REFERENCES

- [1] Hench, L. L. and West, J. K., "Principles of Electronic Ceramics", John Wiley & Sons, 1990
- [2] Van Groenou, A. B., Bongers, P. F. and Stuijts, A. L., "Magnetism, Microstructure and Crystal Chemistry of Spinel Ferrites", Materials Science and Engineering, v3, pp 317-392, 1968/69
- [3] Heck, C., "Magnetic Materials and Their Applications", Butterworths, London, 1974
- [4] Stuijts, A. L., Rathenau, G. W. and Weber, G. H., "Ferroxdure II and III, Anisotropic Permanent Magnet Materials", Philips Technical Review, v16, pp 141-180, 1954
- [5] Moulson, A. J. and Herbert, J. M., "Electroceramics: Materials, Properties, Applications", 1st Edition, Chapman & Hall, London, 1990
- [6] Snelling, E. C., "Soft Ferrites: Properties and Applications", 1st Edition, Iliffe Books Ltd., London, 1969
- [7] Sugimoto, M., "The Past, Present and Future of Ferrites", Journal of American Ceramic Society, v82, no2, pp 269-280, 1999
- [8] Perduijn, D. J. and Peloschek, H. P., "Mn-Zn Ferrites with very High Permeabilities", Proceedings of the British Ceramic Society, v10, pp 263-273, 1968

- [9] Peloschek, H. P. and Perduijn, D. J., "High-Permeability MnZn Ferrites with Flat μ -T Curves", IEEE Transactions on Magnetics, v4, no3, pp 453-455, 1968
- [10] Röss, E., Hanke, I. and Moser, E., "Mangan-Zink-Ferrite mit Anfangspermeabilitäten bis über 20000 und ihr Gefüge", Zeitschrift für angewandte Physik, v17, no7, pp 504-508, 1964
- [11] Verma, A., Goel, T. C., Mendiratta, R. G., and Gupta, R. G., "High-resistivity nickel-zinc ferrites by the citrate precursor method", Journal of Magnetism and Magnetic Materials, v192, pp 271-276, 1999
- [12] Jonker, G. H. and Stuijts, A. L., "Controlling the properties of electroceramic materials through their microstructure", Philips Technical Review, v32, pp 79-95, 1971
- [13] Stuijts, A. L., "Microstructural Considerations in Ferromagnetic Ceramics" in Proceedings of the 3rd International Materials Symposium 'Ceramic Microstructures – Their Analysis, Significance and Production', Ceramic Microstructures, editors Fulrath, R. M. and Pask, J. A., pp 443-474, 1966
- [14] Stuijts, A. L., "Renaissance in ceramic technology", Philips Technical Review, v31, no 2, pp 44-53, 1970
- [15] Stuijts, A. L., "Low-porosity Ferrites", Proceedings of the British Ceramic Society, v2, pp 73-81, 1964
- [16] Stuijts, A. L., Verwell, J. and Peloschek, H. P., "Dense Ferrites and Their Applications", IEEE Transactions on Communications and Electronics, v83, pp 726-736, November 1964

- [17] Globus, A., “Some Physical Considerations About the Domain Wall Size Theory of Magnetization Mechanisms”, in Proceedings of the 2nd International Conference on Ferrites, pp 1-15, 1976
- [18] Stuijts, A. L. and Kooy, C., “Influence of Technological Factors on the Sintering Behavior of a Ferrite”, ‘in Proceedings of the Conference held under the auspices of the British Ceramic Society and the Netherlands Keramische Vereniging, at Noordwijk an Zee, 13-17 May, 1963’, in Science of Ceramics, edited by Stewart, G. H., v2, 1965
- [19] Louh, R., Reynolds III, T. G. and Buchanan, R. C., “Ferrite Ceramics” in ‘Ceramic Materials for Electronics’ edited by Buchanan, R. C., 3rd Edition, Marcel Dekker Inc., New York, 2004
- [20] Smit, J. and Wijn, H. P. J., “Ferrites: Physical Properties of Ferrimagnetic Oxides in Relation to Their Technical Applications”, 1st Edition, Philips’ Technical Library, Eindhoven, 1959
- [21] Jagodzinski, H., “Crystallographic Aspects of Nonstoichiometry of Spinels” in ‘Problems of Nonstoichiometry, pp 131-177’ edited by Rabenau, A., North-Holland Publishing Company, Amsterdam, 1970
- [22] Spinel, <http://www.a-m.de/englisch/lexikon/spinell-bild1.htm>, Last accessed date: January 2006
- [23] Kittel, C., “Introduction to Solid State Physics”, 7th Edition, John Wiley & Sons, New York, 1995
- [24] Newnham, R. E., “Electroceramics”, Reports on Progress in Physics, v52, pp 123-156, 1989

- [25] Mendelson, M. I., "Average Grain Size in Polycrystalline Ceramics", *Journal of the American Ceramic Society*, v52, no8, pp 443-446, 1969
- [26] Mitoff, S. P., "Electrical Conduction Mechanisms in Oxides" in 'Progress in Ceramic Science, v4, pp 217-264', edited by Burke, J. E., 1st Edition, Pergamon Press, Oxford, 1966
- [27] Reijnen, P. J. L., "Sintering Behavior and Microstructures of Aluminates and Ferrites with Spinel Structure with Regard to Deviation from Stoichiometry" in 'Science of Ceramics, v4, pp 169-188', edited by Stewart, G. H., Academic Press, 1968
- [28] Reijnen, P. J. L., "Nonstoichiometry and Sintering in Ionic Solids" in 'Problems of Nonstoichiometry, pp 219-238' edited by Rabenau, A., North-Holland Publishing Company, Amsterdam, 1970
- [29] Rezlescu, E., Sachelarie, L., Popa, P. D. and Rezlescu, N., "Effect of Substitution of Divalent Ions on the Electrical and Magnetic Properties of Ni-Zn-Me Ferrites", *IEEE Transactions on Magnetics*, v36, no 6 , pp 3962-3967, 2000
- [30] Hsu, W., Chen, S. C., Kuo, P. C., Lie, C. T. and Tsai, W. S., "Preparation of NiCuZn ferrite nanoparticles from chemical co-precipitation method and the magnetic properties after sintering", *Materials Science and Engineering B*, v111, pp 142-149, 2004
- [31] Nam, J. H., Jung, H. H., Shin, J. Y. and Oh, J. H., "The Effect of Cu Substitution on the Electrical and Magnetic Properties of NiZn Ferrites", *IEEE Transactions on Magnetics*, v31, no 6, pp 3985-3987, 1995

- [32] Sun, J., Li, J. and Sun, G., “Effects of La_2O_3 and Gd_2O_3 on some properties of Ni-Zn ferrite”, *Journal of Magnetism and Magnetic Materials*, v250, pp 20-24, 2002
- [33] Jacobo, S. E., Fano, W. G. and Razzitte, A. C., “The effect of rare earth substitution on the magnetic properties of $\text{Ni}_{0.5}\text{Zn}_{0.5}\text{M}_x\text{Fe}_{2-x}\text{O}_4$ (M : rare earth)”, *Physica B*, v320, pp 261-263, 2002
- [34] Singh, A. K., Verma, A., Thakur, O. P., Prakash, C., Goel, T. C. and Mendiratta, R. G., “Electrical and magnetic properties of Mn-Ni-Zn ferrites processed by citrate precursor method”, *Materials Letters*, v57, pp 1040-1044, 2003
- [35] Singh, A. K., Goel, T. C. and Mendiratta, R.G., “Dielectric properties of Mn substituted Ni-Zn ferrites”, *Journal of Applied Physics*, v91, no 10, pp 6626-6629, 2002
- [36] Pal, M., Brahma, P. and Chakravorty, D., “Magnetic and electrical properties of nickel-zinc ferrites doped with bismuth oxide”, *Journal of Magnetism and Magnetic Materials*, v152, pp 370-374, 1996
- [37] Mohan, G. R., Ravinder, D., Reddy, A. V. R. and Boyanov, B. S., “Dielectric properties of polycrystalline mixed nickel-zinc ferrites”, *Materials Letters*, v40, pp 39-45, 1999
- [38] Verma, A., Goel, T. C., Mendiratta, R. G. and Alam, M. I., “Dielectric properties of NiZn ferrites prepared by the citrate precursor method”, *Materials Science and Engineering B*, v60, pp 156-162, 1999
- [39] Verma, A., Goel, T. C. and Mendiratta, R. G., “Frequency variation of initial permeability of NiZn ferrites prepared by the citrate precursor

method”, Journal of Magnetism and Magnetic Materials, v210, pp 274-278, 2000

- [40] Verma, A., Goel, T. C., Mendiratta, R. G. and Kishan, P., “Magnetic properties of nickel-zinc ferrites prepared by the citrate precursor method”, Journal of Magnetism and Magnetic Materials, v208, pp 13-19, 200
- [41] Islam, M. U., Abbas, T., Niazi, S. B., Ahmad, Z., Sabeen, S. and Chaudhry, M. A., “Electrical Behavior of fine particle, co-precipitation prepared Ni-Zn ferrites”, Solid State Communications, v130, pp 353-356, 2004
- [42] Largeteau, A. and Ravez, J., “Ceramic Ferrites with Grain Boundary Barrier Layers: Role of Grain Composition on Dielectric Properties”, Materials Science and Engineering B, v6, pp 33-36.1990
- [43] Mangalaraja, R. V., Ananthakumar, S., Manohar, P. and Gnanam, F. D., “Direct current resistivity studies of $\text{Ni}_{1-x}\text{Zn}_x\text{Fe}_2\text{O}_4$ prepared through flash combustion and citrate-gel decomposition techniques”, Materials Letters, v57, pp 2662-2665, 2003
- [44] Mangalaraja, R. V., Ananthakumar, S., Manohar, P. and Gnanam, F. D., “Dielectric behavior of $\text{Ni}_{1-x}\text{Zn}_x\text{Fe}_2\text{O}_4$ prepared by flash combustion technique”, Materials Letters, v57, pp 1151-1155, 2003
- [45] Ahmed, M. A., Ateia, E., Salah, L. M. and El-Gamal, A. A., “Structural and electrical studies on La^{3+} substituted Ni-Zn ferrites”, Materials Chemistry and Physics, v92, pp 310-321, 2005
- [46] Caizer, C., “Structural and magnetic properties of nanocrystalline $\text{Zn}_{0.65}\text{Ni}_{0.35}\text{Fe}_2\text{O}_4$ powder obtained from heteropolynuclear complex combination”, Materials Science and Engineering B, v100, pp 63-68, 2003

- [47] Dionne, G. F. and West, R. G., “Magnetic and dielectric properties of the spinel ferrite system $\text{Ni}_{0.65}\text{Zn}_{0.35}\text{Fe}_{2-x}\text{Mn}_x\text{O}_4$ ”, *Journal of Applied Physics*, v61, pp 3868-3870, 1987
- [48] Ikegami, T., Kobayashi, M., Moriyoshi, Y. and Shirasaki, S., “Characterization of Sintered MgO Compacts with Fluorine”, *Journal of American Ceramic Society*, v63, pp 773-779, 1980
- [49] Ganesh, I., Bhattacharjee, S., Saha, B. P., Johnson, R. and Mahajan, Y. R., “A new sintering aid for magnesium aluminate spinel”, *Ceramics International*, v27, pp 773-779, 2001
- [50] Zhang, Y. C., Yue, Z. X., Gui, Z. L. and Li, L. T., “Effects of CaF_2 addition on the microstructure and microwave dielectric properties of ZnNb_2O_6 ceramics”, *Ceramics International*, v29, pp 555-559, 2003
- [51] Oel, H. J., “Bestimmung der Größenverteilung von Teilchen, Kristalliten und Poren”, *Berichte der Deutschen Keramischen Gesellschaft*, v43, no 10, pp 624-641, 1966
- [52] Oel, H. J., “Crystal Growth in Ceramic Powders”, in ‘Kinetics of Reactions in Ionic Systems: Proceedings of the International Symposium on Special Topics in Ceramics, Alfred University, June 18-24, 1967’, edited by Gray, T. I. and Fréchette, V. D., Plenum Press, New York, 1969
- [53] American Society for Testing and Materials (ASTM) A772 – 89 “Standard Test Method for A-C Magnetic Permeability of Materials Using Sine Current”, *Annual Book of ASTM Standards*, Volume 03.04, Philadelphia, PA, 1993

- [54] MS Thesis – Optical Micrographs of CaF₂ added NZF ceramics, <http://www.mete.metu.edu.tr/People/Assistants/Baris/All%20A%201200%20OM%20photos%20dpi72.htm>, Last accessed date: January 2006
- [55] Coble, R. L., “Sintering Crystalline Solids. I. Intermediate and Final State Diffusion Models”, *Journal of Applied Physics*, v23, no 5, pp 787-792, 1961
- [56] Zhao, J. and Harmer, M. P., “Effect of Pore Distribution on Microstructure Development: I, Matrix Pores”, *Journal of the American Ceramic Society*, v71, no 2, pp 113-120, 1988
- [57] Zhao, J. and Harmer, M. P., “Effect of Pore Distribution on Microstructure Development: III, Model Experiments”, *Journal of the American Ceramic Society*, v75, no 4, pp 830-843, 1992
- [58] Barba, A., Clausell, C., Feliu, C. and Monzo, M., “Sintering of (Cu_{0.25}Ni_{0.25}Zn_{0.50})Fe₂O₄ Ferrite”, *Journal of the American Ceramic Society*, v87, no 4, pp 571-577, 2004
- [59] Coble, R. L. and Gupta, T. K., “Intermediate Stage Sintering”, in ‘Sintering and Related Phenomena: Proceedings of the International Conference held in June 1965 at the University of Notre Dame’ edited by Kuczynski, G. C., Hooton, N. A. and Gibbon, C. F., Gordon and Breach, New York, 1967
- [60] Kingery, W. D., “Densification during Sintering in the Presence of a Liquid Phase. I. Theory”, *Journal of Applied Physics*, v30, no 3, pp 301-310, 1959

- [61] Koops, C. G., "On the Dispersion of Resistivity and Dielectric Constant of Some Semiconductors at Audiofrequencies", *Physical Review*, v83, no 1, pp 121-124, 1951
- [62] Hilborn, Jr. R. B., "Maxwell – Wagner Polarization in Sintered Compacts of Ferric Oxide", *Journal of Applied Physics*, v36, no 5, pp 1553-1557, 1965
- [63] Rosales, M. I., Amano, E., Cuautle, M. P. and Valenzuela, R., "Impedance Spectroscopy Studies of Ni-Zn Ferrites", *Materials Science and Engineering B*, v49, pp 221-226, 1997
- [64] Ngai, K. L. and White, C. T., "Frequency dependence of dielectric loss in condensed matter", *Physical Review B*, v20, no 6, pp 2475-2486, 1979
- [65] Bera, J. and Roy, P. K., "Effect of grain size on electromagnetic properties of $\text{Ni}_{0.7}\text{Zn}_{0.3}\text{Fe}_2\text{O}_4$ ferrite", *Physica B*, v363, pp 128-132, 2005
- [66] Verma, A. and Dube, D. C., "Processing of Nickel Zinc Ferrites via the Citrate Precursor Route for High-Frequency Applications", *Journal of American Ceramic Society*, v88, pp 519-523, 2005

APPENDIX A

GRAIN SIZE DISTRIBUTION GRAPHS OF NZF CERAMICS

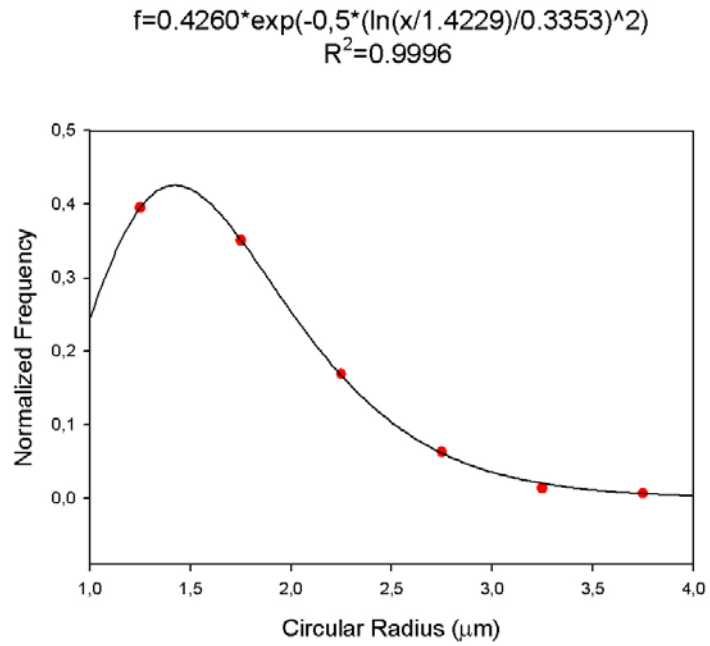


Figure A.1 The grain size distribution of NZF sample containing 0.5 wt% CaF₂. The ceramic was soaked for 2 hours at 1200 °C.

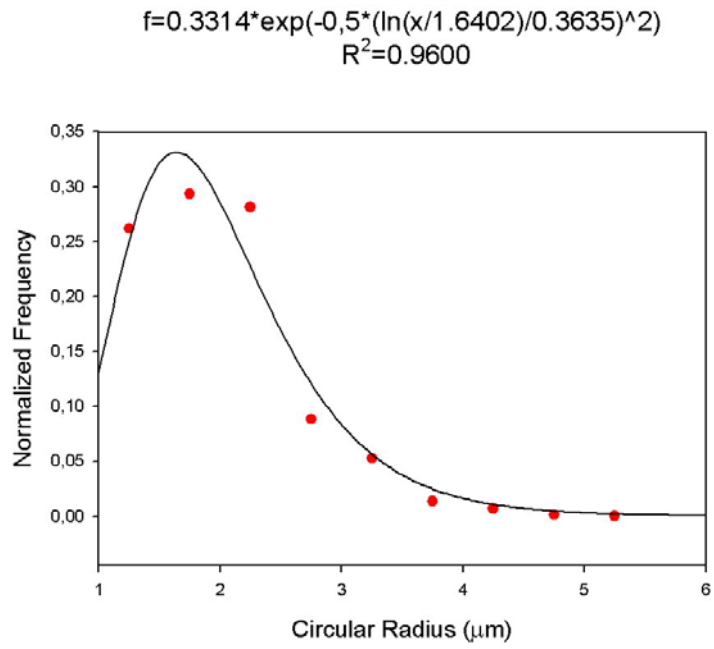


Figure A.2 The grain size distribution of NZF sample containing 0.5 wt% CaF₂. The ceramic was soaked for 6 hours at 1200 °C.

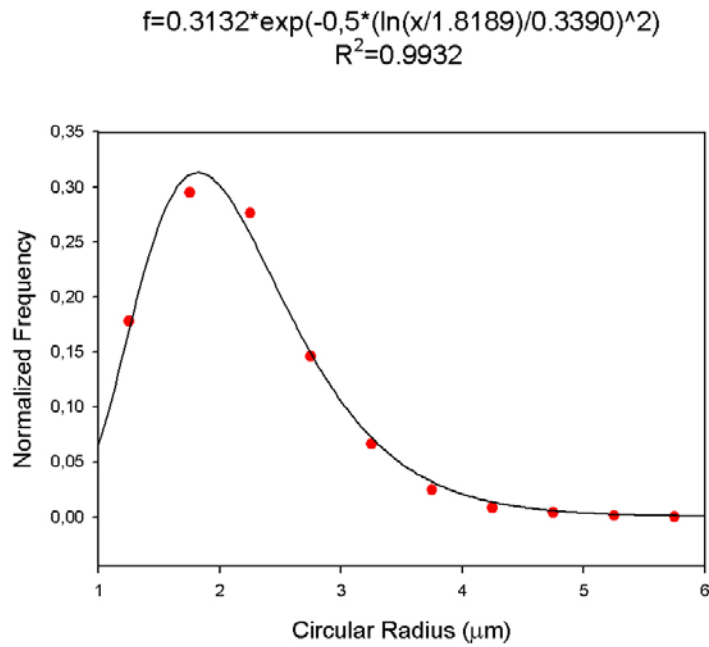


Figure A.3 The grain size distribution of NZF sample containing 0.5 wt% CaF₂. The ceramic was soaked for 12 hours at 1200 °C.

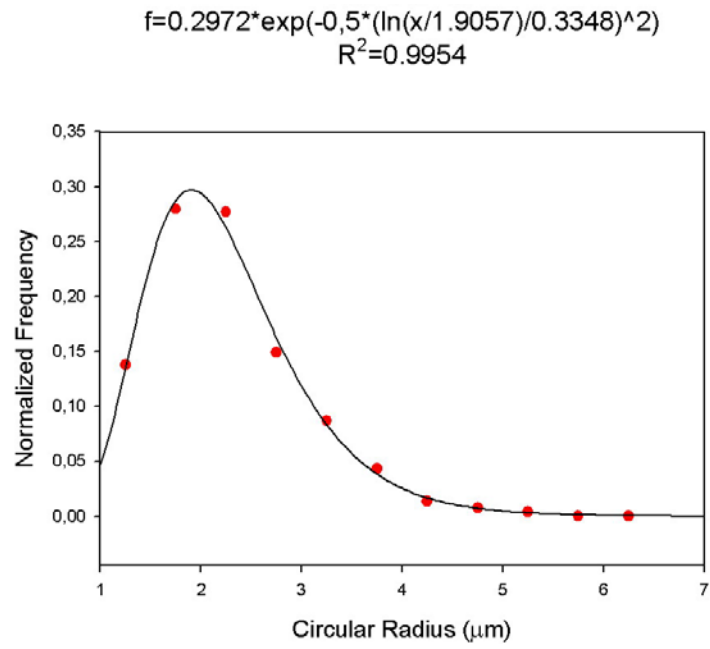


Figure A.4 The grain size distribution of NZF sample containing 0.5 wt% CaF₂. The ceramic was soaked for 18 hours at 1200 °C.

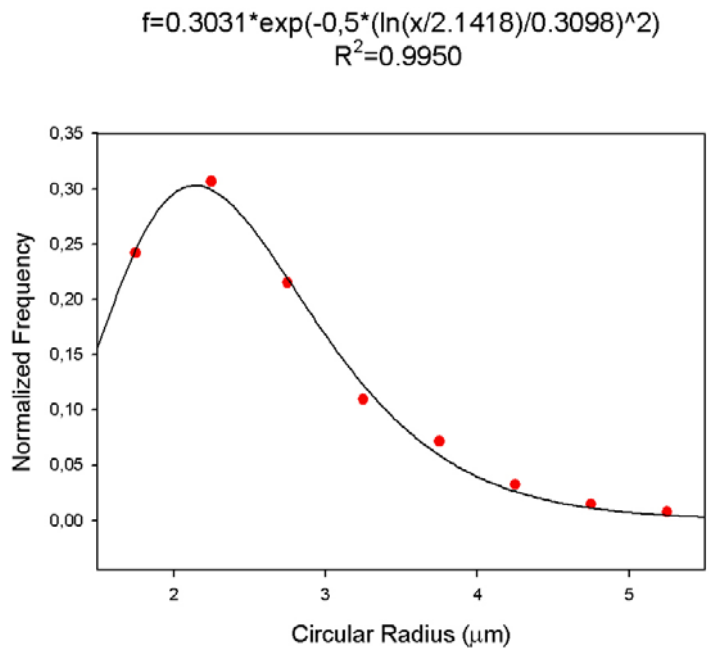


Figure A.5 The grain size distribution of NZF sample containing 0.75 wt% CaF₂. The ceramic was soaked for 2 hours at 1200 °C.

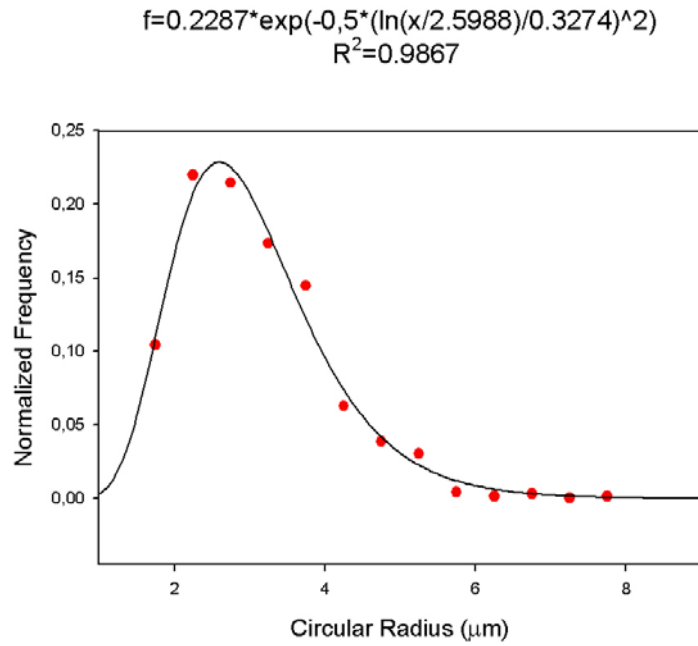


Figure A.6 The grain size distribution of NZF sample containing 0.75 wt% CaF₂. The ceramic was soaked for 6 hours at 1200 °C.

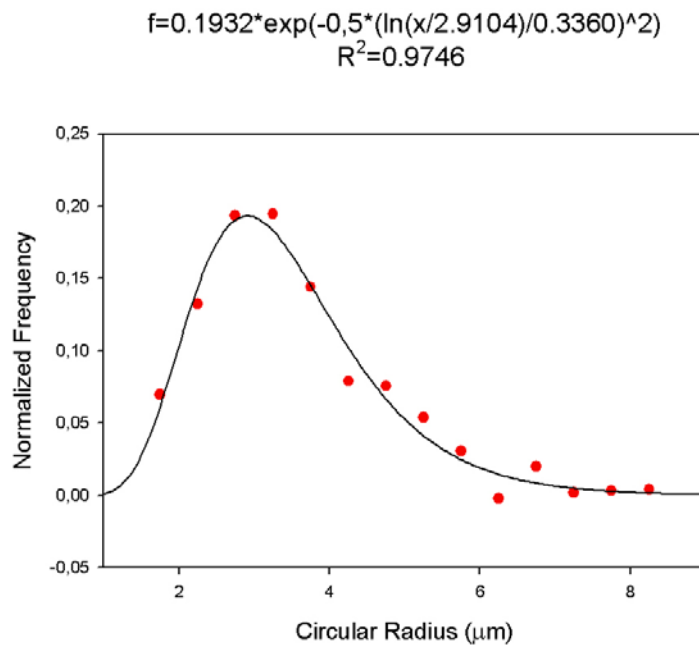


Figure A.7 The grain size distribution of NZF sample containing 0.75 wt% CaF₂. The ceramic was soaked for 12 hours at 1200 °C.

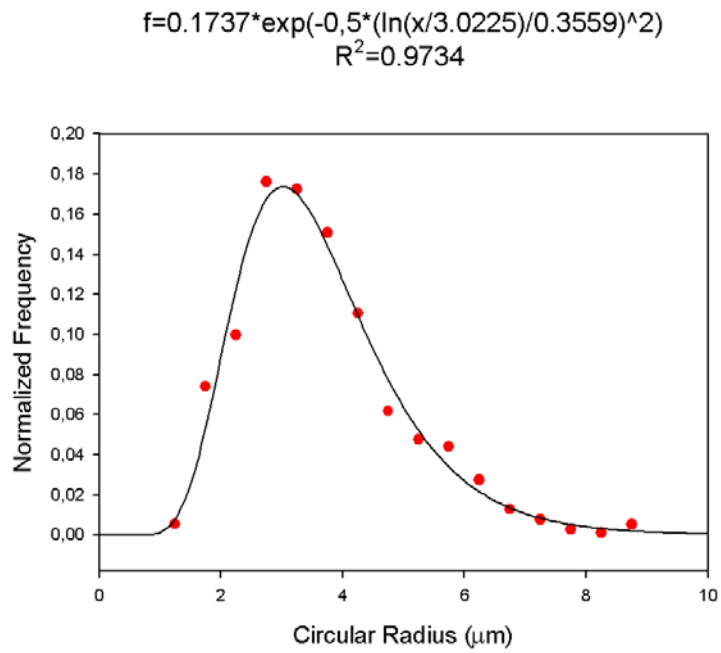


Figure A.8 The grain size distribution of NZF sample containing 0.75 wt% CaF₂. The ceramic was soaked for 18 hours at 1200 °C.

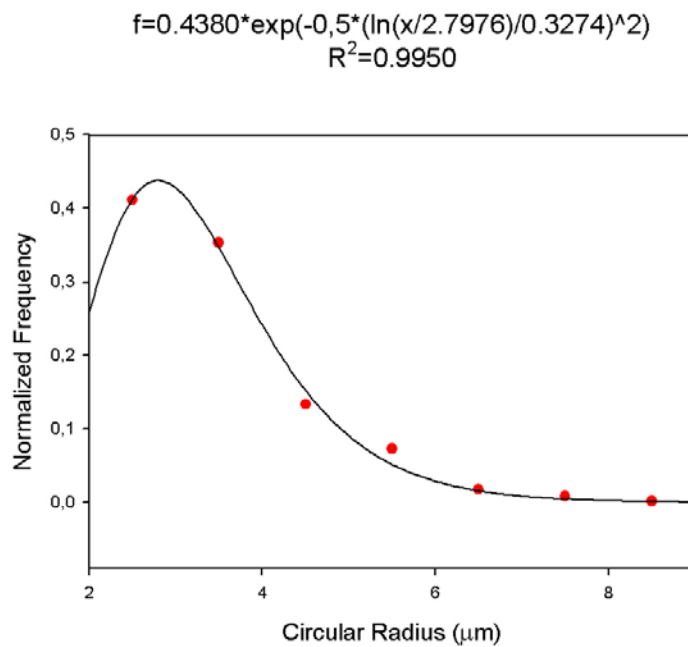


Figure A.9 The grain size distribution of NZF sample containing 1.0 wt% CaF₂. The ceramic was soaked for 2 hours at 1200 °C.

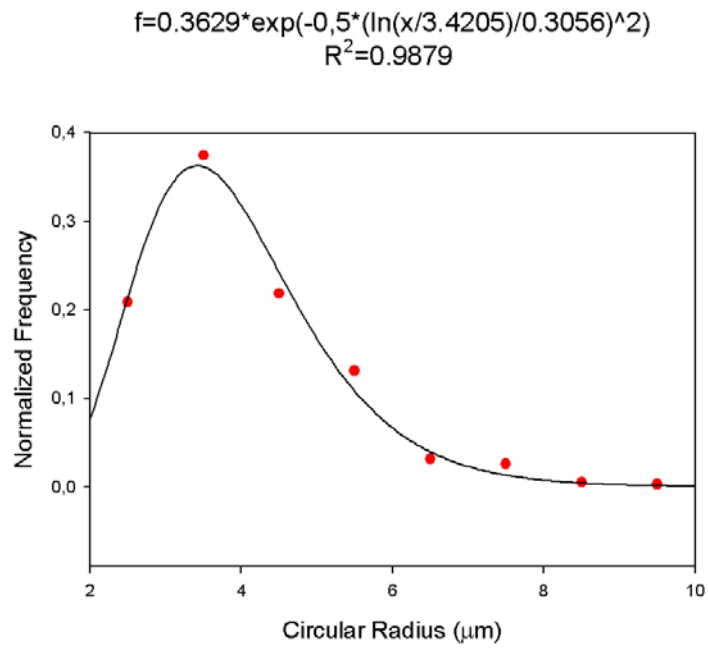


Figure A.10 The grain size distribution of NZF sample containing 1.0 wt% CaF₂. The ceramic was soaked for 6 hours at 1200 °C.

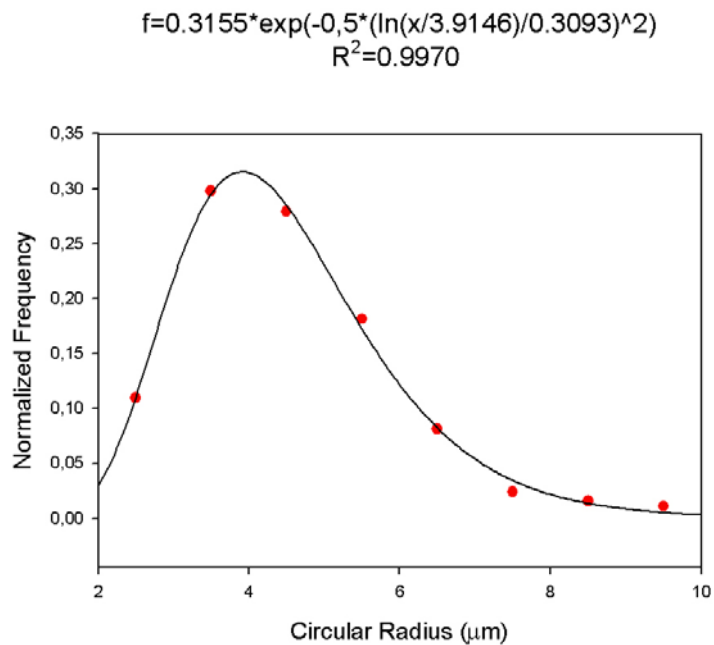


Figure A.11 The grain size distribution of NZF sample containing 1.0 wt% CaF₂. The ceramic was soaked for 12 hours at 1200 °C.

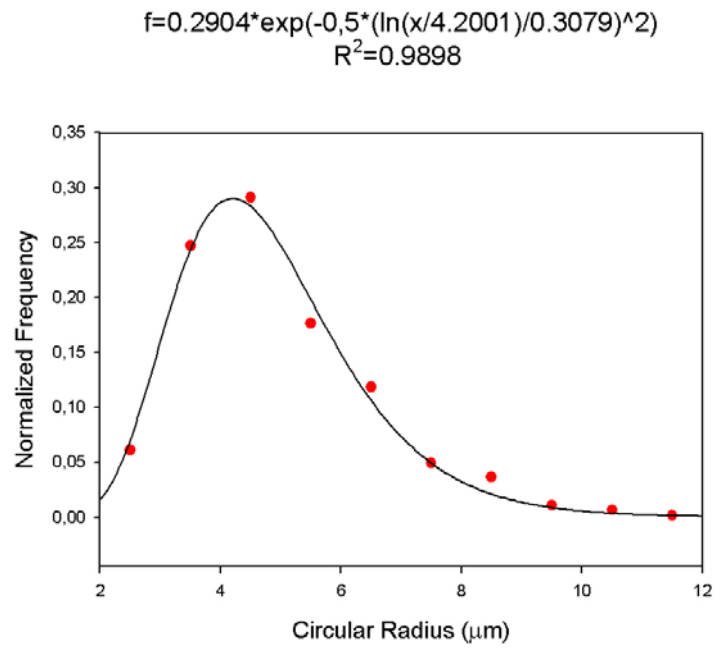


Figure A.12 The grain size distribution of NZF sample containing 1.0 wt% CaF₂. The ceramic was soaked for 18 hours at 1200 °C.